



University of Cambridge
Department of Applied Mathematics
and Theoretical Physics (DAMTP)
and
Wolfson College



Thermodynamic and hydrodynamic behaviour of interacting Fermi gases

Olga Goulko

Dissertation submitted for the degree of Doctor of Philosophy

November 10, 2011

Declaration

This dissertation is the result of my own work and includes nothing which is the outcome of work done in collaboration, except where specifically indicated in the text. No part of this dissertation has been previously submitted for a degree or any other qualification.

Olga Goulko
November 10, 2011

Summary

Fermionic matter is ubiquitous in nature, from the electrons in metals and semiconductors or the neutrons in the inner crust of neutron stars, to gases of fermionic atoms, like ^{40}K or ^6Li that can be created and studied under laboratory conditions. It is especially interesting to study these systems at very low temperatures, where we enter the world of quantum mechanical phenomena. Due to the Fermi-Dirac statistics, a dilute system of spin-polarised fermions exhibits no interactions and can be viewed as an ideal Fermi gas. However, interactions play a crucial role for fermions of several spin species.

This thesis addresses several questions concerning interacting Fermi gases, in particular the transition between the normal and the superfluid phase and dynamical properties at higher temperatures. First we will look at the unitary Fermi gas: a two-component system of fermions interacting with divergent scattering length. This system is particularly interesting as it exhibits universal behaviour. Due to the strong interactions perturbation theory is inapplicable and no exact theoretical description is available. I will describe the Determinant Diagrammatic Monte Carlo algorithm with which the unitary Fermi gas can be studied from first principles. This algorithm fails in the presence of a spin imbalance (unequal number of particles in the two components) due to a sign problem. I will show how to apply reweighting techniques to generalise the algorithm to the imbalanced case, and present results for the critical temperature and other thermodynamic observables at the critical point, namely the chemical potential, the energy per particle and the contact density. These are the first numerical results for the imbalanced unitary Fermi gas at finite temperature. I will also show how temperatures beyond the critical point can be accessed and present results for the equation of state and the temperature dependence of the contact density.

At sufficiently high temperatures a semiclassical description captures all relevant physical features of the system. The dynamics of an interacting Fermi gas can then be studied via a numerical simulation of the Boltzmann equation. I will describe such a numerical setup and apply it to study the collision of two spin-polarised fermionic clouds. When the two components are separated in an elongated harmonic trap and then released, they collide and for sufficiently strong interactions can bounce off each other several times. I will discuss the different types of the qualitative behaviour, show how they can be interpreted in terms of the equilibrium properties of the system, and explain how they relate to the coupling between different excitation modes. I will also demonstrate how transport coefficients, for instance the spin drag, can be extracted from the numerical data.

Acknowledgements

First and foremost thanks go to my Ph.D. supervisor Matthew Wingate who has introduced me to this interesting topic and has guided me through my research. Without his help, advice and encouragement this thesis would not have been possible. Matt has always found time to answer all my questions and to explain things to me that I did not understand. I could not have hoped for a more approachable and patient supervisor.

I would also like to thank my other collaborators, Frédéric Chevy and Carlos Lobo. I very much enjoyed our inspiring discussions and the great working atmosphere. I hope that in the future we will continue to work together.

Throughout my Ph.D. many people from the department have been a great help. I am especially grateful to Francis Bursa, Johannes Hofmann, Ron Horgan, Adrian Kent, Nick Manton and Stefan Meinel for many interesting discussions and helpful advice. Thanks go to all members of the Lattice Field Theory group for the friendly atmosphere and the interesting seminars and discussions. A big thank you also to Amanda Stagg for help with numerous organisational issues.

Many colleagues at other institutions have been a tremendous help and provided me with useful advice and new ideas. I am very grateful to Evgeni Burovski, Yvan Castin, Joaquín Drut, Kris van Houcke, Dean Lee, Meera Parish, Nikolay Prokof'ev, Christophe Salomon, Ariel Sommer, Boris Svistunov, Michael Urban, Herbert Wagner, Felix Werner and Martin Zwierlein. Special thanks go to Evgeni Burovski and Felix Werner for providing me with their numerical data which has been included in this thesis. Numerous other people whom I met during conferences and seminars have given me new ideas and helped me to learn new things. In particular I would like to thank all participants of the ECT* workshop “Sign problems and complex actions” for many interesting talks and discussions.

I cannot express enough thanks to my family and friends for their constant encouragement and moral support during my time in Cambridge. A huge thank you goes to my fellow Part III and Ph.D. students at DAMTP for many interesting and motivating discussions and study group meetings. Without the wonderful friendly atmosphere at Wolfson College, the inspiring lunch conversations and the occasional thesis “support group” meetings this work could not have been completed.

My research was funded by the German Academic Exchange Service (DAAD), the Engineering and Physical Sciences Research Council (EPSRC) and the Cambridge European Trust, to all of whom I am very grateful for their generous financial support. I would also like to thank the Department of Applied Mathematics and Theoretical

Physics (DAMTP), Wolfson College and the Cambridge Philosophical society for providing me with travel grants that have enabled me to attend numerous workshops and conferences. For local financial support during conferences I am grateful to the ECT* in Trento, Durham University and the ENS in Paris. Many thanks go to all the seminar organisers who have invited me to give talks at their institutions. I would like to thank the Institute for Nuclear Theory at the University of Washington for its hospitality and financial support during the programme “Fermions from Cold Atoms to Neutron Stars: Benchmarking the Many-Body Problem”.

This research was very computationally intensive and would not have been possible without the support and the helpful advice of the computing officers at DAMTP, especially Elie Bassouls, Mike Rose and John Sutton. I am also very grateful to Stefan Meinel and Hanno Rein for their help with various programming issues. This work has made use of the resources provided by the University of Cambridge High Performance Computing Service (<http://www.hpc.cam.ac.uk/>). I am grateful to Stuart Rankin from the HPC for help on various occasions.

Contents

Summary	3
Acknowledgements	4
1 Introduction	8
1.1 Ultracold atomic gases	8
1.2 Interacting Fermi gases	9
1.3 The unitary Fermi gas	16
1.4 Spin imbalance	19
1.5 Dynamical properties	21
2 The Fermi-Hubbard model at finite temperature	22
2.1 Dispersion relation	23
2.2 Tuning the coupling constant	24
2.3 Lattice corrections	26
2.4 The finite temperature formalism	29
2.5 Matrix notation	30
3 Order parameter and finite-size scaling	33
4 Diagrammatic Monte Carlo sampling	39
4.1 Formalism	39
4.2 Extending the configuration space	41
4.3 Sampling with a different distribution	42
5 Implementation of the algorithm	44
6 Observables at the critical point	50
6.1 Spin susceptibility and pseudogap	51
6.2 Critical temperature	52
6.3 Energy per particle	56
6.4 Chemical potential	60
6.5 Contact density	60
6.6 Comparison with the literature	63

7	Observables beyond the critical point	67
7.1	The equation of state for the density	69
7.2	The equation of state for the pressure	71
7.3	The temperature dependence of the contact	74
8	Simulation of the Boltzmann equation	77
8.1	Distributions in a trap	77
8.2	The Boltzmann equation	80
8.3	Numerical setup	82
8.4	Tests and optimal parameters	87
9	Collision of two fermionic clouds	95
9.1	Qualitative Behaviour	95
9.2	Transitions between regimes	97
9.3	Coupling between excitation modes	98
9.4	Transport coefficients	103
10	Conclusions and Outlook	109
A	Matrix update procedure	112
A.1	The Sherman-Morrison Formula	112
A.2	Adding one row and one column	114
A.3	Removing one row and one column	117
A.4	Changing the elements of one row	123
	Bibliography	126

Introduction

1.1 Ultracold atomic gases

The first experimental realisations of a Bose-Einstein condensate (BEC) in a dilute atomic gas in 1995 marked the birth of what has by now become an entire new area of research within condensed matter physics [1, 2]. Since then enormous progress has been made both theoretically and experimentally in the field of cold atoms. The typical densities of the systems considered range between 10^{13} and 10^{15} cm^{-3} , which is four to six orders of magnitude lower than of the air surrounding us, not to mention denser systems like liquids or solids. To observe quantum phenomena at such low densities temperatures below 10^{-5} K are required – a major technical challenge. Only with the development of advanced cooling techniques like laser cooling and evaporative cooling could such low temperatures be achieved.

But why is the study of ultracold gases so important in the first place? Partial Bose-Einstein condensation can be observed in liquid ^4He already at temperatures below 2.17 K, which is why over five decades passed between the discovery of superfluidity in liquid helium and the first realisation of a gaseous BEC. The crucial difference between the two systems is that ^4He is a liquid, which means that strong correlations are induced by interatomic interactions. These complicated interactions obscure a mean-field description for conventional superfluids and superconductors. Dilute gases on the other hand can form essentially pure condensates, well-described by the macroscopic wave function. Hence they can provide a direct realisation of many basic models in condensed matter physics.

The significance of cold atomic gases can be summarised in two main points: good tunability and a multitude of analogues. Dilute gases can be easily manipulated with lasers and magnetic fields, which gives experimentalists excellent control over a variety of properties, such as interaction strength, temperature, trapping potential and even dimension. This remarkable tunability allows to enter regimes that have not been experimentally accessible before. Also, thanks to the low density of the system, microscopic length scales are large enough to be easily observed by optical means. Superfluid features, collective oscillations, quantised vortices, few-particle systems in microtraps and Mott-insulator to superfluid transitions in optical lattices are just a small selection

of the many phenomena that have so far been subject of research in this field [3, 4].

At low temperatures the thermal de Broglie wavelength is large compared to the range of the interatomic potential and the exact form of the interaction becomes unimportant for the macroscopic properties of the system. Therefore the model of a dilute quantum gas can represent various systems in nature and can be used in different areas of physics. For example it finds application in nuclear physics where results from the field of cold gases can be used to describe systems such as low-density neutron matter or even atomic nuclei. The neutrons in the core of a neutron star are believed to form a fermionic condensate that can be studied with the methods of cold Fermi gases. Even quantum chromodynamics (QCD) at high temperatures and densities might have similar physics to these models.

In this thesis I will focus on different features of interacting Fermi gases, ranging from superfluidity to spin transport. I will begin with a general overview on interacting Fermi gases introducing the main theoretical concepts. Chapters 2-6 are devoted to a diagrammatic Monte Carlo study of the two-component unitary Fermi gas at the critical point. This work was done in collaboration with Matthew Wingate and results were published in [5], [6] and [7]. Chapter 7 extends this study to temperatures beyond the critical point, which is still work in progress. In the chapters 8 and 9 I will describe how different dynamical properties of a trapped interacting Fermi gas at high temperatures and finite values of the scattering length can be studied with a numerical simulation of the Boltzmann equation. This work was done in collaboration with Frédéric Chevy and Carlos Lobo and some of the results appeared in [8]. A summary of all results and an outlook on future work can be found in chapter 10. Throughout the text we will use units in which $\hbar = k_B = 1$.

1.2 Interacting Fermi gases

The physical consequences of quantum degeneracy are very different for Bose and Fermi gases [3, 4]. Unlike an ideal Bose gas, which exhibits a phase transition to a BEC at low temperatures, for a non-interacting Fermi gas quantum degeneracy only corresponds to a smooth crossover from classical to quantum behaviour. This is due to Pauli's exclusion principle that does not allow two identical fermions to occupy the same quantum state and thus inhibits *s*-wave scattering for non-interacting fermions. The existence of a phase transition can only be due to interactions. Depending on the depth of the interaction potential the system exhibits a rich variety of features.

In dilute systems interparticle interactions can be accurately described through two-body collisions [1, 9, 10]. Assuming elastic collisions and neglecting small relativistic spin interactions the problem of a collision between two particles of equal mass m reduces to the solution of the Schrödinger equation for the scattering of one particle

with reduced mass $m/2$ and positive energy $E = k^2/m > 0$ on the spherically symmetric finite range potential $V(r)$,

$$\left(-\frac{\nabla^2}{m} + V(r) - E\right) \psi(\mathbf{r}) = 0. \quad (1.1)$$

At large distances from the scatterer ($r \gg r_0$, where r_0 is the range of the potential) the solution of the Schrödinger equation is a superposition of the original incoming plane wave propagating in the direction of \mathbf{k} with an outgoing spherical wave,

$$\psi(\mathbf{r}) = e^{i\mathbf{k}\cdot\mathbf{r}} + f(k, \theta) \frac{e^{ikr}}{r}, \quad (1.2)$$

where the scattering amplitude $f(k, \theta)$ depends on the absolute value of the wavevector k and the angle θ between the directions of \mathbf{r} and \mathbf{k} . The scattering amplitude tells us about the probability for the scattered particle to pass through the surface element $r^2 d\Omega$ per unit time,

$$\left| f \frac{e^{ikr}}{r} \right|^2 v r^2 d\Omega = v |f|^2 d\Omega, \quad (1.3)$$

where $d\Omega$ is the solid angle element. The quantity $d\sigma = |f|^2 d\Omega$ has the dimension of an area and is called the differential cross section. An explicit expression for the scattering amplitude can be obtained by solving the Schrödinger equation (1.1) for $r \gg r_0$ and matching it to the asymptotic behaviour (1.2). The spherical symmetry of the potential implies that the solution must be axially symmetric around the direction \mathbf{k} of the incoming flux. Hence we can decompose the wave function into the ℓ -wave components of angular momentum,

$$\psi(\mathbf{r}) = \sum_{\ell=0}^{\infty} P_{\ell}(\cos \theta) \frac{\chi_{k\ell}(r)}{kr}, \quad (1.4)$$

where P_{ℓ} are the Legendre polynomials and the functions $\chi_{k\ell}(r)$ satisfy the radial Schrödinger equation,

$$\frac{d^2 \chi_{k\ell}}{dr^2} - \frac{\ell(\ell+1)}{r^2} \chi_{k\ell} + m(E - V(r)) \chi_{k\ell} = 0. \quad (1.5)$$

To match to the asymptotic form (1.2) we note that the plane wave $e^{i\mathbf{k}\cdot\mathbf{r}}$ also has a spherical wave expansion [10],

$$e^{i\mathbf{k}\cdot\mathbf{r}} = e^{ikr \cos \theta} = \frac{1}{2ikr} \sum_{\ell=0}^{\infty} (2\ell+1) P_{\ell}(\cos \theta) (e^{ikr} - e^{-i(kr-\pi\ell)}). \quad (1.6)$$

As the Legendre polynomials are pairwise orthogonal we need to match the different ℓ contributions individually. In the low-energy limit of ultracold collisions ($k \ll 1/r_0$)

the only relevant contribution comes from the s -wave component $\ell = 0$. In this case the radial Schrödinger equation outside the range of the potential $r \gg r_0$ simplifies to

$$\frac{d^2 \chi_{k0}}{dr^2} + mE \chi_{k0} = 0 \quad (1.7)$$

and has the solution

$$\chi_{k0} = A_0 \sin(kr + \delta_0), \quad (1.8)$$

with two integration constants: A_0 and the phase shift δ_0 , which generally depend on k . Comparing with (1.2) we obtain $A_0 = e^{i\delta_0}$ and

$$f_{\ell=0}(k) = \frac{e^{2i\delta_0} - 1}{2ik} = \frac{1}{k \cot \delta_0 - ik}. \quad (1.9)$$

The $\ell = 0$ contribution to the scattering amplitude turns out to be independent of the angle θ , hence s -wave scattering is equally likely in any direction. Taking the limit $k \rightarrow 0$ we can neglect the energy term altogether, and the solution of (1.7) simplifies to a linear function,

$$\chi_{k0}(r) \propto r - a, \quad (1.10)$$

where the coefficient a has the dimension of length and is referred to as the scattering length. The value (and sign) of the scattering length depends on the potential $V(r)$ and can be calculated by solving the Schrödinger equation inside the range of the potential and matching it to the asymptotic form (1.10) at $r = r_0$. The scattering length is then the intercept of this asymptote. As an example Fig. 1.1 shows the solution of the Schrödinger equation at small positive energies for the square potential

$$V(r) = \begin{cases} V_0 & \text{if } r \leq r_0 \\ 0 & \text{if } r > r_0 \end{cases}$$

for different values of V_0 . Inside the range of this potential the solution is a sine function if $V_0 < 0$ (potential well) and an exponential function if $V_0 > 0$ (potential barrier). We can see from Fig. 1.1(a) that the scattering length is positive for a repulsive potential with $V_0 > 0$ and from Fig. 1.1(b) that it is negative for a weakly attractive potential with $V_0 < 0$. As we increase the potential depth the scattering length approaches $-\infty$ and for even deeper attractive potentials becomes positive again, as shown in Fig. 1.1(c).

By comparing (1.10) to the $k \rightarrow 0$ limit of (1.8) we can obtain the leading order expression for the phase shift δ_0 ,

$$\lim_{k \rightarrow 0} \chi_{k0} \propto \lim_{k \rightarrow 0} \sin \left(k \left(r + \frac{\delta_0}{k} \right) \right) = r + \frac{\delta_0}{k} \quad (1.11)$$

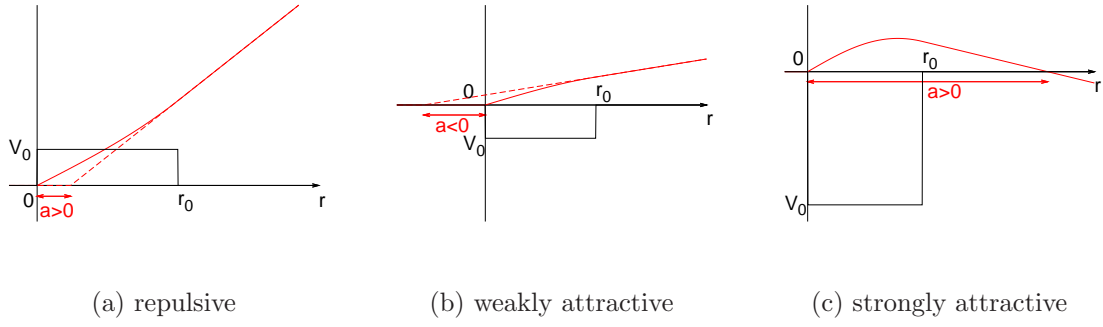


Figure 1.1: The radial wave function and its asymptote for different values of potential depth V_0 . The scattering length a is the intercept of the asymptote with the r -axis.

and therefore the scattering length equals $a = -\delta_0/k$. Hence the phase shift δ_0 is proportional to k . Higher ℓ phase shifts only contribute to order $k^{2\ell+1}$ and are thus indeed negligible at low energies [9, 10]. For the s -wave scattering amplitude (1.9) this implies

$$f_{\ell=0}(k) = -\frac{1}{a^{-1} + ik}, \quad (1.12)$$

to leading order in k . Note that when $k \rightarrow 0$ the s -wave scattering amplitude tends to a constant value, $f_{\ell=0}(k \rightarrow 0) = -a$. Hence the scattering length alone is sufficient to describe low-energy scattering. In particular, the exact shape of the interaction potential becomes unimportant. If needed, we can revert to an effective potential description and replace the potential by a more convenient form, for instance a zero-range potential, provided that it has the same long-distance behaviour. For the s -wave cross section we obtain

$$\sigma = \int d\sigma = \int |f|^2 d\Omega = \int \frac{\sin \theta d\theta d\phi}{a^{-2} + k^2} = \frac{4\pi a^2}{1 + k^2 a^2}. \quad (1.13)$$

Note that for identical fermions the orbital part of the wave function must be anti-symmetric and hence the cross section vanishes, $d\sigma = |f(\theta) - f(\pi - \theta)|^2 d\Omega = 0$. This explains why s -wave scattering is inhibited for identical fermions and a spin polarised system behaves like an ideal gas. To observe low-energy interactions at least two different fermionic components are required.

Including the next-to-leading order in the expansion of the phase shift we obtain

$$k \cot \delta_0 = -a^{-1} + \frac{1}{2} r_e k^2, \quad (1.14)$$

where r_e is called the effective range of the potential. Due to time reversal symmetry no linear term in k is present [11]. Note that the effective range is generally not the same as the range of the potential r_0 and, like the scattering length, can have arbitrary sign.

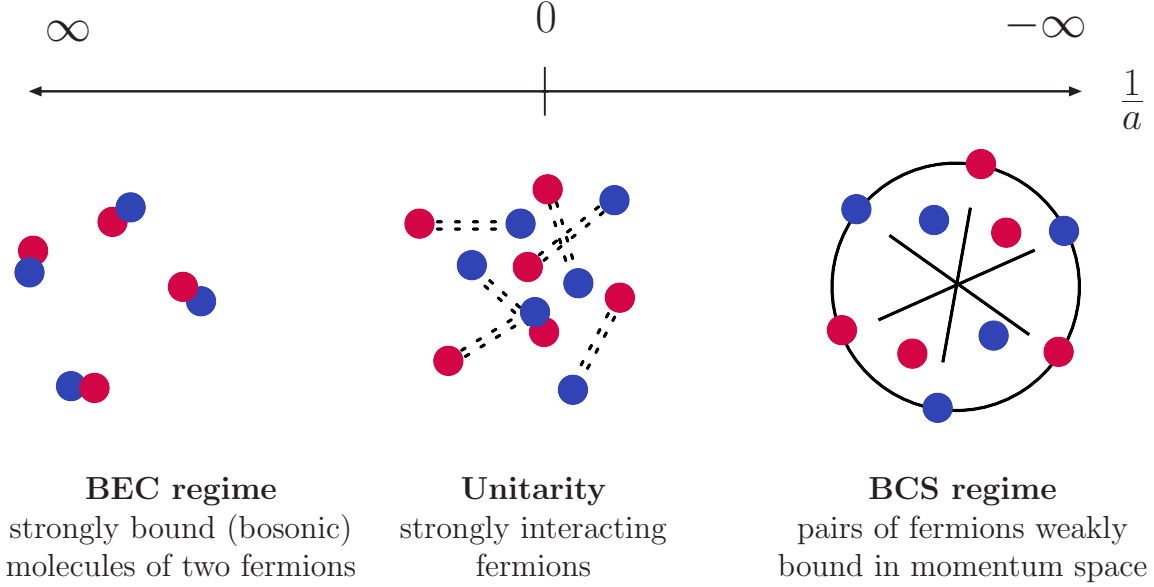


Figure 1.2: The different regimes of behaviour as a function of the inverse scattering length

So far we have only considered positive energy solutions. If the energy is negative, solutions of the Schrödinger equation are two-body bound states. The asymptotic ($r \gg r_0$) bound state wave function for $\ell = 0$ has the form

$$\chi_b(r) \propto e^{-\sqrt{m|E_b|r}}, \quad (1.15)$$

where $E_b < 0$ is the binding energy of the dimer and both particles are again assumed to have equal mass m . Expanding this expression for small energies E_b to leading order,

$$\chi_b(r) \propto 1 - \sqrt{m|E_b|r}, \quad (1.16)$$

and comparing the result to equation (1.10) yields $a^{-1} = \sqrt{m|E_b|} > 0$ and hence $E_b = -1/ma^2$. So bound states occur at positive scattering length, with binding energy inversely proportional to the square of the scattering length. This implies that a small positive scattering length can correspond both to a repulsive potential, as depicted in Fig. 1.1(a) and a bound state with large binding energy. As we shall see, the repulsive Fermi gas is unstable, and it is the gas of dimers that is usually realised experimentally.

To sum up, we have seen that in the presence of interactions the behaviour of a system depends crucially on sign and value of the scattering length a . In the following we will always consider fermions of two species, for instance two different spin states, as otherwise no s -wave interactions are possible. As sketched in Fig. 1.2, we can classify the interactions into three qualitative regions: small and negative a (the BCS regime), small and positive a (the BEC regime) and the unitary regime of divergent a that, in terms of the inverse scattering length, lies in between the BCS and the BEC regime.

The regime of small and negative scattering length, $a < 0$ and $k_F|a| \ll 1$, (where

$k_F = (3\pi^2 n)^{1/3}$ is the Fermi wavevector defined in terms of the total number density n) corresponds to a weakly attractive gas and can be accurately described using the theory J. Bardeen, L. N. Cooper and J. R. Schrieffer introduced to explain superconductivity [3]. It is thus referred to as the BCS regime. The BCS theory assumes the existence of a weakly attractive force between the fermions. Below some critical temperature, this force will cause atoms with opposite momenta on the Fermi surface to form Cooper pairs – bound states in momentum space with zero centre of mass momentum and exponentially small binding energy. This mechanism is similar to the formation of Cooper pairs of electrons in a superconducting metal. These weakly bound pairs are very large and overlap strongly in coordinate space. They form a condensate in the zero-momentum state, which gives rise to superfluidity, analogous to the superconducting state of certain metals. This regime is well-understood and the BCS theory provides exact results for many interesting quantities, both at zero and finite temperature. The critical temperature for example is

$$T_c \approx 0.28 T_F e^{\pi/2 k_F a}, \quad (1.17)$$

where $T_F = \varepsilon_F = k_F^2/2m$ stands for the Fermi temperature. With decreasing $k_F|a|$ the critical temperature becomes exponentially small, which makes the phase transition difficult to study experimentally.

As we have seen above, bound states of two atoms can be formed at positive scattering length a , with energy $E_b = -1/ma^2$ that becomes large for small values of a . Such strongly bound dimers are bosons since they consist of two fermions. They behave like a Bose gas and form a BEC below a critical temperature, so that the regime $a > 0$, $k_F|a| \ll 1$ is referred to as the BEC regime. A theoretical description of the BEC regime is provided by the usual theory for Bose gases. The critical temperature is given by

$$T_c = 0.218 T_F, \quad (1.18)$$

and is considerably higher than in the BCS case, which makes it much easier to observe in an experiment. It is important to stress that the bound states in the BEC regime are strongly bound molecules, and not weakly bound pairs as in the BCS case. These two regimes are fundamentally different and can be distinguished in an experiment, since in the BEC regime the formation of molecules is followed by their condensation only when the molecule density becomes high enough, while in the BCS regime pair formation and condensation take place simultaneously.

With respect to the relevant degrees of freedom – fermionic pairs in the BCS case and bosonic molecules in the BEC regime – these two limits correspond to weakly interacting systems and can be described analytically. The region in between, the so-called BEC-BCS crossover, is more challenging. In the limit $a \rightarrow \infty$, the s -wave

scattering amplitude obeys the universal law $f_{\ell=0}(k) = i/k$, independent of the form of the interaction. This is referred to as the unitary Fermi gas, which we will discuss in detail in section 1.3. In this case $f_{\ell=0}(k)$ takes its maximal value – the system is maximally interacting.

Experimentally, the absence of s -wave scattering in a gas of identical fermions leads to major difficulties with evaporative cooling, a technique based on scattering. This difficulty can be bypassed with help of “sympathetic cooling” techniques, which either employ two different spin components of the same Fermi gas or add a Bose gas component to the Fermi gas as a refrigerant. Another important tool for the experimental study of Fermi gases interacting with different values of the scattering length is provided by Feshbach resonances, which allow to vary the value and even the sign of the scattering length by simply tuning a magnetic field [3, 4, 12]. A Feshbach resonance occurs when the energy associated with the scattering between two particles (open channel) becomes very close to the energy of a bound state relative to a different channel (closed channel). The scattered particles can then temporarily enter the metastable bound state, which can significantly increase the scattering cross section. If open and closed channel carry different magnetic momenta, their energies can be continuously shifted with respect to each other via the Zeeman effect in the hyperfine levels, by varying an external uniform magnetic field. This can be used to tune the energies towards the resonance. By changing the energy of the closed channel from just below to just above the energy in the open channel in the presence of a small coupling, the scattering length can be tuned from large and positive to large and negative values. Crossing this threshold, the scattering length diverges. The dependence of the scattering length on the external magnetic field B can be phenomenologically modelled by the relation

$$a = a_{\text{bg}} \left(1 - \frac{\Delta B}{B - B_0} \right), \quad (1.19)$$

where a_{bg} is the background scattering length for collisions entirely in the open channel, and ΔB and B_0 describe the width and position of the resonance respectively [4, 11]. Such a resonance for the two lowest magnetic sub-states of ^6Li is plotted in Fig. 1.3. The whole range of possible values for the scattering length a , including unitarity, can be experimentally achieved using Feshbach resonances.

As we have seen, small and positive values of the scattering length can correspond to both a repulsive gas and a gas of strongly bound dimers. When the scattering length is tuned starting from a Feshbach resonance the atoms are captured in bound states, and hence only the latter case is realised [13]. It is also possible to experimentally create a repulsive gas by adiabatically switching on the scattering length starting from $a = 0$. The repulsive Fermi gas is unstable and does not exhibit superfluidity.

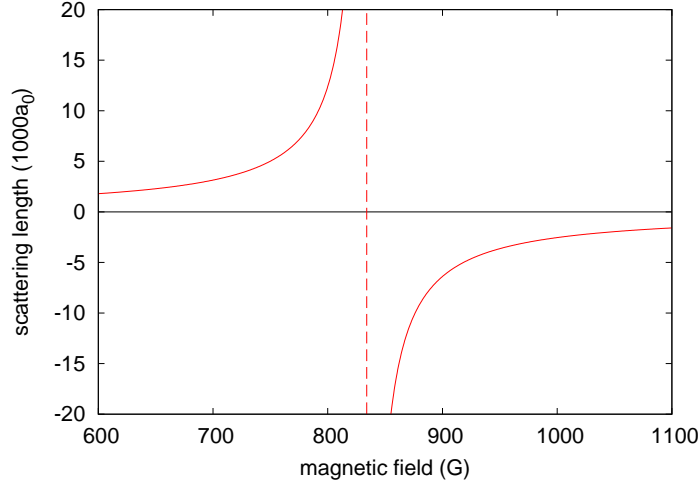


Figure 1.3: Magnetic field dependence of the scattering length (1.19) for the two lowest magnetic sub-states of ${}^6\text{Li}$. The Feshbach resonance (dashed line) occurs at $B_0 = 834$ G with a width $\Delta B = 300$ G. The background scattering length $a_{\text{bg}} = -1405a_0$ is very large, a_0 is the Bohr radius.

1.3 The unitary Fermi gas

The regime of divergent scattering length $a \rightarrow \infty$ is called unitarity and is particularly interesting for a number of reasons. In this case the gas is both dilute (the range of the interatomic potential is much smaller than the interparticle distance) and strongly interacting (the scattering length is much larger than the interparticle distance) at the same time [3]. As discussed in the previous section, details of the interatomic potential are unimportant for the description of low-energy interactions and the scattering length is the only relevant interaction-related scale of the problem. At unitarity the scattering length diverges so that this length scale is no longer present. The behaviour of the gas now only depends on two dimensionful parameters: the temperature and the density of the system. Hence all thermodynamic observables must be universal functions of the temperature T and the Fermi energy of the non-interacting gas $\varepsilon_F = (3\pi^2 n)^{2/3}/2m$. For instance the critical temperature is simply a dimensionless number times the Fermi energy, while the chemical potential in units of the Fermi energy is a purely universal function of the temperature.

On the practical side the unitary Fermi gas offers fascinating prospects to study high-temperature superfluidity. Compared to other known systems the critical temperature of the phase transition into the superfluid phase is remarkably high, as depicted in Table 1.1. If we scale it to the density of electrons in a metal this transition would occur far above room temperature [11]. Exploring the properties of the unitary Fermi gas promises valuable insights into the mechanisms behind high-temperature superfluidity and superconductivity. Another advantage of the unusually high critical temperature is that the phase transition becomes experimentally accessible, as opposed to the BCS

	T_c	T_F	T_c/T_F
metallic superconductors	1 – 10 K	50 – 150 kK	$10^{-5} - 10^{-4}$
superfluid ^3He	2.6 mK	5 K	$5 \cdot 10^{-4}$
high-temperature superconductors	35 – 140 K	2000 – 5000 K	10^{-2}
neutron stars	10^{10} K	10^{11} K	10^{-1}
strongly interacting atomic Fermi gases	200 nK	1 μK	0.2

Table 1.1: Typical critical temperatures T_c , Fermi temperatures T_F , and their ratios for various fermionic superfluids and superconductors, see [11].

regime where T_c is exponentially small.

Due to the strength of the interaction and the consequent lack of a small parameter for perturbation theory, no exact theory for the Fermi gas at large values of the scattering length has been developed yet. There exist several different analytical and numerical approaches. One possibility is to generalise the BCS mean-field theory to all values of the scattering length [14]. However at finite temperature fluctuations become crucial and the mean-field approximation is no longer valid. And even at zero temperature the many-body problem along the BCS-BEC crossover cannot be solved, since the BCS model only contains zero-momentum pairs, and thus density fluctuations are not accounted for [4].

One example of an analytical approach is to postulate N fermionic flavours and to consider a system with $2N$ (rather than only two) fermionic fields, interacting with a bosonic field [15]. The fermionic degrees of freedom can be integrated out, leaving only the complex scalar field with a corresponding effective action. From this an expansion in $1/N$ can be generated for different observables. The problem is solved in the $N \rightarrow \infty$ limit with correction terms of leading order in $1/N$. The $1/N$ corrections are comparatively large, given that the physically interesting case is $N = 1$.

A self-consistent many-body approach based on the Luttinger – Ward formalism is presented in [16]. In this approach the grand thermodynamic potential is expressed in terms of Green’s functions and interactions between fermions are represented as a perturbative series of irreducible Feynman diagrams. As the complete series is impossible to calculate one needs to employ the ladder approximation which describes the formation of pairs and is exact in the BCS limit. The De Dominicis – Martin extension allows to also incorporate bosonic degrees of freedom and improves the results across the BEC-BCS crossover. An advantage of this approach is that the Green’s function need not be approximated in terms of free Green’s functions. Also the results are valid for all values of the scattering length. However it fails to correctly capture the critical behaviour at the superfluid transition, as it predicts a weak first order transition rather than a second order one.

Other analytical methods include an effective theory based on an expansion around $d = 4 - \epsilon$ and $d = 2 - \epsilon$ spatial dimensions [17, 18]. Both limits can be treated ana-

lytically: near $d = 4$ the unitary Fermi gas behaves like a weakly interacting system of fermionic and bosonic degrees of freedom and near $d = 2$ like a weakly interacting Fermi gas, see [19] for a review. The physical case $d = 3$ is obtained through extrapolation of the series expansion to $\epsilon = 1$. To first order, this approach allows to derive an effective potential, from which thermodynamical quantities can be calculated with good accuracy. However, the next order reveals a deviation from the numerically and experimentally predicted values, which indicates that the expansion might not converge sufficiently quickly. A calculation to third or higher order involves a significant increase in difficulty.

Due to the strong nonperturbative nature of the problem numerical approaches are the only ones that can give reliable quantitative predictions about the properties of the Fermi gas in the unitarity limit. Unlike the analytical approximations they can start directly from first principles and model the system in a systematically improvable way. They provide quantitative results that can be compared directly with experimental data and can be used as a benchmark to test analytical methods. An example is the beyond mean-field approximation from [20], where the equation of state of the unitary Fermi gas is compared to Monte Carlo results using three different perturbation (T -matrix) schemes. Since there is no a priori judgement as to which perturbation scheme is more accurate, the comparison to numerical results is vital. Monte Carlo results are also used for a phenomenological interpolation of the analytical prediction around the critical point, where the purely analytical results are poor.

By today, numerical methods have advanced so far that they can produce high precision results for several quantities, for instance the critical temperature, with up to a few percent accuracy. Many numerical approaches use methods from nuclear theory, for instance the effective field theory approach in [21] which uses hybrid Monte Carlo to simulate cold dilute neutron matter on the lattice. At zero temperature fixed-node diffusion Monte Carlo finds wide application. In this setup the wave function is sampled via a trial function using the Schrödinger equation. The fixed node approximation enforces the positive definiteness of the sampling function, to avoid the fermionic sign problem. At finite temperature it is used for the nonperturbative restricted path integral Monte Carlo [22]. Due to the fixed-node approximation at finite temperature this approach can only give upper bounds on the critical temperature. The auxiliary field quantum Monte Carlo method [23, 24, 25] uses a continuum model with a momentum cut-off and is independent of the dispersion relation.

In this work we will focus on the determinant diagrammatic Monte Carlo (DDMC) approach [26], which will be described in detail in the following chapters. This approach avoids the fermionic sign problem for the two-component balanced gas and can provide precise predictions for the critical temperature and other thermodynamic observables at unitarity.

1.4 Spin imbalance

So far, most numerical studies were limited to the balanced case, when the number of fermions in the two spin components is equal. An imbalance in the particle number results in new interesting effects, which makes a detailed numerical study desirable [3, 27, 28]. Amongst the main areas of interest are the finite temperature phase diagram, new exotic phases and phase transitions, as well as the analysis of the strongly interacting normal state at high imbalance. Imbalanced Fermi gases are also related to superconductors under an external magnetic field. Since the orbital motion of the electrons screens this field in bulk superconductors, a highly imbalanced state is difficult to achieve. Superfluid Fermi gases do not suffer from this restriction. Also, unlike with superconductors, we are not limited to the BCS regime but can work across the whole BEC-BCS crossover.

As the single component Fermi gas does not interact via *s*-wave scattering and consequently cannot undergo a phase transition into the superfluid phase it is clear that as we increase the imbalance at some point superfluidity must break down even at zero temperature. Experiments agree however that the superfluid phase is remarkably stable towards imbalance and that this breakdown occurs at a very high critical imbalance of around 77% at unitarity [29, 30]. The authors of [31] quote an even higher value of over 90%, but this discrepancy is probably due to their system being out of equilibrium, as a consequence of the highly elongated trap geometry and the evaporative cooling scheme which create a polarisation pattern that favours a superfluid at the trap centre [32]. In all experiments a phase separation was observed as imbalance increased. A fully paired superfluid core formed in the trap centre, surrounded by a shell of imbalanced gas in the normal phase.

Many properties of the zero temperature phase diagram can be deduced analytically. On the BCS side, the two Fermi surfaces become mismatched at finite imbalance and Cooper pairs with zero total momentum are difficult to form. When the gap between the two Fermi surfaces becomes too large, superfluidity is broken and a first order transition into a normal phase occurs. As the superfluid must be fully paired, the excess atoms of the majority species will be spatially separated from the superfluid. The result is a combination of a paired superfluid phase and a normal phase which is a uniform non-interacting mixture of the two species, in agreement with experimental findings. On the BEC side, the energetically favourable phase is a uniform mixture of a superfluid gas of bosonic dimers and of a normal gas of spin polarised fermions. What happens in the unitarity limit is not yet completely clear.

Apart from the conventional normal and superfluid phases a spin imbalance opens the possibility for the formation of new exotic states. The most prominent one is the FFLO phase (after Fulde, Ferrell, Larkin and Ovchinnikov). In the classical BCS picture Cooper pairs with zero centre of mass momentum are formed by two particles at the

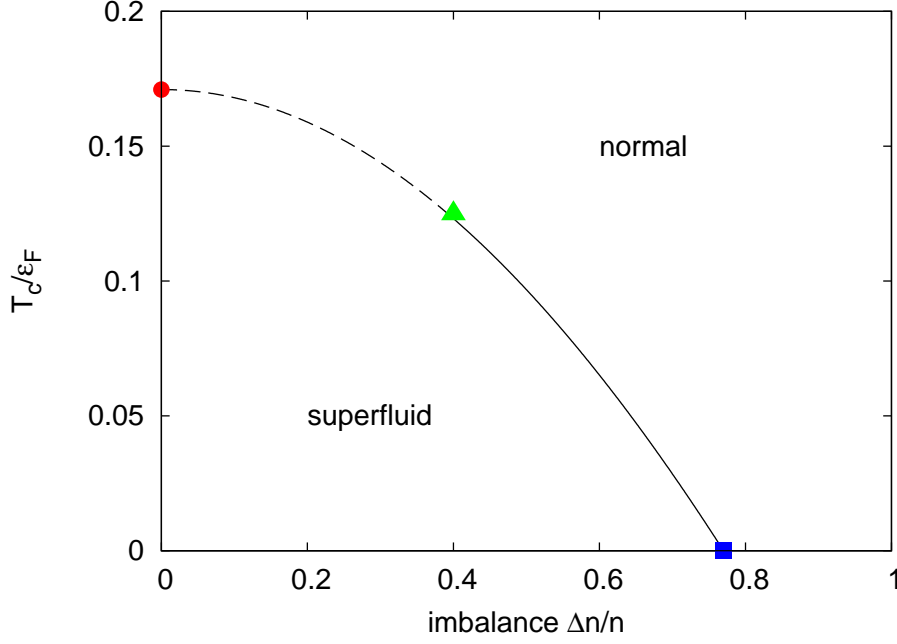


Figure 1.4: Sketch of the finite temperature phase diagram of the spin imbalanced unitary Fermi gas, as in [28]. The phase transition is first order at zero temperature (blue square) and second order at zero imbalance (red circle), which implies the existence of a tricritical point (green triangle). Above this point, the critical line is second order (dashed line), and first order below (solid line).

Fermi surface. In an imbalanced system the two Fermi surfaces become mismatched. The FFLO phase is characterised by the formation of pairs of two particles at their respective Fermi surfaces, which consequently have non-zero centre of mass momentum. This momentum can be interpreted as a spatial variation of the order parameter. It can be shown that the FFLO phase occurs only in a very small domain of imbalance in the BCS limit and is difficult to observe at unitarity. A zero-momentum pair can also be formed if a particle on the surface of the minority Fermi sphere pairs with a particle of opposite momentum inside the majority Fermi sphere. This phase, which is unstable, is referred to as the Sarma phase. Exotic states due to deformed Fermi surfaces have also been suggested.

At finite temperature thermal fluctuations reduce the gap and therefore we expect the critical imbalance to decrease with growing temperature, resulting in a critical line which ends in the critical point for the balanced Fermi gas. We know that at zero temperature the phase transition is first order, whereas for the balanced gas it is second order. This implies the existence of a tricritical point somewhere on the critical line. A sketch of the finite temperature phase diagram for the unitary Fermi gas is given in Fig. 1.4. The exact position of the tricritical point, as well as the shape of the critical curve are subjects of current research. In this work we will explore the imbalanced unitary Fermi gas close to the balanced limit and focus on the curvature of the critical curve as the imbalance tends to zero.

From the numerical point of view, studying imbalance is difficult because of the sign problem, as we shall discuss in section 4.3. The work presented here was the first numerical study of the imbalanced unitary Fermi gas at finite temperature.

1.5 Dynamical properties

Many interesting experiments with interacting Fermi gases are performed on non-equilibrium systems. Away from equilibrium one can access dynamical properties, for instance the collective excitations of a gas. In particular a lot of effort has been put into the study of spin transport phenomena in Fermi gases [33, 34, 35, 36, 37, 38]. Spin transport plays a role in astrophysics (consider for instance neutrino transport after a supernova explosion) and even in the physics of the early universe (hydrodynamic transport of quark-gluon plasma). There is also a clear parallel to electron transport which is fundamental for many modern technologies, like superconductors, semiconductors or transistors, to name just a few. So far electronics has focused on charge transport, but the electron spin might be used in a similar way as a carrier of information [39]. Either extending conventional charge-based electronic appliances by the spin degree of freedom, or using the spin alone can be the foundation for a new generation of “spintronic” devices. Advantages are for instance nonvolatility, increased data processing speed and decreased power consumption. Understanding the spin relaxation, diffusion and other transport properties is of fundamental importance in this field.

An important advantage of cold gases in studies of spin transport phenomena is the simplification due to the absence of relaxation mechanisms for spin currents apart from direct collisions between atoms of different spin, unlike e.g. in a solid where collisions with the ionic lattice can be important. The interaction strength and the temperature of the system are also easily tunable parameters as we have discussed in section 1.1. If the Fermi gas is strongly interacting the viscosity remains very low even well above the critical point, which makes it easy to experimentally reach the hydrodynamic regime. Experimental observation of different phenomena is likewise simple, as many interesting effects happen on time scales of milliseconds and can be observed in real time. Finally, as we shall see, very large spin polarisations can be easily created leading to large spin currents.

In this work we will study the spin transport properties of an interacting Fermi gas via modelling the collision of two clouds with opposite spin polarisation in an elongated harmonic trap. This study is motivated by the recent experimental results [37, 40].

The Fermi-Hubbard model at finite temperature

The Fermi-Hubbard model is the simplest lattice model for two-particle scattering. It describes non-relativistic fermions of two species, which we will label by $s \in \{\uparrow, \downarrow\}$ and call “spin up” and “spin down”. The Hamiltonian in the grand canonical ensemble is given by

$$H = H_0 + H_1 = \sum_{\mathbf{k}, s} (\epsilon_{\mathbf{k}} - \mu_s) c_{\mathbf{k}s}^\dagger c_{\mathbf{k}s} + U \sum_{\mathbf{x}} c_{\mathbf{x}\uparrow}^\dagger c_{\mathbf{x}\uparrow} c_{\mathbf{x}\downarrow}^\dagger c_{\mathbf{x}\downarrow}, \quad (2.1)$$

where $c_{\mathbf{k}s}^\dagger$ ($c_{\mathbf{k}s}$) is the time-dependent fermionic creation (annihilation) operator and $\epsilon_{\mathbf{k}} = \frac{1}{m} \sum_{j=1}^3 (1 - \cos k_j)$ the discrete dispersion relation which will be discussed in detail in section 2.1. The first part of the Hamiltonian is the kinetic term H_0 and the second part the interaction term H_1 , which represents a contact (zero-range) interaction between a spin up and a spin down particle. In the following we will assume that the fermions have equal particle mass m and will work in units where $m = 1/2$.

The attractive contact interaction is characterised by the coupling constant $U < 0$. This coupling can be tuned so that the scattering length takes infinite value, by solving the two-body problem in the same way as it was done in [26]. The corresponding value is $U = -7.914$ in units where $m = 1/2$, as will be shown in section 2.2.

We work on a 3d simple cubic spatial lattice with L^3 sites and periodic boundary conditions. The time direction remains continuous. We set the physical scale via $\nu = nb^3$, where $\nu = \langle \sum_s c_{\mathbf{x}s}^\dagger c_{\mathbf{x}s} \rangle$ is the dimensionless filling factor, n the particle density and b the lattice spacing. To return to the continuum, we change the chemical potentials μ_s such that the gas becomes more and more dilute in lattice units, $\nu \rightarrow 0$, which then tends to reproduce the continuum limit $b \rightarrow 0$. Since the leading order lattice corrections are proportional to the lattice spacing b which in turn scales like $\nu^{1/3}$, the continuum extrapolation of an observable is linear with $\nu^{1/3}$, provided that the system is dilute enough so that higher order corrections are negligible [26, 41]. The effect of lattice corrections will be discussed in more depth in section 2.3. In the following we will set the lattice spacing to unity.

2.1 Dispersion relation

The continuum dispersion relation for a free particle is $k^2/2m$, corresponding to the Fourier transform of the kinetic energy operator $-\nabla^2/2m$. The according discrete dispersion relation $\epsilon_{\mathbf{k}}$ must be a non-negative, even function in each component k_j , and due to symmetry also invariant under the permutation of the k_j . In the zero-momentum limit the discrete dispersion relation must approach the continuum one,

$$\epsilon_{\mathbf{k}} \xrightarrow[k \rightarrow 0]{} \frac{k^2}{2m} + O(k^4). \quad (2.2)$$

In this work we will use the simplest lattice dispersion relation,

$$\epsilon_{\mathbf{k}} = \frac{1}{m} \sum_{j=1}^3 (1 - \cos k_j), \quad (2.3)$$

for a better comparison with reference [26] where the same relation was used. This relation can be derived directly from the following discretisation (to leading order in lattice spacing) of the Laplace operator:

$$\nabla^2 c_s(\mathbf{x}) = \sum_{j=1}^3 (c_s(\mathbf{x} + \hat{j}) - 2c_s(\mathbf{x}) + c_s(\mathbf{x} - \hat{j})), \quad (2.4)$$

where \hat{j} denote unit vectors in the three spatial directions. We can change to the momentum space representation by expressing the fermionic fields through their discrete Fourier transforms,

$$c_s(\mathbf{x}) = \frac{1}{\sqrt{L^3}} \sum_{\mathbf{p}} c_{\mathbf{p}s} e^{i\mathbf{p}\mathbf{x}}, \quad (2.5)$$

$$c_s^\dagger(\mathbf{x}) = \frac{1}{\sqrt{L^3}} \sum_{\mathbf{p}} c_{\mathbf{p}s}^\dagger e^{-i\mathbf{p}\mathbf{x}}, \quad (2.6)$$

where the summation goes over the first Brillouin zone, $-\pi < p_j < \pi$. As a consequence of the lattice discretisation we obtained a natural momentum cut-off. The kinetic part

of the Hamiltonian $H_0 = \sum_{\mathbf{x}} c_s^\dagger(\mathbf{x}) (-\nabla^2/2m) c_s(\mathbf{x})$ then becomes

$$H_0 = \frac{1}{L^3} \sum_{\mathbf{x}} \left(-\frac{1}{2m} \right) \sum_{\mathbf{k}, \mathbf{p}} c_{\mathbf{k}s}^\dagger e^{-i\mathbf{k}\mathbf{x}} \sum_{j=1}^3 c_{\mathbf{p}s} (e^{i\mathbf{p}(\mathbf{x}+\hat{j})} - 2e^{i\mathbf{p}\mathbf{x}} + e^{i\mathbf{p}(\mathbf{x}-\hat{j})}), \quad (2.7)$$

$$= \frac{1}{L^3} \sum_{\mathbf{x}} \left(-\frac{1}{2m} \right) \sum_{\mathbf{k}, \mathbf{p}} c_{\mathbf{k}s}^\dagger c_{\mathbf{p}s} e^{i(\mathbf{p}-\mathbf{k})\mathbf{x}} \sum_{j=1}^3 (e^{ip_j} - 2 + e^{-ip_j}), \quad (2.8)$$

$$= \frac{1}{L^3} \left(-\frac{1}{2m} \right) \sum_{\mathbf{k}, \mathbf{p}} c_{\mathbf{k}s}^\dagger c_{\mathbf{p}s} L^3 \delta_{\mathbf{p}\mathbf{k}} \sum_{j=1}^3 (2 \cos p_j - 2), \quad (2.9)$$

$$= \frac{1}{m} \sum_{\mathbf{k}} c_{\mathbf{k}s}^\dagger c_{\mathbf{k}s} \sum_{j=1}^3 (1 - \cos k_j), \quad (2.10)$$

yielding the dispersion relation (2.3). It is easy to see that as we take $k \rightarrow 0$ this dispersion relation tends to the correct continuum form. At large momenta however it deviates significantly from the continuum relation. It is possible to speed the approach to the continuum limit by choosing a more complex dispersion relation, for instance by including higher orders in lattice spacing [42]. In section 2.3 we will discuss these discretisation effects in more detail.

2.2 Tuning the coupling constant

The scattering amplitude for a scattering process of two non-relativistic particles at zero temperature and chemical potential, interacting through a four-point contact interaction, can be written as a series of Feynman diagrams [26, 43]:

The Feynman rules for the diagrams are known from quantum field theory, see e.g. [44]. Note that they depend on the metric and the definition of the propagator. In the following we will use the $(1, -1, -1, -1)$ metric. The Feynman rules are:

Internal lines: propagator $G_0(\omega, \mathbf{p})$

Vertices: factor $-iU$, momentum conservation

Loops: integral over undetermined loop momentum

The total incoming (and outgoing) frequency and momentum are ω and \mathbf{p} respectively. Since the particles are non-relativistic and at zero temperature, there is no travelling

backwards in time (particle number is conserved) and hence each loop carries the same total frequency and momentum (ω, \mathbf{p}) and has no minus sign associated with it. The diagrammatic series can be rewritten in the following way

$$i\mathcal{A}(\omega, \mathbf{p}) = \text{[Four-point vertex]} + \text{[Four-point vertex with loop]}$$

which corresponds to

$$i\mathcal{A}(\omega, \mathbf{p}) = -iU + (-iU)\Pi(\omega, \mathbf{p})i\mathcal{A}(\omega, \mathbf{p}) \Leftrightarrow \mathcal{A}^{-1}(\omega, \mathbf{p}) = -U^{-1} - i\Pi(\omega, \mathbf{p}), \quad (2.11)$$

where $\Pi(\omega, \mathbf{p})$ is the one-loop integral, which will be calculated below. In the low momentum and low frequency limit the scattering amplitude is proportional to the scattering length, as we have seen in section 1.2. Hence at unitarity $\mathcal{A}^{-1}(0, \mathbf{0}) = 0$ and Eq. (2.11) becomes

$$0 = -U^{-1} - i\Pi(0, \mathbf{0}) \Rightarrow U^{-1} = -i\Pi(0, \mathbf{0}). \quad (2.12)$$

To obtain the coupling U we have to compute $\Pi(\omega, \mathbf{p})$, which is an integral over the product of two propagators. To do so, we first need to calculate the free zero temperature propagator $G_0(x - x') = \langle 0 | \mathbf{T}c(x)c^\dagger(x') | 0 \rangle$, which we obtain from the free non-relativistic Dirac Lagrangian,

$$\left(i\partial_t + \frac{\nabla^2}{2m} \right) G_0(x - y) = i\delta^{(4)}(x - y) \quad (2.13)$$

$$\Rightarrow G_0(\omega, \mathbf{p}) = \frac{i}{\omega - \mathbf{p}^2/2m + i\varepsilon}, \quad (2.14)$$

where the infinitesimal term $i\varepsilon$ specifies the contour. Accordingly, on the lattice the propagator will have the form

$$G_0(\omega, \mathbf{p}) = \frac{i}{\omega - \epsilon_{\mathbf{p}} + i\varepsilon}, \quad (2.15)$$

compare e.g. with [45, §9]. This explicit form depends on the metric. To calculate the loop integral note that the loop carries an overall four-momentum (ω, \mathbf{p}) , which is distributed over the two internal lines of the loop. Without loss of generality we can denote these two internal momenta $(\frac{\omega}{2} + \xi, \frac{\mathbf{p}}{2} + \mathbf{k})$ and $(\frac{\omega}{2} - \xi, \frac{\mathbf{p}}{2} - \mathbf{k})$, so that the loop

integration goes over ξ and \mathbf{k} ,

$$\Pi(\omega, \mathbf{p}) = \int \frac{d\xi d^3\mathbf{k}}{(2\pi)^4} G_0\left(\frac{\omega}{2} + \xi, \frac{\mathbf{p}}{2} + \mathbf{k}\right) G_0\left(\frac{\omega}{2} - \xi, \frac{\mathbf{p}}{2} - \mathbf{k}\right) \quad (2.16)$$

$$= \int \frac{d\xi d^3\mathbf{k}}{(2\pi)^4} \frac{i}{\left(\frac{\omega}{2} + \xi - \epsilon_{\frac{\mathbf{p}}{2} + \mathbf{k}} + i\varepsilon\right)} \frac{i}{\left(\frac{\omega}{2} - \xi - \epsilon_{\frac{\mathbf{p}}{2} - \mathbf{k}} + i\varepsilon\right)}. \quad (2.17)$$

We perform the $d\xi$ integration with the residue theorem. The integrand has two simple poles at $\xi_{\pm} = \pm \left(\frac{\omega}{2} - \epsilon_{\frac{\mathbf{p}}{2} \mp \mathbf{k}} + i\varepsilon\right)$. We choose the counterclockwise integration in the upper half-plane, so that the contour encloses the ξ_+ pole and get

$$\Pi(\omega, \mathbf{p}) = \int \frac{d^3\mathbf{k}}{(2\pi)^3} \frac{i}{\omega - \epsilon_{\frac{\mathbf{p}}{2} + \mathbf{k}} - \epsilon_{\frac{\mathbf{p}}{2} - \mathbf{k}}}, \quad (2.18)$$

dropping the $i\varepsilon$ insertion. Finally, inserting this result into Eq. (2.12) we get the coupling constant at unitarity,

$$U^{-1} = -i\Pi(0, \mathbf{0}) = - \int \frac{d^3\mathbf{k}}{(2\pi)^3} \frac{1}{2\epsilon_{\mathbf{k}}}. \quad (2.19)$$

For a discrete dispersion relation the integral goes over the first Brillouin zone, $-\pi < k_j < \pi$. For the relation $\epsilon_{\mathbf{k}} = (1/m) \sum_j (1 - \cos k_j)$ it can be solved numerically¹, resulting in $U \approx -7.914$ in units where $m = 1/2$.

2.3 Lattice corrections

Plugging in the expressions (2.18) and (2.19) into (2.11) we obtain an expression for the scattering amplitude at unitarity for arbitrary frequency and momentum,

$$\mathcal{A}^{-1}(\omega, \mathbf{p}) = -U^{-1} - i\Pi(\omega, \mathbf{p}) = \int \frac{d^3\mathbf{k}}{(2\pi)^3} \left(\frac{1}{2\epsilon_{\mathbf{k}}} + \frac{1}{\omega - \epsilon_{\frac{\mathbf{p}}{2} + \mathbf{k}} - \epsilon_{\frac{\mathbf{p}}{2} - \mathbf{k}}} \right). \quad (2.20)$$

The goal is to calculate how the lattice scattering amplitude $\mathcal{A}^{-1}(\omega, \mathbf{p})$ differs from the continuum scattering amplitude $\mathcal{A}_{\text{cont.}}^{-1}(\omega, \mathbf{p})$ to leading order in ω and \mathbf{p} , as this gives an estimate of the lattice corrections. To do this we expand $\mathcal{A}^{-1}(\omega, \mathbf{p})$ via a Taylor series around the origin, keeping only leading order terms. Introducing the following abbreviation for the integrand,

$$g(\omega, \mathbf{p}) = \frac{1}{2\epsilon_{\mathbf{k}}} + \frac{1}{\omega - \epsilon_{\frac{\mathbf{p}}{2} + \mathbf{k}} - \epsilon_{\frac{\mathbf{p}}{2} - \mathbf{k}}}, \quad (2.21)$$

¹One integration can be performed exactly, the remaining two numerically. The value quoted in [26] is $U \approx -7.915$.

we can write the first terms in the Taylor expansion as

$$g(\omega, \mathbf{p}) = g(0, \mathbf{0}) + \frac{\partial g}{\partial \omega} \Big|_{(0, \mathbf{0})} \omega + \sum_i \frac{\partial g}{\partial p_i} \Big|_{(0, \mathbf{0})} p_i + \sum_i \frac{\partial^2 g}{\partial \omega \partial p_i} \Big|_{(0, \mathbf{0})} \omega p_i + \frac{1}{2} \sum_{i,j} \frac{\partial^2 g}{\partial p_i \partial p_j} \Big|_{(0, \mathbf{0})} p_i p_j. \quad (2.22)$$

We kept the second order momentum terms because the linear terms vanish, as will be shown below. To calculate the derivatives of the dispersion relation we introduce the substitution $\mathbf{z}_{\pm} = \mathbf{p}/2 \pm \mathbf{k}$ such that $\partial/\partial p_i = \frac{1}{2} \partial/\partial z_{\pm i}$. After setting $\mathbf{p} = 0$ this new variable becomes $\mathbf{z}_{\pm}|_{\mathbf{p}=0} = \pm \mathbf{k}$ and hence $\epsilon_{\mathbf{z}_{\pm}}|_{\mathbf{p}=0} = \epsilon_{\mathbf{k}}$ due to symmetry. We will now proceed to calculate all the terms in the expansion. The first two terms equal

$$g(0, \mathbf{0}) = \frac{1}{2\epsilon_{\mathbf{k}}} - \frac{1}{2\epsilon_{\mathbf{k}}} = 0, \quad (2.23)$$

$$\frac{\partial g}{\partial \omega} \Big|_{(0, \mathbf{0})} \omega = \frac{-1}{\left(\omega - \epsilon_{\frac{\mathbf{p}}{2} + \mathbf{k}} - \epsilon_{\frac{\mathbf{p}}{2} - \mathbf{k}}\right)^2} \Big|_{(0, \mathbf{0})} \omega = \frac{-\omega}{(2\epsilon_{\mathbf{k}})^2}. \quad (2.24)$$

Now let us calculate the first derivative with respect to the momentum,

$$\frac{\partial g}{\partial p_i} = \frac{\frac{1}{2} (\partial \epsilon_{\mathbf{z}_+} / \partial z_{+i} + \partial \epsilon_{\mathbf{z}_-} / \partial z_{-i})}{\left(\omega - \epsilon_{\frac{\mathbf{p}}{2} + \mathbf{k}} - \epsilon_{\frac{\mathbf{p}}{2} - \mathbf{k}}\right)^2}. \quad (2.25)$$

Since $\epsilon_{\mathbf{z}_{\pm}}$ is an even function, its derivative is an odd function. Hence

$$\frac{\partial \epsilon_{\mathbf{z}_+}}{\partial z_{+i}} + \frac{\partial \epsilon_{\mathbf{z}_-}}{\partial z_{-i}} \Big|_{\mathbf{z}_{\pm} = \pm \mathbf{k}} = 0. \quad (2.26)$$

Therefore the contributions $(\partial g / \partial p_i)|_{(0, \mathbf{0})} p_i$ vanish and for the same reason the contributions $(\partial^2 g / \partial \omega \partial p_i)|_{(0, \mathbf{0})} \omega p_i$ also vanish. We have one more derivative to calculate

$$\begin{aligned} \frac{\partial^2 g}{\partial p_i \partial p_j} &= \frac{1}{4 \left(\omega - \epsilon_{\frac{\mathbf{p}}{2} + \mathbf{k}} - \epsilon_{\frac{\mathbf{p}}{2} - \mathbf{k}}\right)^4} \left[\left(\omega - \epsilon_{\frac{\mathbf{p}}{2} + \mathbf{k}} - \epsilon_{\frac{\mathbf{p}}{2} - \mathbf{k}}\right)^2 \left(\frac{\partial^2 \epsilon_{\mathbf{z}_+}}{\partial z_{+i} \partial z_{+j}} + \frac{\partial^2 \epsilon_{\mathbf{z}_-}}{\partial z_{-i} \partial z_{-j}} \right) + \right. \\ &\quad \left. + \left(\frac{\partial \epsilon_{\mathbf{z}_+}}{\partial z_{+i}} + \frac{\partial \epsilon_{\mathbf{z}_-}}{\partial z_{-i}} \right) 2 \left(\omega - \epsilon_{\frac{\mathbf{p}}{2} + \mathbf{k}} - \epsilon_{\frac{\mathbf{p}}{2} - \mathbf{k}}\right) \left(\frac{\partial \epsilon_{\mathbf{z}_+}}{\partial z_{+j}} + \frac{\partial \epsilon_{\mathbf{z}_-}}{\partial z_{-j}} \right) \right]. \quad (2.27) \end{aligned}$$

The second term in the square brackets must vanish due to (2.26). Since the second derivative of the even function $\epsilon_{\mathbf{z}_{\pm}}$ is even again, the two contributions for \mathbf{z}_+ and \mathbf{z}_-

are identical. Using this we obtain

$$\left. \frac{\partial^2 g}{\partial p_i \partial p_j} \right|_{(0,0)} = \frac{2(\partial^2 \epsilon_{\mathbf{k}} / \partial k_i \partial k_j)}{4(2\epsilon_{\mathbf{k}})^2}, \quad (2.28)$$

and putting everything together,

$$\mathcal{A}^{-1}(\omega, \mathbf{p}) = - \int \frac{d^3 \mathbf{k}}{(2\pi)^3} \left(\frac{\omega}{(2\epsilon_{\mathbf{k}})^2} - \sum_{i,j} \frac{(\partial^2 \epsilon_{\mathbf{k}} / \partial k_i \partial k_j) p_i p_j}{4(2\epsilon_{\mathbf{k}})^2} \right). \quad (2.29)$$

This formula holds generally for every symmetric dispersion relation and hence also for the continuum relation $k^2/2m$. Using this we can calculate the lattice corrections,

$$\mathcal{A}^{-1}(\omega, \mathbf{p}) - \mathcal{A}_{\text{cont.}}^{-1}(\omega, \mathbf{p}) = \frac{\omega}{4} A - \frac{p^2}{16} B, \quad (2.30)$$

where the values of the two parameters A and B are given below. Note that mixed terms proportional to $p_i p_j$ for $i \neq j$ make no contribution to the lattice corrections. The reason is the symmetry of the dispersion relation: the function $\partial^2 \epsilon_{\mathbf{k}} / \partial k_i \partial k_j$ is odd in both k_i and k_j and hence its integral over the Brillouin zone vanishes. And the second derivative $\partial^2 / \partial p_i \partial p_j$ of $p^2/2m$ is only non-vanishing for $i = j$. Explicitly we have the following expressions for the correction parameters:

$$A = \int \frac{d^3 \mathbf{k}}{(2\pi)^3} \frac{1}{(k^2/2m)^2} - \int_{\text{BZ}} \frac{d^3 \mathbf{k}}{(2\pi)^3} \frac{1}{\epsilon_{\mathbf{k}}^2}, \quad (2.31)$$

$$B = \int \frac{d^3 \mathbf{k}}{(2\pi)^3} \frac{1/m}{(k^2/2m)^2} - \int_{\text{BZ}} \frac{d^3 \mathbf{k}}{(2\pi)^3} \frac{\partial^2 \epsilon_{\mathbf{k}} / \partial k_i \partial k_i}{\epsilon_{\mathbf{k}}^2}, \quad (2.32)$$

for arbitrary $i = 1, 2, 3$, c.f. [26]. In principle the leading order lattice corrections can be completely suppressed by choosing a dispersion relation for which $A = B = 0$. Such dispersion relations do indeed exist [46], but will be not explored in this work. Comparing to the explicit expression for the effective range r_e in a lattice model [47] we see that $A = r_e m^2 / (2\pi)$. Thus $A = 0$ is equivalent to a dispersion relation with zero effective range. For the dispersion relation (2.3) the effective range equals

$$r_e = 8\pi \int_{\mathbb{R} \setminus \text{BZ}} \frac{d^3 \mathbf{k}}{(2\pi)^3} \frac{1}{k^4} + 8\pi \int_{\text{BZ}} \frac{d^3 \mathbf{k}}{(2\pi)^3} \left(\frac{1}{k^4} - \frac{1}{(2m\epsilon_{\mathbf{k}})^2} \right) = -0.3056, \quad (2.33)$$

in units of lattice spacing [47, 48]. For this dispersion relation the effective range is negative.

2.4 The finite temperature formalism

The finite temperature behaviour of a system in equilibrium is described by its partition function $Z = \text{Tr} e^{-\beta H}$, where β is the inverse temperature. Physical observables are thermal expectation values of operators, which are obtained through

$$\langle \hat{X} \rangle = \frac{\text{Tr} \hat{X} e^{-\beta H}}{Z}. \quad (2.34)$$

Note that the expression $e^{-\beta H}$ bears a similarity to the expression e^{iHt} , which often occurs in quantum field theories in relation to the time evolution operator. From quantum field theory on the other hand we know the following identity (see e.g. [44]) for the time-evolution operator $U(t)$, $t > 0$, in the interaction picture:

$$U(t) \equiv e^{iH_0 t} e^{-iHt} = \mathbf{T} \exp \left(-i \int_0^t H_1(t') dt' \right), \quad (2.35)$$

where $H_1(t)$ is the interaction part of the Hamiltonian in the interaction picture, defined by

$$H_1(t) = e^{iH_0 t} H_1 e^{-iH_0 t}, \quad (2.36)$$

and \mathbf{T} the time-ordering operator, which places operators evaluated at later times to the left. Equation (2.35) can be rewritten as

$$e^{-iHt} = e^{-iH_0 t} \mathbf{T} \exp \left(-i \int_0^t H_1(t') dt' \right). \quad (2.37)$$

To relate the two expressions e^{-iHt} and $e^{-\beta H}$ we make an analytic continuation to imaginary time, by setting all time variables $t' \rightarrow -i\tau'$ for a real $\tau' > 0$, and identifying $\tau = it$ with β . Doing so we can use (2.37) to write

$$Z = \text{Tr} e^{-\beta H} = \text{Tr} \left[e^{-\beta H_0} \mathbf{T}_\tau \exp \left(- \int_0^\beta d\tau H_1(\tau) \right) \right], \quad (2.38)$$

where \mathbf{T}_τ is now the imaginary time ordering operator that moves operators at larger values of τ to the left. The exponential in equation (2.38) can be expanded in powers of H_1 , as it is usually done in perturbation theory. Of course, we cannot neglect higher order terms for a strongly coupled system, but we can use the expansion for a Monte Carlo calculation, by randomly sampling terms in the series. Inserting the explicit form of H_1 into the expansion,

$$Z = \sum_{p=0}^{\infty} (-U)^p \sum_{\mathbf{x}_1, \dots, \mathbf{x}_p} \int_{0 < \tau_1 < \dots < \tau_p < \beta} \prod_{j=1}^p d\tau_j \text{Tr} \left[e^{-\beta H_0} \prod_{j=1}^p c_{\uparrow}^{\dagger}(\mathbf{x}_j, \tau_j) c_{\uparrow}(\mathbf{x}_j, \tau_j) c_{\downarrow}^{\dagger}(\mathbf{x}_j, \tau_j) c_{\downarrow}(\mathbf{x}_j, \tau_j) \right], \quad (2.39)$$

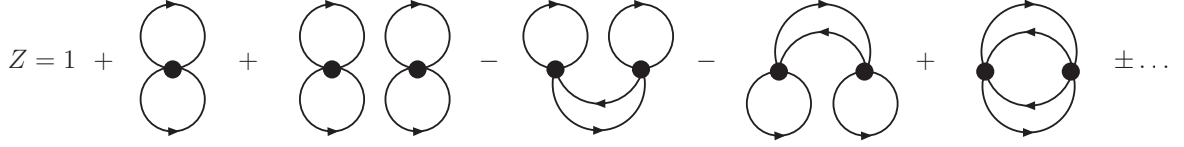


Figure 2.1: Diagrammatic expansion of the partition function

generates a series of Feynman diagrams, as shown in Fig. 2.1. The diagrams consist of four-point vertices representing a factor of $(-U)$ and lines representing a free finite temperature single-particle propagator [45],

$$G_{(0)}^s(\mathbf{x}_i - \mathbf{x}_j, \tau_i - \tau_j) \equiv -\langle \mathbf{T}_\tau c_{\mathbf{x}_i s}^\dagger(\tau_i) c_{\mathbf{x}_j s}(\tau_j) \rangle \quad (2.40)$$

$$= -\text{Tr}[\mathbf{T}_\tau e^{-\beta H_0} c_{\mathbf{x}_i s}^\dagger(\tau_i) c_{\mathbf{x}_j s}(\tau_j)], \quad (2.41)$$

resulting from contractions between the fermionic operators. Lines in the upper half-plane belong to spin up and lines in the lower half-plane to spin down propagators respectively. Additionally, each closed fermionic loop carries a minus sign due to the fermionic anticommutation relations. Therefore diagrams with an even and those with an odd number of loops have different signs. This makes a direct sampling of the individual diagrams difficult, since a series of terms with alternating signs fluctuates and the error of the numerical calculation is bound to be large. In a certain case however, this sign problem can be avoided, as we shall prove in the next section. The explicit form of the propagator (2.40) is given by [49]

$$G_{(0)}^s(\mathbf{k}, \tau \equiv \tau_j - \tau_i) = \begin{cases} e^{-(\epsilon_{\mathbf{k}} - \mu_s)\tau} (1 - n_{\mathbf{k}s}) & \text{for } \tau > 0 \\ -e^{-(\epsilon_{\mathbf{k}} - \mu_s)\tau} n_{\mathbf{k}s} & \text{for } \tau \leq 0 \end{cases}, \quad (2.42)$$

where $n_{\mathbf{k}s} = (1 + e^{\beta(\epsilon_{\mathbf{k}} - \mu_s)})^{-1}$ is the occupation of the state (\mathbf{k}, s) for free fermions at inverse temperature β . In the case of equal chemical potentials for spin up and spin down, $n_{\mathbf{k}s}$ does not depend on s . The spatial representation of the Green's function can be obtained by an appropriate Fourier transform.

2.5 Matrix notation

To avoid the sign problem mentioned in the previous section, we will group the diagrams of the expansion of Z in a clever way [50]. Consider the two parts of a Feynman diagram corresponding to spin up and spin down separately. As the spin up and the spin down contributions are independent each diagram can be decomposed as a product of its spin up and spin down components. The set of all diagrams of a certain order is the sum of all such possible products.

Now take the entity of all diagrams of arbitrary order p and consider only one

of the two components with spin s . Every such diagram component has p vertices at positions x_1, \dots, x_p , each with an outgoing and an incoming line, which have to be joined together somehow. We can write the set of all possible combinations of how these lines can be connected as a $p \times p$ matrix A^s , where the matrix element A_{ij}^s denotes a free single-particle propagator (2.40) going from x_i to x_j ,

$$A_{ij}^s = G_{(0)}^s(\mathbf{x}_i - \mathbf{x}_j, \tau_i - \tau_j), \quad i, j = 1, \dots, p, \quad (2.43)$$

or in other words, a connection from the outgoing line of vertex i to the incoming line of vertex j . In this notation, each single diagram corresponds to the product of p elements of the matrix A^s , with the condition that we must choose one and only one element from each row and column of the matrix. This condition incorporates the fact that each vertex has one and only one incoming and outgoing spin s line respectively. Such a choice of matrix elements can be written as $\{A_{i\sigma(i)}^s | i = 1, \dots, p\}$, where $\sigma \in \Sigma_p$ is some permutation of the integers $1, \dots, p$ (an element of the permutation group Σ_p). This permutation uniquely determines the form of the diagram.

Additionally, each loop brings a minus sign. We need a prescription how to determine the overall sign of a diagram from the permutation σ . To achieve this consider first a random permutation and then swap two of its elements. In terms of diagrams this means the following: If the two corresponding vertices belonged to the same spin s loop, this loop gets broken up in two separate loops; if they belonged to two different loops, these loops get joined together. In any case the number of loops changes by one, which means a change in the overall sign of the diagram. Mathematically on the other hand, such a swap means a change of the signature of the permutation. So depending on the diagram order p the overall sign of any diagram σ of this order is either $\text{sgn}(\sigma)$ or $-\text{sgn}(\sigma)$. To find out which of the two is the case, consider the identity permutation, which corresponds to a diagram where each vertex is connected only to itself. This means that there are p (spin s) loops. If p is even, such a diagram has sign $+1$, and if p is odd, it has sign -1 . In total we can write each diagram as $(-1)^p \text{sgn}(\sigma) \prod_i A_{i\sigma(i)}^s$. Now it is easy to see that summing all diagrams of one order we simply obtain the determinant of the matrix A^s :

$$\sum_{\sigma \in \Sigma_p} (-1)^p \text{sgn}(\sigma) \prod_{i=1}^p A_{i\sigma(i)}^s = (-1)^p \det A^s. \quad (2.44)$$

Putting the two spin components together we get an expression for the contribution of all diagrams of a given order p ,

$$(-1)^{2p} \det A^\uparrow \det A^\downarrow = \det A^\uparrow \det A^\downarrow, \quad (2.45)$$

where A^\uparrow comes from the spin up part and A^\downarrow from the spin down part of the diagrams.

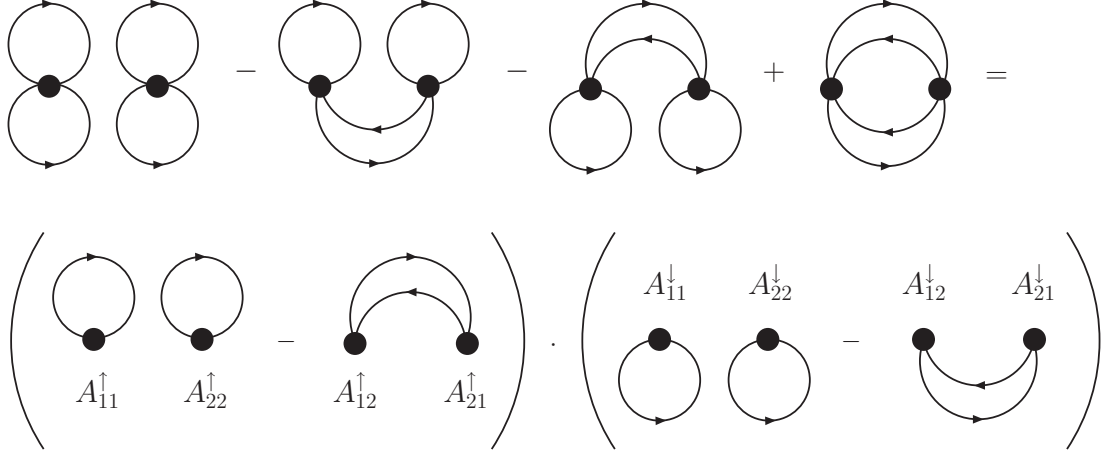


Figure 2.2: Decomposition of the sum of all $p = 2$ diagrams into a product of two matrix determinants.

Hence we have represented the contribution from all diagrams of a certain order p as a product of two matrix determinants, one for each species of spin. An example of such a representation for $p = 2$ is given in Fig. 2.2.

Now it is easy to see how this formalism can help with the sign problem. If the number of spin up and spin down particles is equal ($\mu_{\uparrow} = \mu_{\downarrow}$) then so are the Green's functions (2.42) for the two components and consequently also all corresponding matrix elements. In this case we have $\det A^{\uparrow} \det A^{\downarrow} = |\det A|^2$, which is always positive. Hence we have represented the partition function as a series of only positive terms.

Another advantage of this formalism is that we do not need to consider individual diagrams, but obtain the contribution from all diagrams of a given order p and at a given set of spacetime positions for the vertices (vertex configuration) at once. If we label a vertex configuration as $S_p = \{(\mathbf{x}_j, \tau_j) | j = 1, \dots, p\}$, the expansion of Z takes the form

$$Z = \sum_{p=0}^{\infty} \sum_{S_p} (-U)^p \det A^{\uparrow}(S_p) \det A^{\downarrow}(S_p), \quad (2.46)$$

where summation goes over all diagram orders p and vertex configurations S_p ,

$$\sum_{S_p} \equiv \sum_{\mathbf{x}_1, \dots, \mathbf{x}_p} \int_{0 < \tau_1 < \dots < \tau_p < \beta} \prod_{j=1}^p d\tau_j. \quad (2.47)$$

This summation, together with the summation over p will be performed stochastically via a Monte Carlo algorithm. To obtain physically relevant quantities we need to compute expectation values over Z rather than Z itself. These can however be expanded in a similar way, which will be illustrated on an example in section 4.1.

Order parameter and finite-size scaling

To calculate the critical temperature we need to introduce an order parameter which distinguishes between the normal and the superfluid phase. The latter is characterised through the presence of anomalous correlations, in our case between pairs of fermions with opposite spin, as these are the relevant degrees of freedom of the system. We therefore first introduce the pair creation and annihilation operators

$$P^\dagger(\mathbf{x}, \tau) = c_{\mathbf{x}\uparrow}^\dagger(\tau)c_{\mathbf{x}\downarrow}^\dagger(\tau), \quad (3.1)$$

$$P(\mathbf{x}, \tau) = c_{\mathbf{x}\uparrow}(\tau)c_{\mathbf{x}\downarrow}(\tau), \quad (3.2)$$

and their two-point correlation function

$$G_2(\mathbf{x}, \tau; \mathbf{x}', \tau') = \langle \mathbf{T}_\tau P(\mathbf{x}, \tau) P^\dagger(\mathbf{x}', \tau') \rangle \quad (3.3)$$

$$= \frac{1}{Z} \text{Tr}[\mathbf{T}_\tau P(\mathbf{x}, \tau) P^\dagger(\mathbf{x}', \tau') e^{-\beta H}]. \quad (3.4)$$

For an infinite system the correlation function at the critical point decays as a power law at large separations $|\mathbf{x} - \mathbf{x}'| \rightarrow \infty$,

$$G_2(\mathbf{x}, \tau; \mathbf{x}', \tau') \propto \frac{1}{|\mathbf{x} - \mathbf{x}'|^{d-2+\eta}}, \quad (3.5)$$

where $d = 3$ is the number of spatial dimensions and $\eta \approx 0.038$ [51, 52] is the anomalous dimension for the U(1) universality class. In our analysis we are limited to finite systems characterised by the lattice size L . Finite-size effects distort the location of the critical point by shifting the critical temperature to another “pseudocritical” value [53]. Hence we need a prescription how to obtain T_c in the thermodynamic limit from the lattice data.

The finite-size scaling hypothesis [53, 54] states that near the critical point the behaviour of a finite system is determined by the dimensionless ratio L/ξ_∞ between the finite-size scale L and the correlation length of the infinite system ξ_∞ . From the renormalisation group framework we know that as we approach the critical point the correlation length diverges as $\xi_\infty \propto |t|^{-\nu_\xi}$ for a second order phase transition, where $t = (T - T_c)/T_c$ and ν_ξ is a universal critical exponent. Hence the scale ratio L/ξ_∞ is

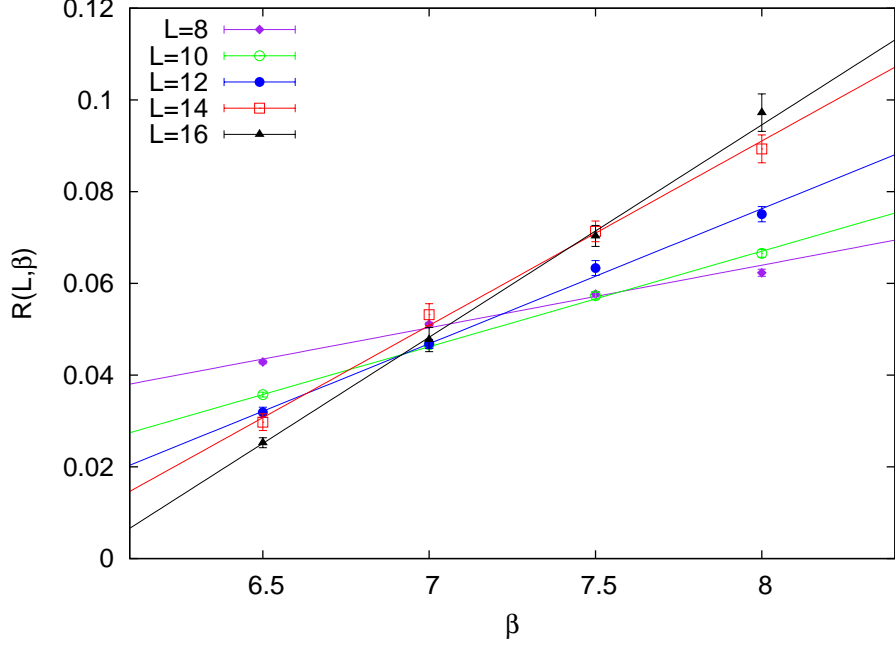


Figure 3.1: Example plot of $R(L, \beta)$ as a function of the inverse lattice temperature β near the critical point for different values of lattice size L . This data was taken at the lattice chemical potential $\mu = 0.4$. The lines are linear fits of the data. Due to corrections from irrelevant operators the fits do not cross in the same point.

proportional to $L|t|^{\nu_\xi}$ near the critical point. The finite-size dependence will thus be represented by a universal scaling function with the argument $L|t|^{\nu_\xi}$, or equivalently by another scaling function with the argument $x = tL^{1/\nu_\xi}$.

For instance let us look at the average of G_2 over space and imaginary time,

$$K(L, T) = (\beta L^3)^{-2} \sum_{\mathbf{x}, \mathbf{x}'} \int_0^\beta d\tau \int_0^\beta d\tau' G_2(\mathbf{x}, \tau; \mathbf{x}', \tau'), \quad (3.6)$$

which is the analogue of the susceptibility [52]. Because of the power law decay (3.5) it is clear from dimensional arguments that $K(L, T)$ must scale like $L^{-(1+\eta)}$. We therefore define the rescaled averaged correlation function

$$R(L, T) = L^{1+\eta} (\beta L^3)^{-2} \sum_{\mathbf{x}, \mathbf{x}'} \int_0^\beta d\tau \int_0^\beta d\tau' G_2(\mathbf{x}, \tau; \mathbf{x}', \tau'). \quad (3.7)$$

Leaving aside corrections due to irrelevant operators for the time being, $R(L, T)$ near the critical point must be a purely universal scaling function of $x = tL^{1/\nu_\xi}$, analytic at $x = 0$. Hence if no corrections due to irrelevant operators were present, $R(L, T)$ would be independent of the lattice size L at the critical point $t = 0$. In this case, all $R(L, T)$ curves for different values of L would cross in a single point.

By looking at the example plot in Fig. 3.1 we can see that this is not the case. This

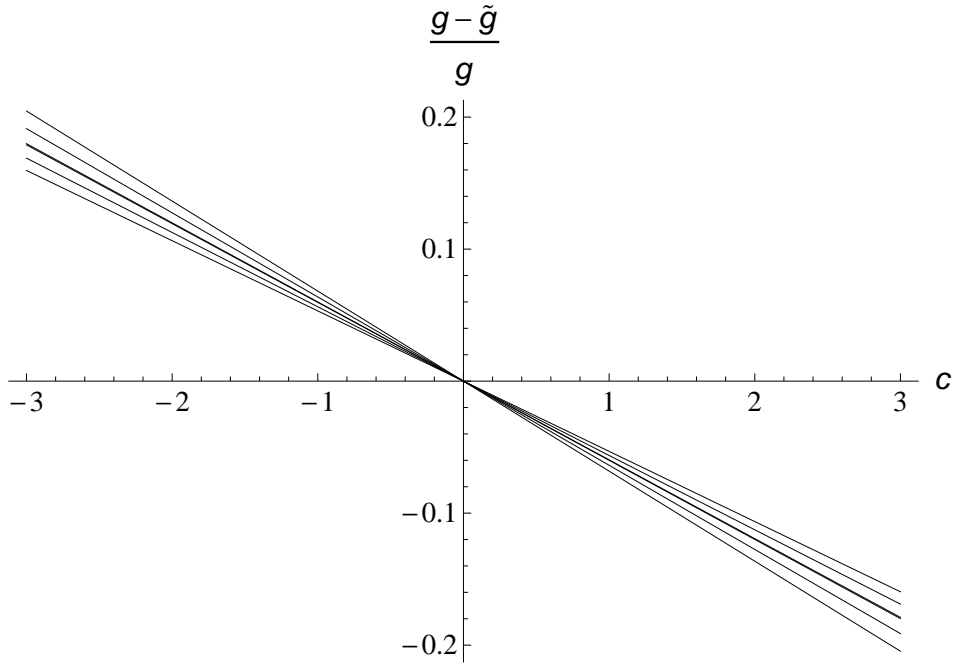


Figure 3.2: The relative difference $(g(L_i, L_j) - \tilde{g}(L_i, L_j))/g(L_i, L_j)$ as a function of c (in lattice units), for several values of L_i and L_j ranging between 10 and 16.

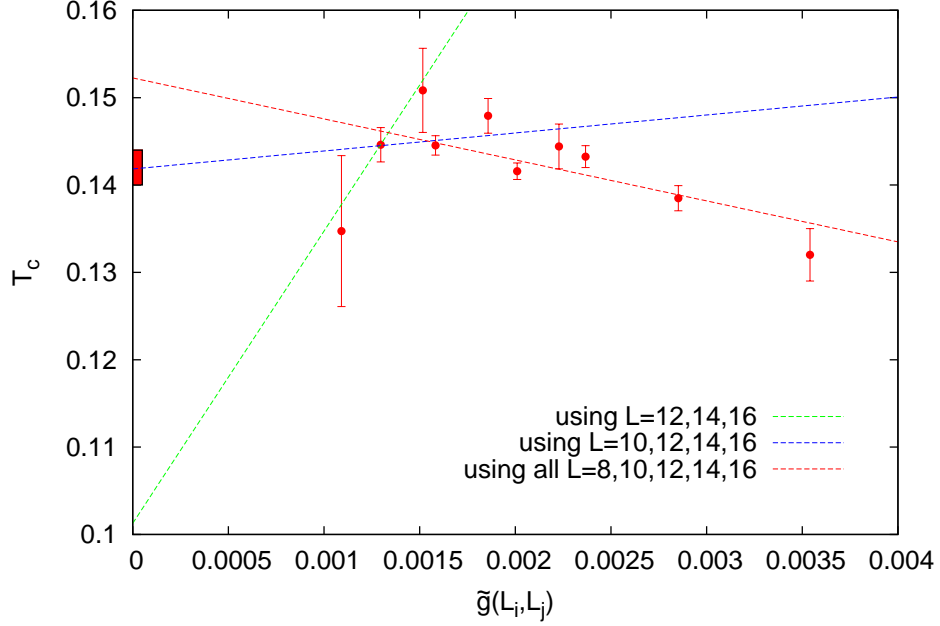


Figure 3.3: The crossing temperatures (in lattice units) for different pairs of lattice sizes for the system from Fig. 3.1 as a function of $\tilde{g}(L_i, L_j)$. A linear dependence is not visible. The lines represent fits through different subsets of points. For comparison, the red box is the continuum value (with error) obtained with the improved method, which gives consistent results independent of the lattice size range.

effect is due to corrections coming from the irrelevant operators. Apart from the operators present in the original Hamiltonian any renormalisation group transformation introduces a potentially infinite hierarchy of additional operators with corresponding coupling constants. These operators are also associated with universal critical exponents under the renormalisation group flow. If the exponents are negative then the contribution of the operator vanishes at the critical point. In this case the operator is called irrelevant [53, 54]. Nevertheless, for finite-size systems the contribution from these operators can become significant, for instance if the critical exponent is close to zero. Taking the leading order correction into account, the function $R(L, T)$ near the critical point can be written as a product of the universal scaling function $f(tL^{1/\nu_\xi})$ and a correction term due to irrelevant operators,

$$R(L, T) = f(tL^{1/\nu_\xi})(1 + cL^{-\omega} + \dots), \quad (3.8)$$

where c is a non-universal constant and ω another universal critical exponent. The values of the critical exponents can be determined to high precision with various methods, see e.g. [51, 52], and for our model equal $\nu_\xi \approx 0.67$ and $\omega \approx 0.8$. Near the critical point we can expand Eq. (3.8) in powers of the rescaled temperature t and keeping only terms linear in t and the leading order correction from irrelevant operators we obtain

$$R(L, T) = (f_0 + f_1(T - T_c)L^{1/\nu_\xi})(1 + cL^{-\omega}). \quad (3.9)$$

Previous work [26, 23] used a two-step procedure for determining T_c from this equation. This procedure is based on the observation that although the crossings of the $R(L, T)$ curves do not occur exactly at T_c they are nevertheless close to the critical point for sufficiently large L . By equating $R(L_i, T_{ij}) = R(L_j, T_{ij})$ and using Eq. (3.9), a relation between T_c and the crossing temperatures T_{ij} can be derived,

$$T_{ij} - T_c = \kappa g(L_i, L_j), \quad (3.10)$$

where

$$g(L_i, L_j) = \frac{(L_j/L_i)^\omega - 1}{L_j^{\frac{1}{\nu_\xi} + \omega} \left(1 - (L_i/L_j)^{\frac{1}{\nu_\xi}}\right) + cL_j^{\frac{1}{\nu_\xi}} \left(1 - (L_i/L_j)^{\frac{1}{\nu_\xi} - \omega}\right)}, \quad (3.11)$$

and $\kappa = cf_0/f_1$ is a non-universal constant. Note that the second term in the denominator of (3.11) also contains the non-universal constant c . In the references [26] and [23] this term is neglected, so that the second step of the procedure simplifies to a linear fit of the crossing temperatures T_{ij} to the function

$$\tilde{g}(L_i, L_j) = \frac{(L_j/L_i)^\omega - 1}{L_j^{\frac{1}{\nu_\xi} + \omega} \left(1 - (L_i/L_j)^{\frac{1}{\nu_\xi}}\right)}. \quad (3.12)$$

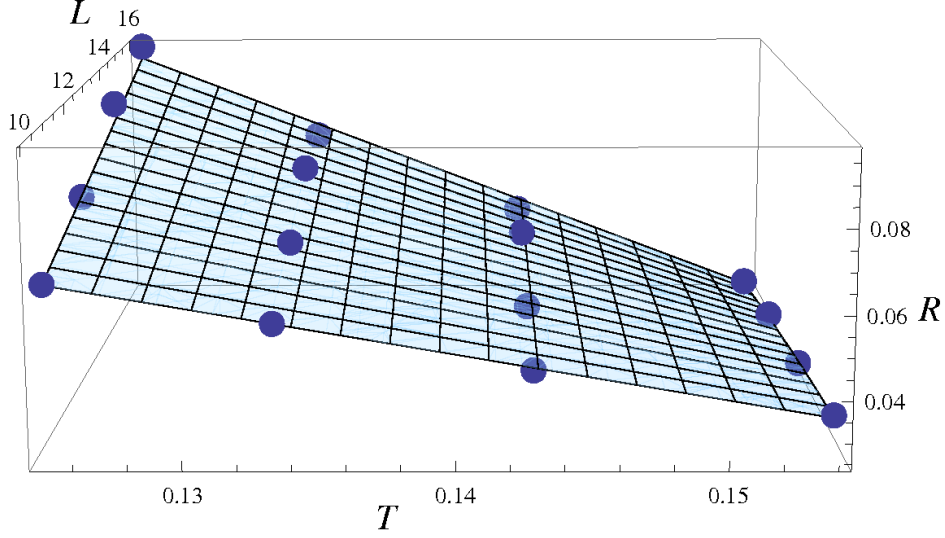


Figure 3.4: A typical fit of the rescaled correlation function $R(L, T)$ according to Eq. (3.9). Here data was taken at four different lattices sizes and temperatures. For this fit $\chi^2/\text{d.o.f.} = 1.4$. The value for c was found to be $-1.4(5)$. All quantities are given in lattice units.

The critical temperature is the intercept of this fit. This simplification is justified if the constant c is sufficiently small. But if c assumes values of order of unity the systematic error associated with this approximation can reach up to 20%, as shown in Fig. 3.2. In this case obtaining a good linear fit of the crossing temperatures is no longer possible. An example is shown in Fig. 3.3, where the crossings from the curves depicted in Fig. 3.1 were used. No linear dependence of the crossing temperatures on \tilde{g} is visible, moreover depending on which values for L are included in the fit the extrapolations yield very different values for $T_c(L \rightarrow \infty)$.

To avoid this systematic uncertainty we propose a different procedure for extracting T_c from the numerical data. In our analysis we use Eq. (3.9) directly to fit all data triplets (R, L, T) to a single function. An example of such a non-linear fit is shown in Fig. 3.4, where we used the same system as for the Figures 3.1 and 3.3. The new procedure has several advantages. Firstly, the previously described systematic error is no longer present, which can become relevant, since we found $|c| > 1$ in several cases (see Sec. 6.2 for a detailed analysis). Secondly, all information obtained from the simulations is used for the data analysis. In the original two-step procedure the (R, T) tuples for each L were fitted to a line separately, which involved two unknown parameters for each value of L . After the crossings of these lines were determined, the information about the values of R could no longer be used for the next stage of the analysis. From the crossings another linear fit involving two unknown parameters had to be made. For our example from Fig. 3.4 with 16 datapoints, the original procedure would require four independent linear fits (8 parameters) and another linear fit into

which the errors of the previous fits propagate. The new method suggested here only requires a single non-linear fit of 4 parameters: f_0 , f_1 , c and T_c , of which only T_c is of interest.

We made several consistency checks of the new method. We established that the fit procedure gives consistent results, independent of which combinations of lattice sizes are included in the fit, provided that all L are sufficiently large. We also confirmed that the fit results agree if we include second order corrections in t and $L^{-\omega}$. For the final results however only leading order terms were used. Also the fits are insensitive to the precise values of the critical exponents, so that we can safely neglect the small errors associated with their numerical determination.

The value for T_c obtained through this procedure is in lattice units and needs to be translated into physical units. Since the only physical length scale at unitarity is determined by the density, the corresponding physical quantity has to be T_c/ε_F , where the Fermi energy is defined as $\varepsilon_F = (3\pi^2\nu)^{2/3}$. In the grand canonical ensemble the chemical potential is fixed and the corresponding filling factor ν is measured for different values of lattice size. For sufficiently large lattices the values $\nu(L)$ scale linearly with $1/L$ and an extrapolation to $1/L \rightarrow 0$ will yield the thermodynamic limit for the filling factor at a given chemical potential [26]. This value will be used to determine ε_F . Finally, as we discussed, the continuum limit for the critical temperature T_c/ε_F is taken by extrapolating to $\nu \rightarrow 0$.

Diagrammatic Monte Carlo sampling

4.1 Formalism

We will now introduce the mathematical formalism that will allow us to apply Monte Carlo importance sampling techniques to the diagrammatic expansions of the partition function and thermal expectation values. In section 2.5 we established the matrix notation for the expansion of the partition function. The same formalism can be applied to thermal averages of operators,

$$\langle \hat{X} \rangle = \frac{1}{Z} \text{Tr}[\hat{X} e^{-\beta H}], \quad (4.1)$$

which correspond to physical observables. The diagrammatic expansion of $\text{Tr}[\hat{X} e^{-\beta H}]$ will have a similar form as the one for Z , but will contain additional vertices due to contractions with the creation and annihilation operators of which \hat{X} is composed. The general form of a diagrammatic expansion of an observable $X = \langle \hat{X} \rangle$ can be written as

$$X = \frac{1}{Z} \sum_{p, S_p} \mathcal{D}^{(X)}(S_p), \quad (4.2)$$

where summation goes over all diagram orders p and vertex configurations S_p . The diagram corresponding to the vertex configuration S_p is denoted by $\mathcal{D}^{(X)}(S_p)$. Instead of uniformly sampling the configuration space and calculating the sum, an efficient Monte Carlo simulation will make use of importance sampling and create the configurations S_p according to their natural probability distribution, which is given by the expansion of the partition function:

$$\rho(S_p) = \frac{1}{Z} \mathcal{D}^{(Z)}(S_p). \quad (4.3)$$

Dividing by $Z = \sum_{p, S_p} \mathcal{D}^{(Z)}(S_p)$ ensures normalisation and

$$\mathcal{D}^{(Z)}(S_p) = (-U)^p \det A^\dagger(S_p) \det A^\downarrow(S_p), \quad (4.4)$$

as given by equation (2.46). We can write

$$X = \frac{1}{Z} \sum_{p, S_p} \mathcal{D}^{(X)}(S_p) = \sum_{p, S_p} \frac{\mathcal{D}^{(X)}(S_p)}{\mathcal{D}^{(Z)}(S_p)} \frac{\mathcal{D}^{(Z)}(S_p)}{Z} = \sum_{p, S_p} \frac{\mathcal{D}^{(X)}(S_p)}{\mathcal{D}^{(Z)}(S_p)} \rho(S_p). \quad (4.5)$$

If we create the configurations S_p according to the probability distribution $\rho(S_p)$, we get an estimator for the observable X through

$$X = \left\langle \frac{\mathcal{D}^{(X)}(S_p)}{\mathcal{D}^{(Z)}(S_p)} \right\rangle_\rho \equiv \langle \mathcal{Q}^{(X,Z)} \rangle_\rho, \quad (4.6)$$

where $\langle \dots \rangle_\rho$ stands for averaging over a sequence of Monte Carlo vertex configurations, created according to the probability distribution $\rho(S_p)$ and

$$\mathcal{Q}^{(X,Z)}(S_p) = \frac{\mathcal{D}^{(X)}(S_p)}{\mathcal{D}^{(Z)}(S_p)}. \quad (4.7)$$

Since the terms $\mathcal{D}^{(X)}(S_p)$ in the diagrammatic expansion of a physical observable are of a similar form as $\mathcal{D}^{(Z)}(S_p)$, the terms in the expansion of the partition function, we can expect cancellations, so that the Monte Carlo estimator $\mathcal{Q}^{(X,Z)}(S_p)$ will have a simple form. To illustrate this we consider as an example the estimator for the filling factor

$$\nu = \sum_s \langle c_{\mathbf{x}s}^\dagger(\tau) c_{\mathbf{x}s}(\tau) \rangle = \frac{1}{Z} \sum_s \text{Tr} [c_{\mathbf{x}s}^\dagger(\tau) c_{\mathbf{x}s}(\tau) e^{-\beta H}], \quad (4.8)$$

where due to translational invariance (\mathbf{x}, τ) can be an arbitrary spacetime point [26]. The diagrammatic expansion of the trace is similar to the expansion of the partition function, the only difference being the two additional operators $c_{\mathbf{x}s}^\dagger(\tau)$ and $c_{\mathbf{x}s}(\tau)$, which can also form contractions with the operators coming from the expansion of the Hamiltonian. It is easy to see that the corresponding diagrams have the form

$$\mathcal{D}^{(\nu)}(S_p) = \sum_s (-U)^p \det B^s(S_p, \mathbf{x}, \tau) \det A^{\bar{s}}(S_p), \quad (4.9)$$

where s and \bar{s} are opposite spin indices. The free Green's function matrix $A^{\bar{s}}$ is the same as in the expansion of Z and the matrix B^s is formed from the matrix A^s by addition of an extra row and an extra column, originating from contractions with the operators $c_{\mathbf{x}s}^\dagger(\tau)$ and $c_{\mathbf{x}s}(\tau)$. The Monte Carlo estimator of the number density is consequently given by the ratio of two determinants,

$$\mathcal{Q}^{(\nu,Z)}(S_p) = \frac{\mathcal{D}^{(\nu)}(S_p)}{\mathcal{D}^{(Z)}(S_p)} = \sum_s \frac{\det B^s(S_p, \mathbf{x}, \tau)}{\det A^s(S_p)}. \quad (4.10)$$

Monte Carlo estimators for other thermodynamic observables can be obtained in an analogous way.

4.2 Extending the configuration space

As we will elaborate in the next chapter, one of the core ideas of the algorithm is the extension of the space of allowed vertex configurations S_p . Mathematically, this means extending the domain on which the sampling probability distribution is defined. In this section we will develop the corresponding mathematical formalism. Let us call the initial domain $\mathfrak{S}^{(Z)}$ and the extended domain $\mathfrak{S}^{(Z_W)} = \mathfrak{S}^{(Z)} \cup \mathfrak{S}^{(G)}$. Then we define the extended probability distribution to be

$$\mathcal{D}^{(Z_W)}(S_p) = \begin{cases} \mathcal{D}^{(Z)}(S_p) & \text{for } S_p \in \mathfrak{S}^{(Z)} \\ \mathcal{D}^{(G)}(S_p) & \text{for } S_p \in \mathfrak{S}^{(G)} \end{cases} \quad (4.11)$$

in terms of the diagrammatic expansion. Apart from normalisation the probability distribution stays the same on the initial domain. Taking normalisation into account:

$$\rho_W(S_p) \equiv \frac{1}{Z_W} \mathcal{D}^{(Z_W)}(S_p) = \begin{cases} \rho(S_p) Z / Z_W & \text{for } S_p \in \mathfrak{S}^{(Z)} \\ \rho_G(S_p) & \text{for } S_p \in \mathfrak{S}^{(G)} \end{cases}, \quad (4.12)$$

where $Z = \sum_{\mathfrak{S}^{(Z)}} \mathcal{D}^{(Z)}(S_p)$ and $Z_W = \sum_{\mathfrak{S}^{(Z_W)}} \mathcal{D}^{(Z_W)}(S_p)$. In other words, the new probability distribution on $\mathfrak{S}^{(Z)}$ is obtained from the original one by reweighting with the ratio of the measures of the old and the new domains.

Thermal averages must stay invariant under this extension, to ensure that the physical predictions are still valid. If the observable X is defined on $\mathfrak{S}^{(Z)}$ only, we extend it to $\mathfrak{S}^{(Z_W)}$ by setting $\mathcal{D}^{(X)}(S_p) = 0 \quad \forall S_p \in \mathfrak{S}^{(G)}$. This implies

$$\frac{\mathcal{D}^{(X)}(S_p)}{\mathcal{D}^{(Z)}(S_p)} = \frac{\mathcal{D}^{(X)}(S_p)}{\mathcal{D}^{(Z_W)}(S_p)} \quad (4.13)$$

$$\Rightarrow \mathcal{Q}^{(X,Z)}(S_p) = \mathcal{Q}^{(X,Z_W)}(S_p) \quad \forall S_p \in \mathfrak{S}^{(Z_W)}. \quad (4.14)$$

Applying (4.12) and (4.13) to (4.5) we can estimate X through

$$X = \sum_{p, S_p} \frac{\mathcal{D}^{(X)}(S_p)}{\mathcal{D}^{(Z_W)}(S_p)} \rho_W(S_p) \frac{Z_W}{Z} = \frac{Z_W}{Z} \langle \mathcal{Q}^{(X,Z_W)} \rangle_{\rho_W}. \quad (4.15)$$

As far as the partition function Z is concerned,

$$Z = \sum_{p, S_p} \mathcal{D}^{(Z)}(S_p) = Z_W \sum_{p, S_p} \frac{\mathcal{D}^{(Z)}(S_p)}{\mathcal{D}^{(Z_W)}(S_p)} \frac{\mathcal{D}^{(Z_W)}(S_p)}{Z_W} = Z_W \langle \mathcal{Q}^{(Z,Z_W)} \rangle_{\rho_W}, \quad (4.16)$$

and hence

$$\frac{Z}{Z_W} = \langle \mathcal{Q}^{(Z, Z_W)} \rangle_{\rho_W}. \quad (4.17)$$

But since

$$\mathcal{D}^{(Z)}(S_p) = \begin{cases} \mathcal{D}^{(Z_W)}(S_p) & \text{for } S_p \in \mathfrak{S}^{(Z)} \\ 0 & \text{for } S_p \in \mathfrak{S}^{(G)} \end{cases} \quad (4.18)$$

we obtain a very simple form for the corresponding Monte Carlo estimator,

$$\mathcal{Q}^{(Z, Z_W)}(S_p) = \begin{cases} 1 & \text{for } S_p \in \mathfrak{S}^{(Z)} \\ 0 & \text{for } S_p \in \mathfrak{S}^{(G)} \end{cases} \quad (4.19)$$

Now we have all the necessary preliminaries to estimate physical observables on the extended domain:

$$X = \langle \mathcal{Q}^{(X, Z)} \rangle_{\rho} = \frac{Z_W}{Z} \langle \mathcal{Q}^{(X, Z_W)} \rangle_{\rho_W} = \frac{\langle \mathcal{Q}^{(X, Z_W)} \rangle_{\rho_W}}{\langle \mathcal{Q}^{(Z, Z_W)} \rangle_{\rho_W}}. \quad (4.20)$$

4.3 Sampling with a different distribution

The original DDMC algorithm relies strongly on the assumption of equal densities of the two fermionic species. This assumption allows us to write the partition function (2.46) as a sum of positive terms only, and consequently to use it as a probability distribution for Monte Carlo sampling. In the presence of an imbalance $\mu_{\uparrow} \neq \mu_{\downarrow}$ a generalisation of the algorithm is necessary, as the diagrams $\mathcal{D}^{(Z)}(S_p)$ no longer need to be positive and hence $\rho(S_p)$ ceases to be a well-defined probability distribution. This forces us to use a different distribution for Monte Carlo sampling. The mathematical formalism for sampling with respect to a different probability distribution $\rho'(S_p) = \frac{1}{Z'} \mathcal{D}^{(Z')}(S_p)$, defined on the same domain as $\rho(S_p)$, will be introduced in this section. Proceeding as in (4.5) we can write

$$X = \frac{Z'}{Z} \sum_{p, S_p} \frac{\mathcal{D}^{(X)}(S_p)}{\mathcal{D}^{(Z')}(S_p)} \rho'(S_p) = \frac{Z'}{Z} \langle \mathcal{Q}^{(X, Z')} \rangle_{\rho'}. \quad (4.21)$$

To obtain an expression for the prefactor consider the diagrammatic expansion of Z in terms of the new distribution $\rho'(S_p)$

$$Z = \sum_{p, S_p} \mathcal{D}^{(Z)}(S_p) = Z' \sum_{p, S_p} \frac{\mathcal{D}^{(Z)}(S_p)}{\mathcal{D}^{(Z')}(S_p)} \rho'(S_p) \Rightarrow \frac{Z}{Z'} = \langle \mathcal{Q}^{(Z, Z')} \rangle_{\rho'}. \quad (4.22)$$

Consequently

$$X = \frac{\langle \mathcal{Q}^{(X, Z')} \rangle_{\rho'}}{\langle \mathcal{Q}^{(Z, Z')} \rangle_{\rho'}}, \quad (4.23)$$

which is analogous to (4.20). Finally, as discussed in section 4.2, we can extend the modified probability distribution $\rho'(S_p)$ to $\rho'_W(S_p)$ on a larger domain, in the same way as we did for $\rho(S_p)$. We obtain using (4.20),

$$\langle \mathcal{Q}^{(X,Z')} \rangle_{\rho'} = \frac{\langle \mathcal{Q}^{(X,Z'_W)} \rangle_{\rho'_W}}{\langle \mathcal{Q}^{(Z',Z'_W)} \rangle_{\rho'_W}} \quad (4.24)$$

and

$$\langle \mathcal{Q}^{(Z,Z')} \rangle_{\rho'} = \frac{\langle \mathcal{Q}^{(Z,Z'_W)} \rangle_{\rho'_W}}{\langle \mathcal{Q}^{(Z',Z'_W)} \rangle_{\rho'_W}}, \quad (4.25)$$

and inserting everything into equation (4.23),

$$X = \frac{\langle \mathcal{Q}^{(X,Z'_W)} \rangle_{\rho'_W}}{\langle \mathcal{Q}^{(Z',Z'_W)} \rangle_{\rho'_W}} \frac{\langle \mathcal{Q}^{(Z',Z'_W)} \rangle_{\rho'_W}}{\langle \mathcal{Q}^{(Z,Z'_W)} \rangle_{\rho'_W}} = \frac{\langle \mathcal{Q}^{(X,Z'_W)} \rangle_{\rho'_W}}{\langle \mathcal{Q}^{(Z,Z'_W)} \rangle_{\rho'_W}}. \quad (4.26)$$

To avoid the sign problem an obvious choice for an alternative distribution is the “sign quenched” distribution. The idea is based on the “phase quenched method” known from lattice QCD [55]. We can write the function $\rho_W(S_p)$ as a product of its modulus and its sign,

$$\rho_W(S_p) = \frac{1}{Z_W} (-U)^p |\det A^\dagger(S_p) \det A^\dagger(S_p)| \text{sgn}(S_p), \quad (4.27)$$

and use the positive function

$$\rho'_W(S_p) \equiv \frac{1}{Z'_W} (-U)^p |\det A^\dagger(S_p) \det A^\dagger(S_p)| \quad (4.28)$$

as the new probability distribution. Using equation (4.26) we can immediately read off the general expression for a thermal average of an operator \hat{X} :

$$\langle \hat{X} \rangle_\rho = \frac{\langle \mathcal{Q}^{(X,Z'_W)} \rangle_{\rho'_W}}{\langle \mathcal{Q}^{(Z,Z'_W)} \rangle_{\rho'_W}} = \frac{\langle \mathcal{Q}^{(X,Z_W)}(S_p) \text{sgn}(S_p) \rangle_{\rho'_W}}{\langle \mathcal{Q}^{(Z,Z_W)}(S_p) \text{sgn}(S_p) \rangle_{\rho'_W}}. \quad (4.29)$$

The Monte Carlo estimators \mathcal{Q} remain unchanged, apart from a multiplication with ± 1 depending on the relative sign of the two matrix determinants $\det A^\dagger(S_p)$ and $\det A^\dagger(S_p)$.

Implementation of the algorithm

Now that we have introduced the diagrammatic Monte Carlo formalism and showed how Monte Carlo estimators for physical observables can be obtained, we are ready to present the algorithm through which the sampling is realised. The configuration space is sampled via a Monte Carlo Markov chain process: in each step one of the possible updates from the current vertex configuration S_p to another vertex configuration S'_q is proposed with probability $W(S_p \rightarrow S'_q)$, and accepted with probability $P(S_p \rightarrow S'_q) = \min(1, \mathcal{R})$, given by the detailed balance equation,

$$\mathcal{R}W(S_p \rightarrow S'_q)\mathcal{D}^{(Z'_w)}(S_p) = W(S_p \leftarrow S'_q)\mathcal{D}^{(Z'_w)}(S'_q). \quad (5.1)$$

The requirements of detailed balance and ergodicity (from any initial configuration every other vertex configuration can be reached in a finite number of steps) ensure that the produced configurations are indeed distributed according to the correct thermal probability distribution $\rho'_W(S_p)$.

The diagrammatic expansion of the two-point correlation function (3.4) is similar to the expansion of the partition function Z , but contains an additional pair of two-point vertices at (\mathbf{x}, τ) and (\mathbf{x}', τ') . It is thus of advantage to sample these two series in the same simulation. In addition to sampling the regular four-point diagrams we allow updates that insert the pair of two-point vertices (which we will call “worm vertices”) into the configuration space. The vertex at (\mathbf{x}, τ) contains two incoming lines corresponding to spin up and spin down, and the vertex at (\mathbf{x}', τ') two outgoing lines corresponding to spin up and spin down. In matrix notation this means that if the worm vertices are present, the Green’s function matrices A^s each get an additional row and column, coming from contractions with P^\dagger and P respectively. We have already worked out the formalism for extending the configuration space in section 4.2. The original configuration space of four-point vertices will be denoted $\mathfrak{S}^{(Z)}$ and the configuration space containing the pair of two-point vertices $\mathfrak{S}^{(G)}$, such that $\mathfrak{S}^{(Z_w)} = \mathfrak{S}^{(Z)} \cup \mathfrak{S}^{(G)}$. The extended partition function Z_w takes the form

$$Z_w = Z \left(1 + \zeta \sum_{\mathbf{x}, \mathbf{x}'} \int_0^\beta d\tau \int_0^\beta d\tau' G_2(\mathbf{x}, \tau; \mathbf{x}', \tau') \right), \quad (5.2)$$

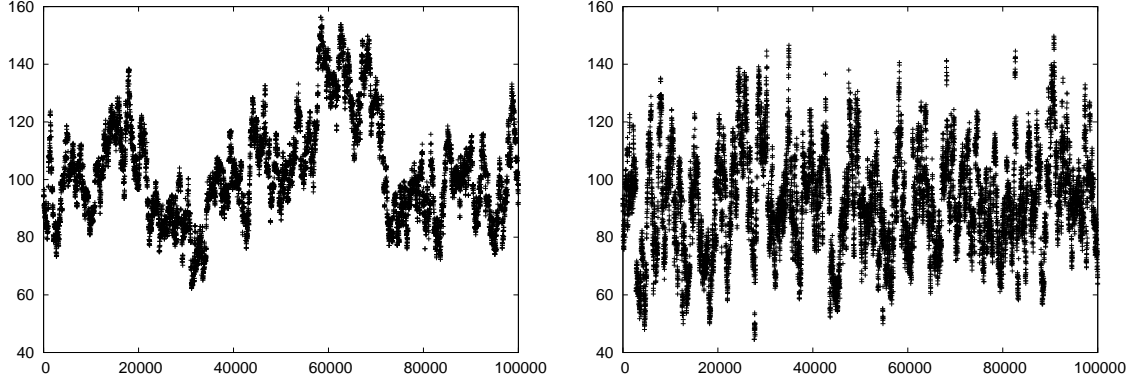


Figure 5.1: The first 100000 numerical measurements of the interaction energy (a measurement takes place every 100 Monte Carlo steps) with the worm setup (left) and the diagonal setup (right). Strong autocorrelations are visible in the worm setup.

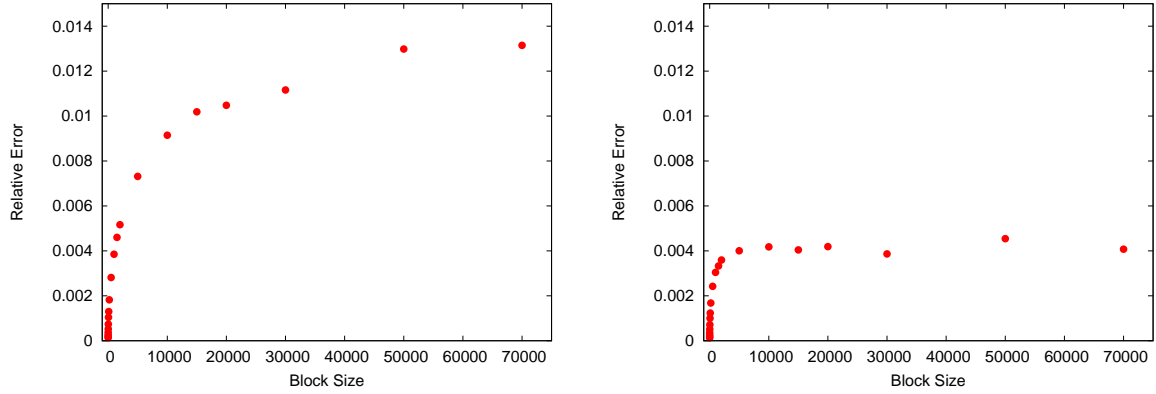


Figure 5.2: The blocking error analysis of the interaction energy with the worm setup (left) and the diagonal setup (right). The blocked error is much higher in the worm setup and continues increasing even for large block sizes.

where ζ is an arbitrary parameter. The advantage of this setup is that the Monte Carlo estimator for the order parameter $R(L, T)$ defined in equation (3.7) now becomes very simple: it is just a constant times the ratio of configurations with and without worm vertices,

$$\mathcal{Q}^{(R, Z_W)}(S_p) = \begin{cases} 0 & \text{for } S_p \in \mathfrak{S}^{(Z)} \\ L^{1+\eta}(\beta L^3)^{-2}\zeta^{-1} & \text{for } S_p \in \mathfrak{S}^{(G)} \end{cases} . \quad (5.3)$$

Other physical observables like the number density or the energy are still only measured when the system is in the “physical sector” $\mathfrak{S}^{(Z)}$, namely when the worm vertices are not present.

A detailed description of the original worm updates can be found in the appendix of [26]. The main idea behind the algorithm is that at low densities the major contribution to the partition function comes from multi-ladder diagrams – these are configurations where the vertices are arranged into several vertex chains. Proposing updates that favour the creation of such vertex chains will lead to higher acceptance ratios and

increase the efficiency of the simulation. At low densities the acceptance ratios of the worm updates are an order of magnitude higher than the acceptance ratios of the simple diagonal updates, in which the vertices are inserted or removed at random.

We found however, that the worm type addition and removal updates from the original setup [26] suffer from strong autocorrelations, so that even after many successful updates the configuration does not change significantly [5, 6]. The cause of this problem is that all updates are performed exclusively through the worm vertices. More precisely, a four-point vertex can only be added or removed from the configuration if its coordinates are in the vicinity of one of the worm vertices. This implies that over long times (until the position of the worm vertices changes significantly through another update) only a small proportion of the configuration space can be changed. Moreover the algorithm tends to repeatedly accept and then immediately undo a change in consecutive Monte Carlo steps.

To illustrate the extent of the problem we compare the measurements of the interaction energy (which is proportional to the diagram order) in the worm setup and the diagonal setup in Fig. 5.1. Both simulations used the same parameters and a comparable number of Monte Carlo steps. Figure 5.2 shows the blocking analysis of the relative error for the same quantity. Blocking is a widely used technique to estimate the error of an autocorrelated measurement. The single data points are arranged consecutively into blocks of equal size, and each block is replaced by the average of the measurements it contains. Then the error is calculated for the resulting blocked system in the usual way. If no autocorrelations are present, the error will be independent of the block size. In the presence of autocorrelations N consecutive data points fluctuate less than N independent measurements. Hence the error will increase with block size, until the block size reaches the autocorrelation length of the system.

Because of the large errors due to autocorrelations the worm setup is effectively less efficient than the standard diagonal setup. For this reason in the present study we employ the conventional diagonal updates, together with the modified worm addition and removal updates, as proposed in [5, 6]. This setup combines the advantages of the diagonal setup (weak autocorrelations) with the ones of the worm setup (high acceptance ratios). Below is a summary of all updates used in our simulation. For the modified updates we also give the values of the acceptance ratios \mathcal{R} (the other acceptance ratios can be found in [26], in the presence of an imbalance one merely needs to replace the terms $|\det A|^2$ by $|\det A^\dagger \det A|$).

Updates only concerning the worm vertices:

- **Worm creation/annihilation:** insert/remove the pair $P(\mathbf{x}, \tau)$, $P^\dagger(\mathbf{x}', \tau')$ into/from the configuration. In our setup the distributions for the coordinates of P and P^\dagger are independent: both are distributed uniformly over the lattice, so that

$W(S_p \rightarrow \tilde{S}_p) = (\beta L^3)^{-2}$, where \tilde{S}_p stands for the configuration S_p with the additional two-point vertices. The authors of [26] describe a setup in which the vertex P is selected randomly, and the vertex P^\dagger is then chosen in a spacetime hypercube of given extent around P . To avoid autocorrelations that can be associated with this scheme we employ the independent setup. The acceptance ratio is then

$$\mathcal{R} = \left| \frac{\det A^\dagger(\tilde{S}_p) \det A^\dagger(\tilde{S}_p)}{\det A^\dagger(S_p) \det A^\dagger(S_p)} \right| (\beta L^3)^2 \zeta. \quad (5.4)$$

- **Worm shift:** shift the $P^\dagger(\mathbf{x}', \tau')$ vertex to other coordinates. This update is equivalent to the worm shift update in [26] and involves a shift to a nearest neighbour on the lattice and a time shift in some interval around the old coordinates.

Updates of the regular four-point vertices: adding/removing a four-point vertex (changes the diagram order).

- **Diagonal version:** add or remove a random vertex. This is the most basic setup for changing the diagram order, however at low densities the acceptance ratios are very low.
- **Modified worm-type updates:**
 - Choose a random four-point vertex from the configuration (which will act as a worm for this step).
 - Addition: add another four-point vertex on the same lattice site and in some time interval of length $\Delta\tau$ around the worm.
 - Removal: remove the nearest neighbour of the worm vertex (implies that addition can only be accepted if the new vertex is the nearest neighbour of the worm).

The probability density for the addition update is then $W(S_p \rightarrow S_{p+1}) = 1/(p\Delta\tau)$, where $1/p$ comes from selecting the worm and $1/\Delta\tau$ from choosing the new time coordinate. Analogously for the removal update $W(S_p \leftarrow S_{p+1}) = 1/(p+1)$ and the acceptance ratio becomes

$$\mathcal{R} = \left| \frac{\det A^\dagger(S_{p+1}) \det A^\dagger(S_{p+1})}{\det A^\dagger(S_p) \det A^\dagger(S_p)} \right| \frac{(-U)p\Delta\tau}{p+1}. \quad (5.5)$$

The modified worm setup still prolongs existing vertex chains like the original worm setup, but autocorrelations are significantly reduced since the “worm” changes with every update. This new type of updates can only be employed in addition to the regular diagonal addition and removal updates. It works regardless if the pair of two-point

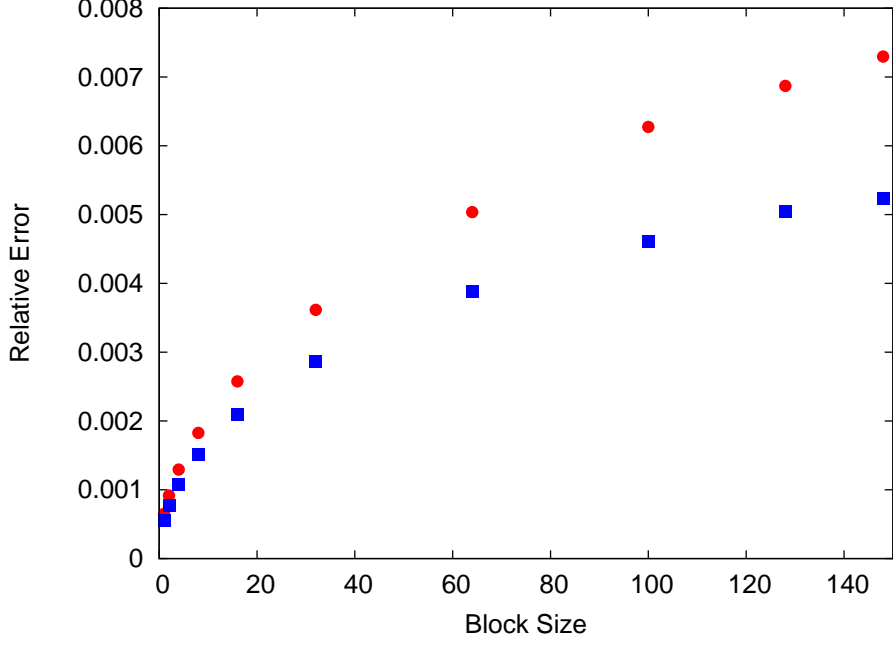


Figure 5.3: The blocking error analysis of the interaction energy. Red circles correspond to the pure diagonal setup and blue squares to a combination of diagonal and modified worm updates with equal probabilities for each kind of update.

vertices is present or not in the configuration (the original worm addition and removal updates can only take place when the two-point vertices are present). The acceptance rates for this update are comparable with those for the regular worm updates. To demonstrate the increase in efficiency we compare the diagonal and the modified worm setup at low density, when the acceptance rates of the diagonal updates are particularly poor. We again consider the blocking analysis of the relative error for the interaction energy. As Fig. 5.3 clearly shows, the autocorrelation length does not increase in presence of the modified worm updates. The blocked error in this case is significantly lower due to the increased acceptance rate.

The structure of the updates requires the calculation of a matrix determinant of a large matrix (with rank p up to about 6000) in each Monte Carlo step. Since only a few elements of the matrix change in the course of one update (at most one row and one column) a recalculation of the whole determinant from scratch is not necessary. In our implementation we make use of the fast matrix update formulae [50] which decrease the number of required operations to order p^2 instead of order p^3 . A detailed description of the matrix update procedures with all necessary mathematical proofs is given in the appendix A. In the presence of an imbalance we need to keep in memory two large matrices instead of one and update each of these matrices separately. Another drawback is that the relative error of the sign adds to the relative error of each observable.

Numerical errors can become very large if the expectation value of the sign in the denominator of a generic thermal expectation value (4.29) is close to zero, as it happens

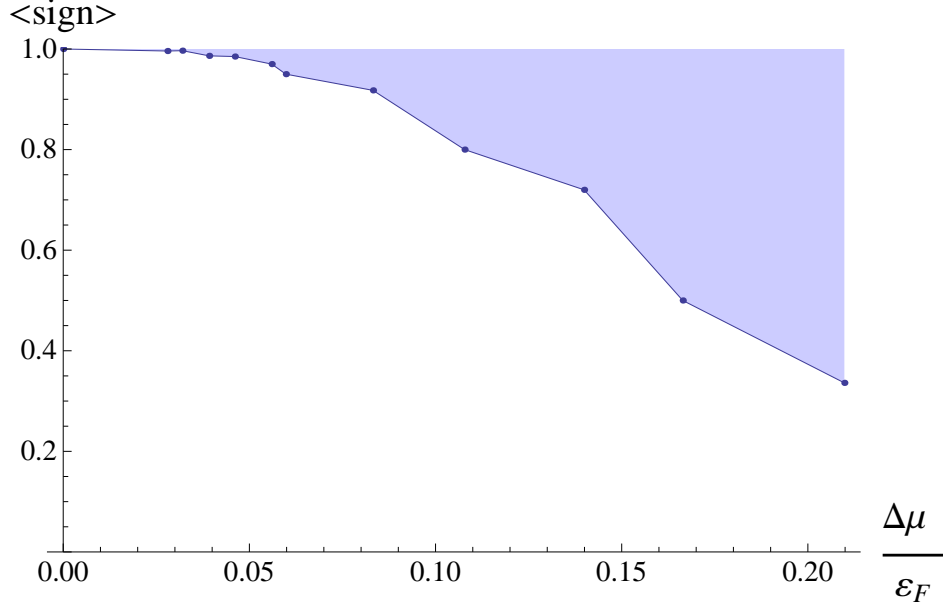


Figure 5.4: Schematic plot of the average sign near the critical point as a function of imbalance. The shaded area covers the range of values the sign can take at different values of lattice size and chemical potential. The lower boundary of this area is the “worst-case” curve of the sign, corresponding to the largest lattice sizes used.

for the expectation value of the phase in QCD. For the unitary Fermi gas the sign remains very close to unity for small imbalances, as shown in Fig. 5.4, so that sign quenching is applicable for imbalances up to approximately $0.2\varepsilon_F$. The restricting factor that keeps us from reaching large imbalances is not the sign, but rather the fact that even large values of the lattice chemical potential difference $\Delta\mu$ do not necessarily lead to large differences in the filling factors of the two components and hence the physical value $\Delta\mu/\varepsilon_F$ still remains small. This method works best close to the balanced limit and can provide a useful tool to examine the trend of the critical temperature and other observables for small deviations from it.

Observables at the critical point

The results presented in this chapter were published in [6, 7].

With the DDMC algorithm described in the previous chapters we obtained data at 25 different values $(\mu_\uparrow, \mu_\downarrow)$, of which 8 were at $\mu_\uparrow = \mu_\downarrow$. The lattice sizes varied between 4^3 for the highest filling factor and 26^3 for the lowest, so that the volume range in physical units was approximately constant. As discussed in chapter 2, the dimensionless physical observables scale linearly with $\nu^{1/3}$ if we are close enough to the continuum limit, such that higher order lattice corrections can be neglected. With our data this behaviour is seen for $\nu^{1/3} \gtrsim 0.75$. This condition was fulfilled for 23 out of the 25 points and in particular for 7 out of the 8 balanced points.

The two most common ways of quantifying imbalance are either through the chemical potential difference $\Delta\mu/\varepsilon_F = |\mu_\uparrow - \mu_\downarrow|/\varepsilon_F$, or through the relative density difference $\Delta\nu/\nu = |\nu_\uparrow - \nu_\downarrow|/(\nu_\uparrow + \nu_\downarrow)$. For the values of imbalance considered in our study these two quantities are proportional to each other, with $\Delta\nu/\nu = 0.122(2)\Delta\mu/\varepsilon_F$, as illustrated in Fig. 6.1. The relative density difference shows no dependence on lattice size (the L -dependencies of ν and $\Delta\nu$ cancel each other out), but considerable dependence on the temperature. Also since $\Delta\nu$ is a very small quantity, numerical fluctuations can become significant. Since the chemical potential difference is less prone to numerical errors, we will use it from now on to quantify imbalance.

Every observable X is a function of filling factor ν and imbalance $h = \Delta\mu/\varepsilon_F$. We are ultimately interested in the continuum limit $\nu = 0$ and want to perform the corresponding extrapolation. To achieve this all numerical data is fitted to a three dimensional surface, where the following assumptions are made for the form of the fitted function:

- At fixed imbalance, X is a linear function of $\nu^{1/3}$ with slope $\alpha^{(X)}(h)$: $X(\nu, h) = X(h) + \alpha^{(X)}(h)\nu^{1/3}$.
- $X(h)$ and $\alpha^{(X)}(h)$ viewed as functions of the imbalance h are analytic and can thus be Taylor expanded.
- Due to symmetry in h all odd powers in the Taylor expansions of $X(h)$ and $\alpha^{(X)}(h)$ have to vanish.

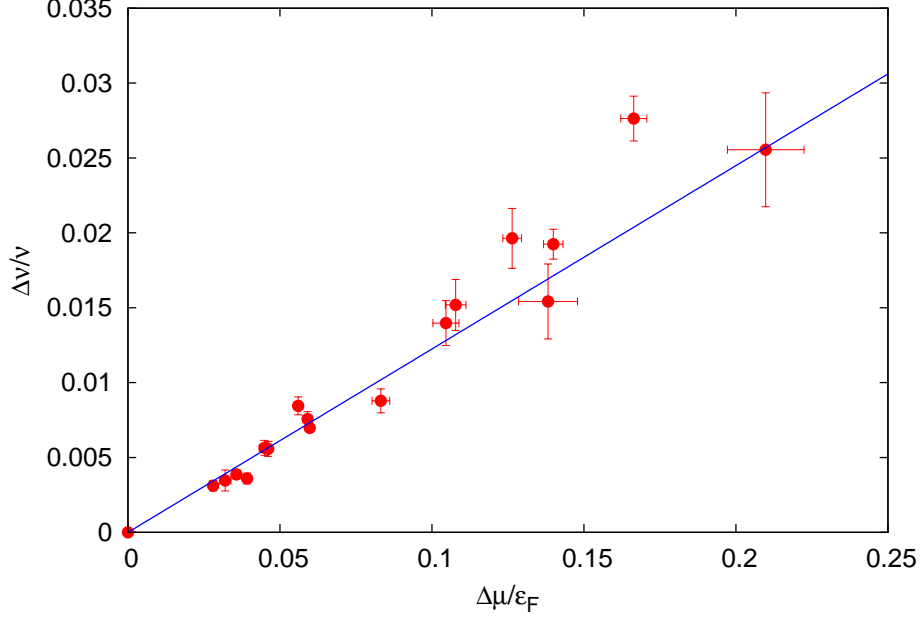


Figure 6.1: Relation between the chemical potential difference and the relative density difference at T_c .

If for instance we expand $X(h)$ and $\alpha^{(X)}(h)$ to leading order in h the fitted function becomes

$$X(\nu, h) = X_0 + X_2 h^2 + (\alpha_0^{(X)} + \alpha_2^{(X)} h^2) \nu^{1/3}. \quad (6.1)$$

This requires a linear fit of four parameters.

6.1 Spin susceptibility and pseudogap

From the fit shown in Fig. 6.1 we can extract the spin susceptibility of the gas [56]. The dimensionless spin susceptibility $\tilde{\chi}$ (in units of the spin susceptibility of an ideal Fermi gas) can be obtained from the relative density difference via

$$\frac{\Delta\nu}{\nu} = \frac{3}{2} \tilde{\chi} \frac{\Delta\mu}{2\varepsilon_F}. \quad (6.2)$$

From our data we obtain the value $\tilde{\chi} = 0.163(3)$ at the critical point. This value is lower than the zero-temperature result $\tilde{\chi}(T = 0) \approx 0.54$ extracted from the experimental data in [56].

Experimentally the spin imbalance $\Delta\nu/\nu$ is increased by applying an external magnetic field $h = \Delta\mu/\varepsilon_F$. At zero temperature the system does not react immediately towards a change in h , resulting in a gap Δ . The gap can be understood as half of the energy needed to break one fermionic pair in order to polarise the system by one excess particle [3]. The size of the gap can be extracted from the density of states which is zero

in the interval $[\mu - \Delta, \mu + \Delta]$. At finite temperature the density of states can exhibit a dip which is similar to the gap and is referred to as the pseudogap Δ^* (see e.g. [57] for a review). The existence of the pseudogap can also be verified by looking at the spin susceptibility of the system. In a degenerate ideal gas which is described by the Fermi-Dirac distribution, the susceptibility equals the density of states at the Fermi level [3]. In this simple model, since for small imbalances the Fermi levels of the two spin states will lie within the dip, the spin susceptibility will be lower than for large imbalances, when the Fermi levels of the two spin states are both outside the dip. As a consequence $\Delta\nu/\nu$ as a function of h will be a curve with two asymptotes: as the imbalance goes to zero the asymptote has zero intercept and a small slope, while in the limit of large imbalance the asymptote has a greater slope and the intercept is unequal zero. Our data suggests an intercept which is either zero or very small. For a fit where both the slope and the intercept are free parameters we obtain $\Delta\nu/\nu = 0.149(6)h - 0.0016(3)$. From this we can conclude that if the pseudogap exists for the unitary Fermi gas at T_c it must be either very broad ($\Delta^* \gtrsim 0.2\varepsilon_F$, the maximal imbalance considered in this work) or the dip in the density of states is very small, such that it cannot be resolved within the precision of our data.

6.2 Critical temperature

Before we include the imbalanced data we first present our analysis of the data at zero imbalance, for comparison with previous results from [26]. Our results and the continuum extrapolation are shown in Fig. 6.2. A line was fitted through the seven points with $\nu^{1/3} < 0.75$, resulting in $T_c/\varepsilon_F = 0.173(6) - 0.16(1)\nu^{1/3}$. The goodness of fit is $\chi^2/\text{d.o.f.} = 0.39$. For comparison we also fit a quadratic through all eight data points, resulting in a continuum value of $T_c/\varepsilon_F = 0.188(15)$, which is in excellent agreement with the linear extrapolation. This confirms that sub-leading corrections proportional to $\nu^{2/3}$ can indeed be neglected for sufficiently small ν .

In Fig. 6.3 we show the results for the fit parameters c , f_0 and $f_1 T_c$, according to Eq. (3.9). These parameters are smooth functions of the filling factor. In particular this data confirms that the non-universal constant c does indeed take values of order unity (cf. section 3) and thus cannot be neglected.

Now we also include data with $\mu_\uparrow \neq \mu_\downarrow$. The best fit of the critical temperature in units of ε_F to the function

$$T_c(\nu, h) = T_0 + T_2 h^2 + (\alpha_0^{(T)} + \alpha_2^{(T)} h^2) \nu^{1/3}, \quad (6.3)$$

yields $T_0 = 0.171(5)$, $\alpha_0^{(T)} = -0.154(9)$, $T_2 = 0.4 \pm 0.9$ and $\alpha_2^{(T)} = -0.7 \pm 1.9$ with $\chi^2/\text{d.o.f.} = 0.43$. Note that the T_2 value corresponding to the minimal χ^2 is positive, which is forbidden by physical arguments (T_c can only decrease with growing imbalance,

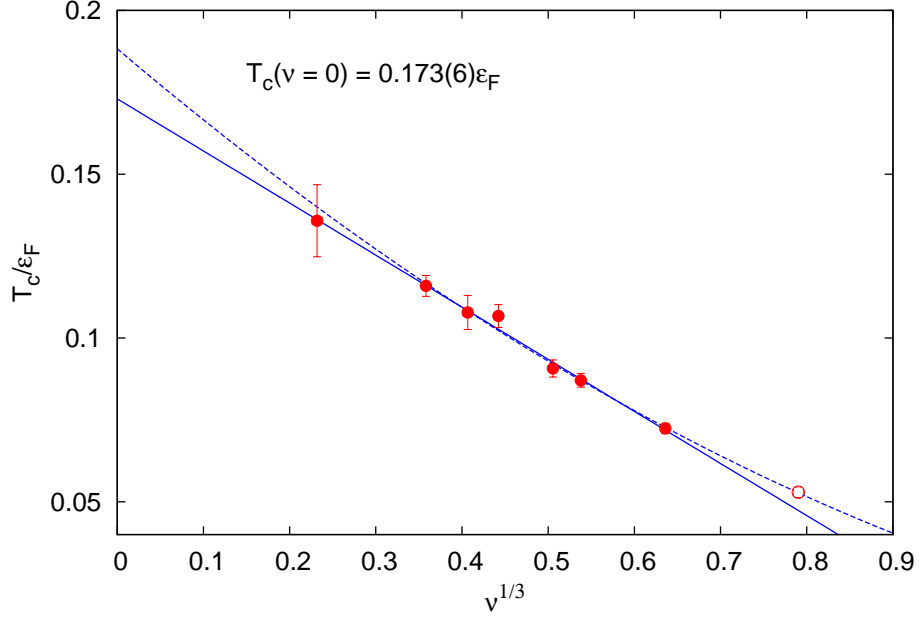


Figure 6.2: The critical temperature versus filling factor for different values of the chemical potential. The continuum limit corresponds to $\nu \rightarrow 0$. The linear extrapolation (solid line) of the seven data points at lowest filling factors (filled circles) yields a continuum value of $T_c/\varepsilon_F = 0.173(6)$. The dashed line corresponds to a quadratic fit through all data points.

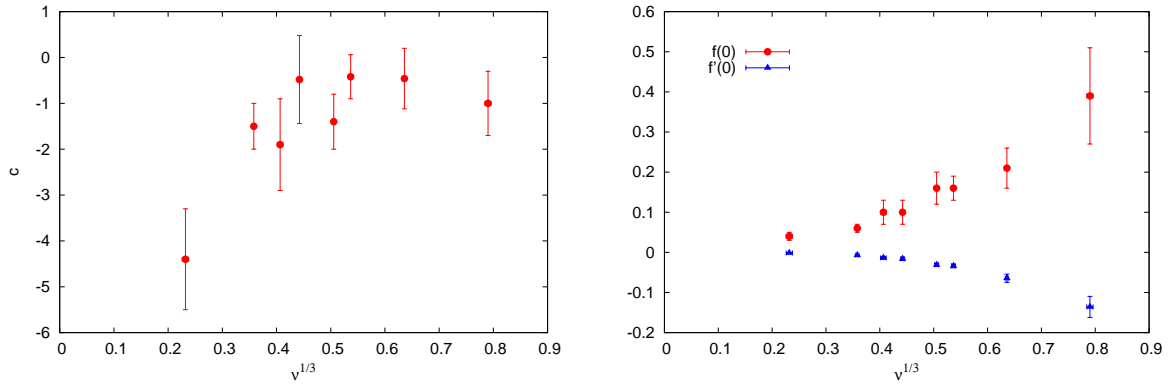


Figure 6.3: The non-universal constant c (left) and the first two coefficients in the expansion of the universal scaling function $f(x)$ (right) in lattice units versus filling factor, see Eq. (3.9) with $f(0) = f_0$ and $f'(0) = f_1 T_c$.

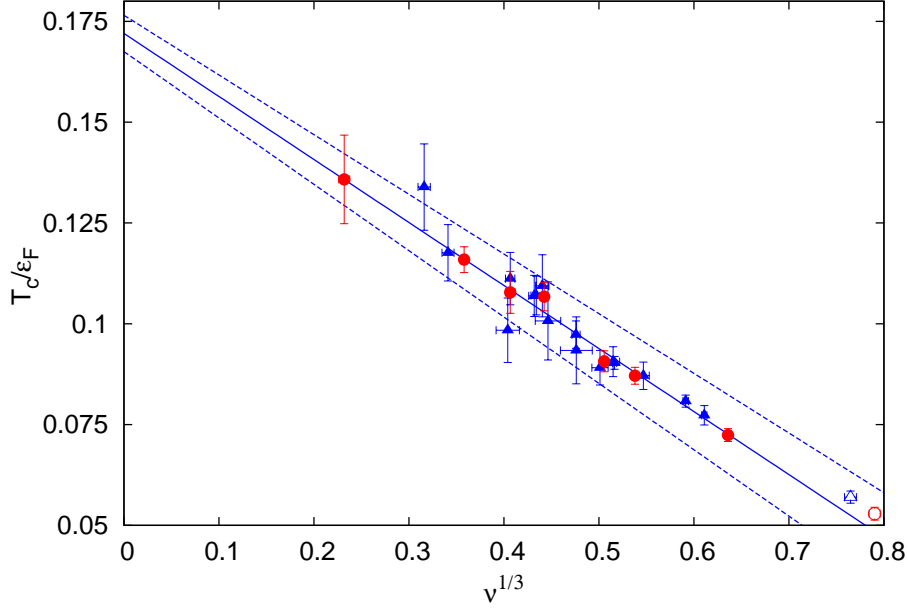


Figure 6.4: Projection of the data onto the $(\nu^{1/3}-T_c)$ plane. Red circles denote the balanced data and blue triangles data at non-zero imbalance. The line corresponds to the constant fit (6.7). Dashed lines denote the error margins.

as interactions are suppressed). The χ^2 -function is very flat along the T_2 direction, so that forcing $T_2 = 0$ results in $\chi^2/\text{d.o.f.} = 0.44$. From the error on T_2 we derive the lower bound $T_2 > -0.5$. The best fit values for T_0 and $\alpha_0^{(T)}$ are in excellent agreement with the ones obtained from the fit of the balanced data only.

The error on the best fit value for α_2 is very large and the fit is consistent with $\alpha_2^{(T)} = 0$. Hence we also perform a fit to the function

$$T_c(\nu, h) = T_0 + T_2 h^2 + \alpha_0^{(T)} \nu^{1/3}, \quad (6.4)$$

where $T_c(h)$ has again been expanded to quadratic order and the function $\alpha^{(T)}(h)$ has been replaced by a constant $\alpha_0^{(T)}$. The best fit is

$$T_c(\nu, h) = 0.171(5) + 0.07(11)h^2 - 0.155(8)\nu^{1/3}, \quad (6.5)$$

with $\chi^2/\text{d.o.f.} = 0.41$. This χ^2 -value is even lower than for the previous fit, which means that the data justifies dropping the $\alpha_2^{(T)}$ term. The best fit result is still consistent with $T_2 = 0$ and leads to a much tighter lower bound $T_2 > -0.04$. The other parameters T_0 and $\alpha_0^{(T)}$ agree with the results from the previous fit and the fit of the balanced data.

Since our results indicate that T_c remains almost unchanged in response to a weak

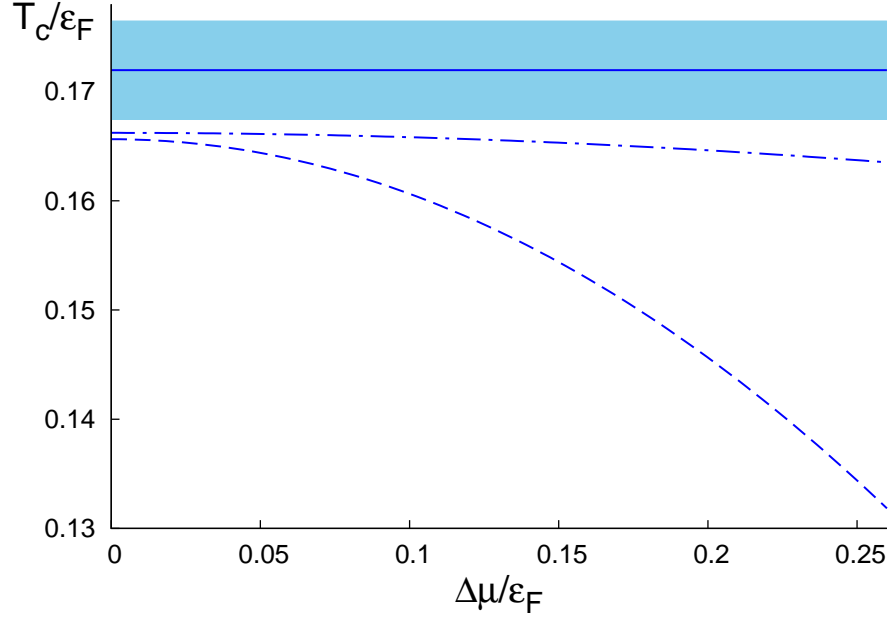


Figure 6.5: The continuum limit of the critical temperature as a function of imbalance. The solid line is the value obtained from the constant fit (6.6), the shaded area corresponds to one standard deviation. The dashed line is the lower bound obtained from fit (6.3) and the dot-dashed line is the tighter lower bound obtained from fit (6.4).

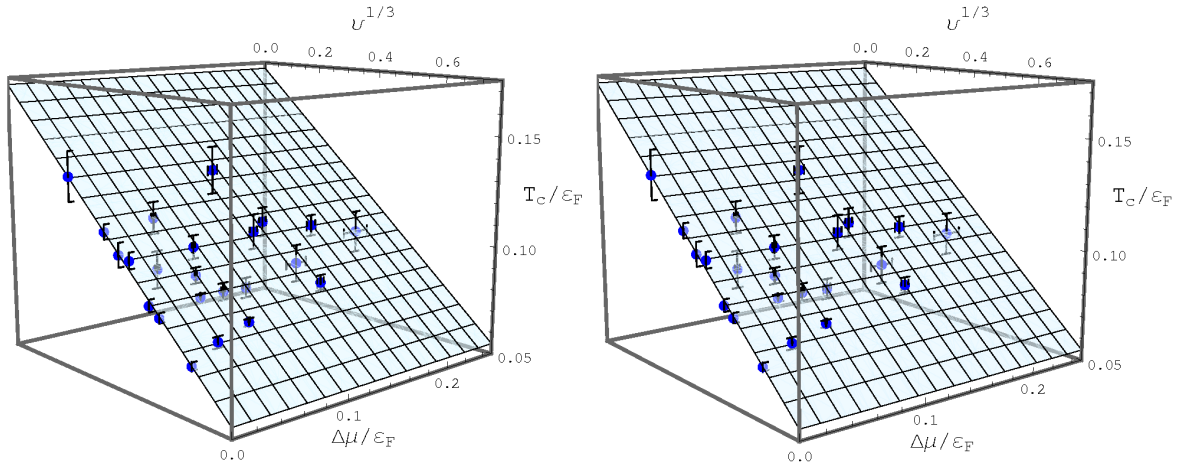


Figure 6.6: Stereogram of the critical temperature versus filling factor and imbalance. The surface corresponds to the constant fit (6.7). To view the image focus your eyes on a point between the image and you (cross viewing).

	T_0	δT_0	T_2	T_2 lower bound	$\alpha_0^{(T)}$	$\delta\alpha_0^{(T)}$	$\alpha_2^{(T)}$	$\delta\alpha_2^{(T)}$	$\chi^2/\text{d.o.f.}$
balanced data	0.173	0.006			-0.16	0.01			0.39
fit to Eq. (6.3)	0.171	0.005	0.4	-0.5	-0.154	0.009	-0.7	1.9	0.43
fit to Eq. (6.4)	0.171	0.005	0.07	-0.04	-0.155	0.008			0.41
fit to Eq. (6.6)	0.172	0.0045			-0.156	0.008			0.41

Table 6.1: Comparison of fit parameters obtained by different fit methods.

imbalance, we also perform a fit to constant $T_c(h)$ and $\alpha^{(T)}(h)$,

$$T_c(\nu, h) = T_0 + \alpha_0^{(T)} \nu^{1/3}. \quad (6.6)$$

This is the same function as the one used in the balanced case and corresponds to a straight line fitted through the projection of all data points onto the $(\nu^{1/3}-T_c)$ plane, see Fig. 6.4. The best fit is

$$T_c(\nu, h) = 0.1720(45) - 0.156(8)\nu^{1/3}, \quad (6.7)$$

with $\chi^2/\text{d.o.f.} = 0.41$. Again the result agrees with the previous fits.

We also performed fits using the jackknife method and several robust fits. All results were consistent with the minimal χ^2 fits. Table 6.1 provides an overview of the results obtained with the different fit methods. The values for the parameters T_0 and $\alpha_0^{(T)}$ were obtained with high accuracy and are all in excellent agreement with each other, independently of the form of the fit function. Depending on the model assumptions two lower bounds could be derived for the leading order deviation of the critical temperature from its balanced value. Figure 6.5 shows these two bounds compared with the value in the balanced case. A three dimensional stereoscopic plot of the data together with a constant surface fit is presented in Fig. 6.6.

6.3 Energy per particle

The total energy is composed of the kinetic energy E_{kin} and the interaction energy E_{int} . An explicit expression for the former can be obtained from the coordinate space picture,

$$E_{\text{kin}} = - \left\langle \sum_{\mathbf{x}, s} c_{\mathbf{x}s}^\dagger \nabla^2 c_{\mathbf{x}s} \right\rangle \quad (6.8)$$

$$= - \left\langle \sum_{\mathbf{x}, s} c_{\mathbf{x}s}^\dagger \sum_{j=1}^3 (c_{(\mathbf{x}+\mathbf{j})s} + c_{(\mathbf{x}-\mathbf{j})s} - 2c_{\mathbf{x}s}) \right\rangle \quad (6.9)$$

$$= \sum_s \langle L^3 (6c_{\mathbf{x}s}^\dagger c_{\mathbf{x}s} - 6c_{\mathbf{x}s}^\dagger c_{(\mathbf{x}+\mathbf{j})s}) \rangle, \text{ for any } \mathbf{j}, \mathbf{x}. \quad (6.10)$$

The factor L^3 in the last step comes from summation over all lattice sites and the factors of 6 are due to summation over j . Since $\sum_s \langle c_{\mathbf{x}s}^\dagger c_{\mathbf{x}s} \rangle$ corresponds to the filling factor, the kinetic energy per particle can be written as

$$E_{\text{kin}}/L^3\nu = 6 \left(1 - \frac{\sum_s \langle c_{\mathbf{x}s}^\dagger c_{(\mathbf{x}+\mathbf{j})s} \rangle}{\nu} \right). \quad (6.11)$$

The Monte Carlo estimator for the interaction energy $E_{\text{int}} = \langle H_1 \rangle$ can be obtained with the Hellmann-Feynman theorem [26]. Define $H(\lambda) = H_0 + \lambda H_1$ and observe that

$$\text{Tr} H_1 e^{-\beta H} = - \frac{1}{\beta} \frac{\partial}{\partial \lambda} \text{Tr} e^{-\beta H(\lambda)} \Big|_{\lambda=1} \equiv - \frac{1}{\beta} \frac{\partial Z(\lambda)}{\partial \lambda} \Big|_{\lambda=1}. \quad (6.12)$$

The modified function $Z(\lambda)$ differs from the partition function only by a rescaling of the coupling constant $U \rightarrow \lambda U$. From equation (2.39) it follows immediately that a diagram of order p is proportional to λ^p and hence differentiating and then setting $\lambda = 1$ generates a factor of p . Hence the Monte Carlo estimator for the interaction energy is given by $\mathcal{Q}^{(H_1, Z)}(S_p) = -\beta^{-1}p$.

The energy per particle thus depends on three observables, the kinetic correlator $\sum_s \langle c_{\mathbf{x}s}^\dagger c_{(\mathbf{x}+\mathbf{j})s} \rangle$, the filling factor $\sum_s \langle c_{\mathbf{x}s}^\dagger c_{\mathbf{x}s} \rangle$ and the average diagram order. Naturally, these observables are strongly correlated with each other. Calculating their expectation values and errors separately and then using error propagation would lead to a tremendous overestimation of the total error. We therefore apply a different strategy. We group the data into N blocks of consecutive data points, with block size well above the autocorrelation size. For each block we then calculate the average of each of the three observables and then from these averages the value of the total energy per particle in units of the Fermi energy. This leaves us with a set of N independent values for the energy per particle. We then calculate the total average, which will be our best estimate for the energy per particle and obtain the error on this estimate with the jackknife method, see e.g. [58], as follows. We remove one block at a time from the total sample and calculate the averages of the N reduced samples with $N - 1$ points each. The variance of this sample of reduced averages yields an error estimate on the total error of the energy per particle.

Our results using only balanced data are shown in Fig. 6.7. These results were obtained at T_c , but the temperature dependence of the energy per particle near T_c was found to be very weak. Also this quantity showed no dependence on the lattice size L and hence the final results are averages over all values of L used. For the energy per particle we obtain the continuum value $E/N\varepsilon_F = 0.276(14)$. In units of the ground state energy of the free gas, $E_{\text{FG}} = (3/5)N\varepsilon_F$, our result is $E/E_{\text{FG}} = 0.46(2)$. Since the expression for the kinetic energy (6.11) involves a difference of two quantities of comparable size, large fluctuations can occur, especially at low filling factors. For this

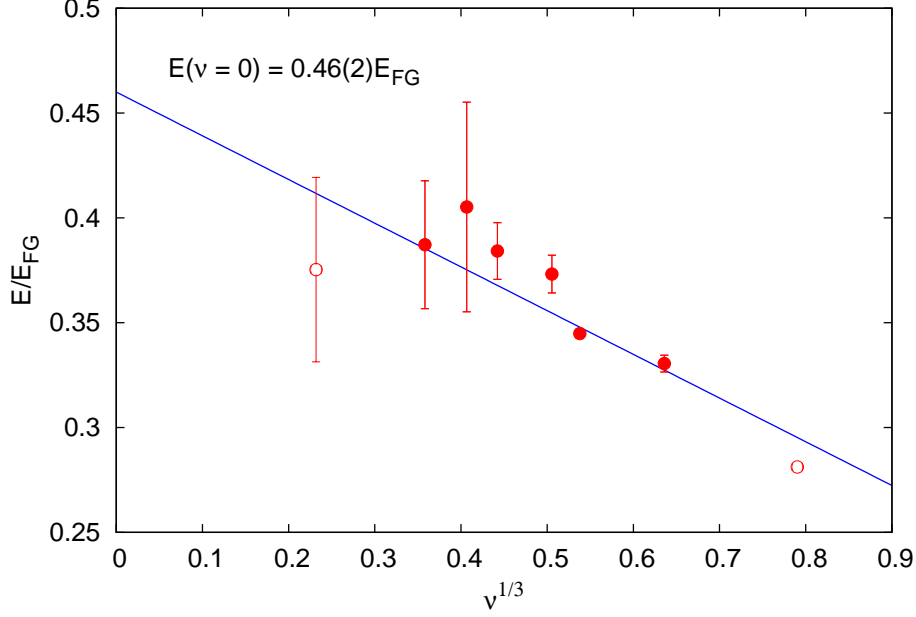


Figure 6.7: The energy per particle versus filling factor at the critical point. The linear fit was performed for data at filling factors $\nu^{1/3} < 0.75$. Filled circles indicate data included in the fit and empty circles stand for data excluded from the fit, see text for discussion.

reason measurements of the energy per particle at lowest filling factor could only be performed on lattices with size $L \leq 14$, which is smaller than the lattice sizes used for the measurement of the critical temperature. We include this point in the plot in Fig. 6.7, but exclude it from the linear fit. The goodness of fit is $\chi^2/\text{d.o.f.} = 2.1$.

Since with increasing imbalance interactions become suppressed, we expect the absolute value of the interaction energy to decrease. This in turn means an increase of the total energy, since the interaction energy is negative. As we did for the critical temperature we fit the energy in units of E_{FG} to the function

$$E(\nu, h) = E_0 + E_2 h^2 + (\alpha_0^{(E)} + \alpha_2^{(E)} h^2) \nu^{1/3} \quad (6.13)$$

and obtain the best fit parameters $E_0 = 0.440(15)$, $\alpha_0^{(E)} = -0.17(3)$, $E_2 = 3.4 \pm 2.2$ and $\alpha_2^{(E)} = -3.1 \pm 4.5$, with $\chi^2/\text{d.o.f.} = 2.8$. These results are consistent with the balanced fit. The leading coefficient $E_2 = 3.4 \pm 2.2$ is no longer consistent with zero. We also perform a fit to the function

$$E(\nu, h) = E_0 + E_2 h^2 + \alpha_0^{(E)} \nu^{1/3} \quad (6.14)$$

and obtain the best fit result

$$E(\nu, h) = 0.444(13) + 1.9(3)h^2 - 0.18(2)\nu^{1/3}, \quad (6.15)$$

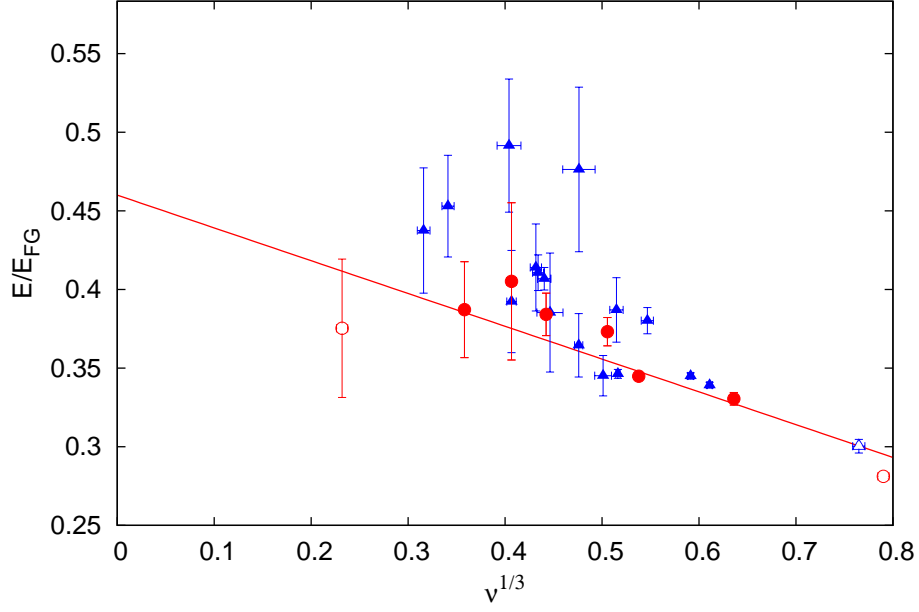


Figure 6.8: Projection of the data for the energy per particle onto the $(\nu^{1/3}-E)$ plane. Red circles denote the balanced data and blue triangles data at non-zero imbalance. For comparison the fit at zero imbalance is shown. The points at non-zero imbalance tend to lie above the balanced fit line.

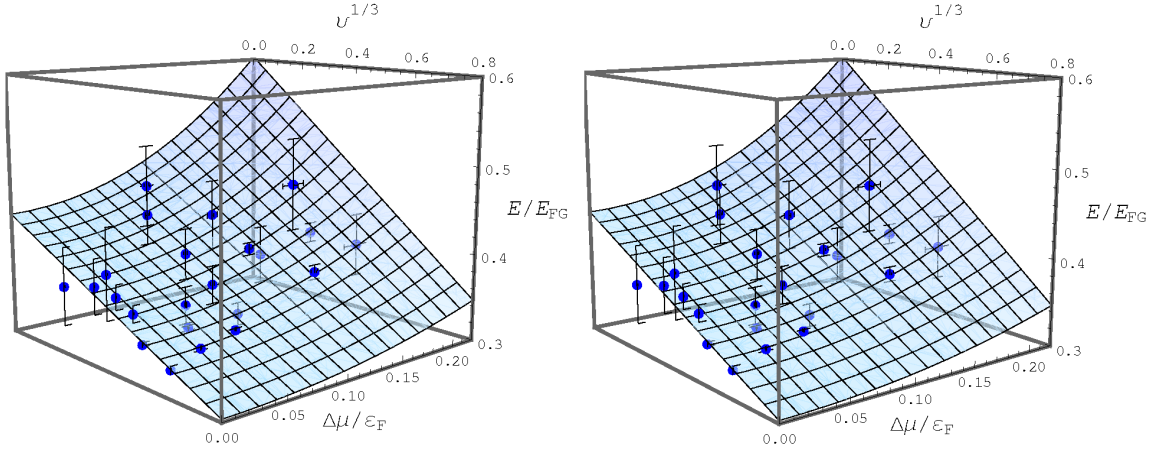


Figure 6.9: Stereogram of the energy per particle E/E_{FG} versus filling factor and imbalance. The surface fit corresponds to the quadratic fit (6.13). To view the image focus your eyes on a point between the image and you (cross viewing).

which agrees with the previous result. The $\chi^2/\text{d.o.f.} = 2.7$. The figures 6.8 and 6.9 show the numerical data.

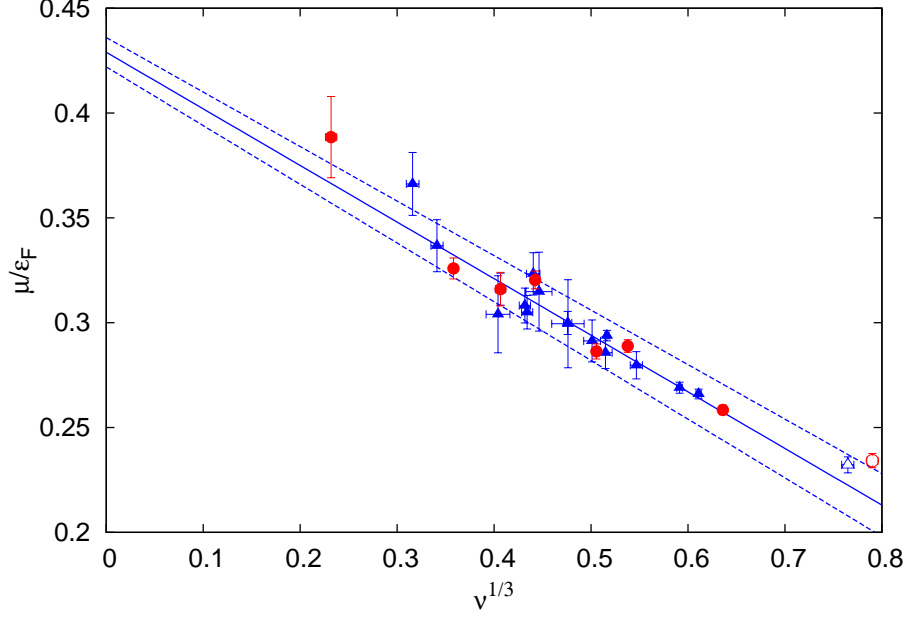


Figure 6.10: Projection of the data for the average chemical potential onto the $(\nu^{1/3}-\mu)$ plane. Red circles denote the balanced data and blue triangles data at non-zero imbalance. The solid line corresponds to the constant fit and the dashed lines indicate the error margins.

6.4 Chemical potential

For the chemical potential at T_c we obtain the continuum value $\mu/\varepsilon_F = 0.429(9)$ with $\chi^2/\text{d.o.f.} = 2.8$ using only balanced data. A similar analysis can be performed for the average chemical potential $\mu/\varepsilon_F = |\mu_\uparrow + \mu_\downarrow|/2\varepsilon_F$ in the presence of an imbalance. Since the average chemical potential is not expected to depend on the imbalance we fit our data in units of ε_F to the constant function

$$\mu(\nu, h) = \mu_0 + \alpha_0^{(\mu)} \nu^{1/3} \quad (6.16)$$

and obtain

$$\mu(\nu, h) = 0.429(7) - 0.27(1)\nu^{1/3}, \quad (6.17)$$

with $\chi^2/\text{d.o.f.} = 1.1$. This is in very good agreement with our balanced result. A plot of the data and the fit is in Fig. 6.10.

6.5 Contact density

Another important quantity is the contact, which plays a prominent role in several universal relations derived by Tan [59, 60, 61]. Through these relations the contact can be interpreted in different ways, for instance as a measure of the local pair density [62], or

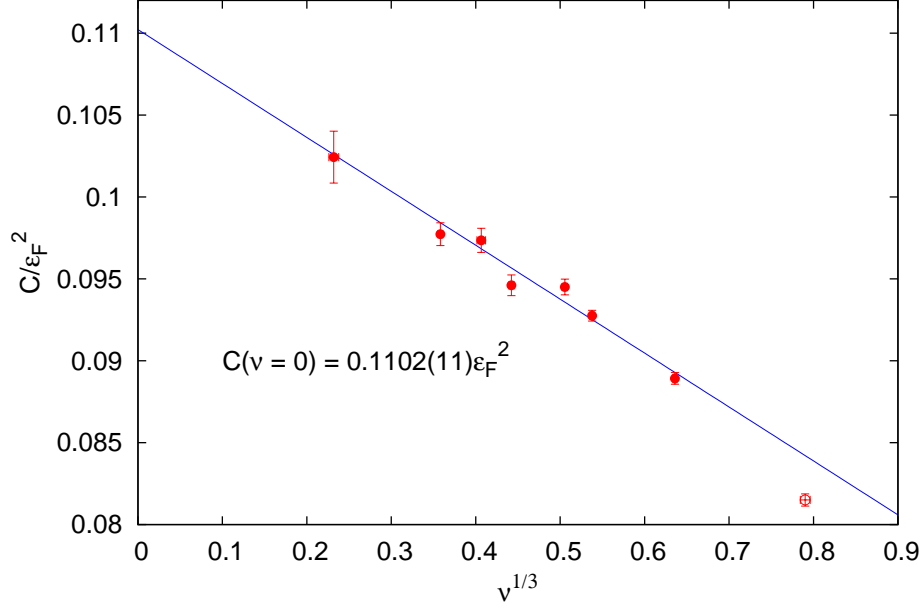


Figure 6.11: The contact density versus $\nu^{1/3}$ for the balanced data at the critical point. The linear fit was performed for data at filling factors $\nu^{1/3} < 0.75$ (filled circles).

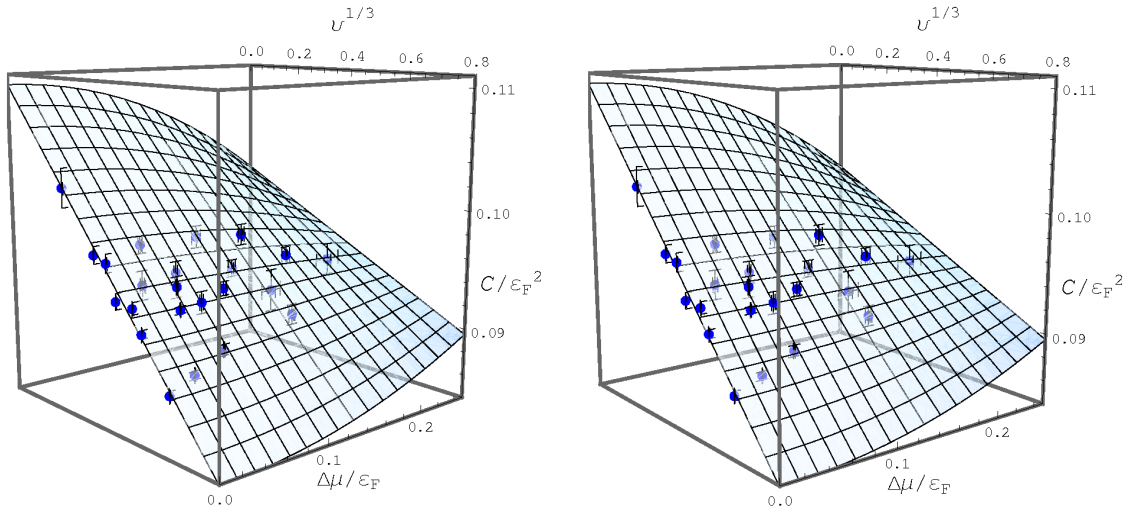


Figure 6.12: Stereogram of the contact density C/ε_F^2 versus filling factor and imbalance. The surface corresponds to the quadratic fit (6.21). To view the image focus your eyes on a point between the image and you (cross viewing).

a measure of the number of atoms with large momenta. The contact also features in the expression for the total energy and in particular is responsible for making this expression convergent, as the contact term cancels the divergent momentum distribution tail. The adiabatic relation describes how the total energy changes with scattering length in terms of the contact. In the presence of an external potential the contact appears in the virial theorem and for a homogeneous system in the relation between pressure and energy. We choose

$$C = m^2 g_0 E_{\text{int}} \quad (6.18)$$

as the definition of the contact, where g_0 denotes the physical coupling constant [62, 63]. The contact is related to the contact density \mathcal{C} via

$$C = \int \mathcal{C}(\mathbf{r}) d^3 r, \quad (6.19)$$

or for homogeneous systems simply $C = \mathcal{C}V$. The dimensionless quantity $\mathcal{C}/\varepsilon_F^2$ can be expressed through lattice quantities¹ as

$$\mathcal{C}/\varepsilon_F^2 = (UE_{\text{int}})/(4L^3\varepsilon_F^2). \quad (6.20)$$

Using only balanced data the best fit is $\mathcal{C}/\varepsilon_F^2 = 0.1102(11) - 0.033(2)\nu^{1/3}$ with $\chi^2/\text{d.o.f.} = 1.8$. The data and the fit are shown in Fig. 6.11. In the presence of an imbalance we expect the interaction energy and hence the contact density to decrease. A three dimensional fit of the data for $\mathcal{C}/\varepsilon_F^2$ to

$$C(\nu, h) = C_0 + C_2 h^2 + (\alpha_0^{(C)} + \alpha_2^{(C)} h^2) \nu^{1/3} \quad (6.21)$$

yields $C_0 = 0.1101(9)$, $\alpha_0^{(C)} = -0.033(2)$, $C_2 = -0.15(16)$ and $\alpha_2^{(C)} = -0.29(36)$, with $\chi^2/\text{d.o.f.} = 1.5$. This is consistent with the balanced fit. The best fit value for the parameter C_2 is negative as required. Forcing $\alpha_2^{(C)} = 0$,

$$C(\nu, h) = C_0 + C_2 h^2 + \alpha_0^{(C)} \nu^{1/3}, \quad (6.22)$$

yields $C_0 = 0.1099(8)$, $\alpha_0^{(C)} = -0.0322(15)$ and $C_2 = -0.01(2)$, with $\chi^2/\text{d.o.f.} = 1.5$. Fitting to a constant function yields $C(\nu, h) = 0.1097(8) - 0.0320(14)\nu^{1/3}$ with $\chi^2/\text{d.o.f.} = 1.4$. Figure 6.12 summarises our results. By a simple change of variables we can obtain the contact in units of Nk_F from the contact density. Our most precise value for the contact at zero imbalance (corresponding to $\mathcal{C}/\varepsilon_F^2 = 0.1101(9)$ from fit (6.21)) is $C/Nk_F = 3.26(3)$.

¹remember that we use $m = 1/2$ and hence in particular $\varepsilon_F = k_F^2$

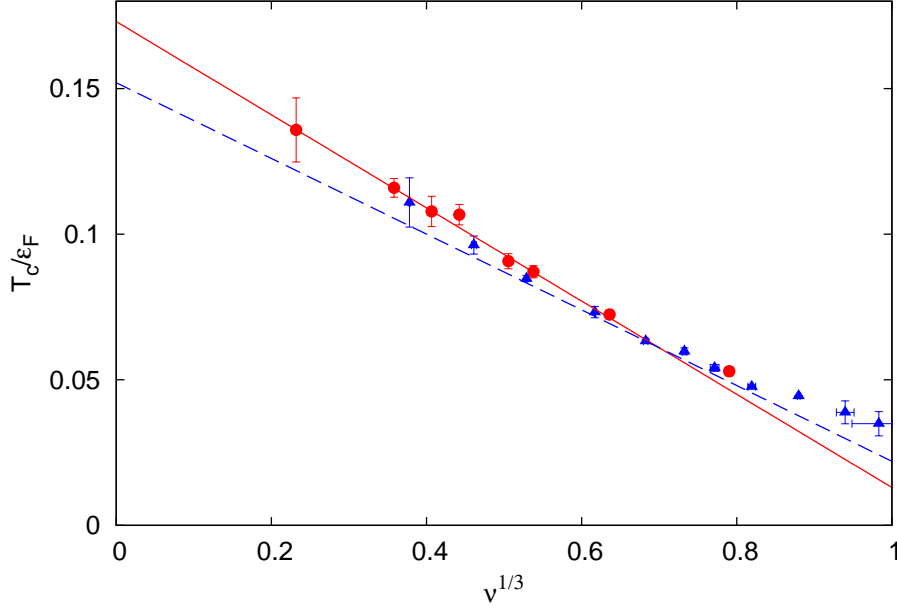


Figure 6.13: Linear continuum extrapolation of the balanced data for the critical temperature from this work [6] (red circles and red solid line) and the corresponding extrapolation of the data from [26] (blue triangles and dashed blue line).

6.6 Comparison with the literature

Our final result for the critical temperature in physical units is $T_c/\varepsilon_F = 0.171(5)$. This value is significantly higher than the previous result from [26], where $T_c/\varepsilon_F = 0.152(7)$. In [64] the result of [26] was found to be in agreement with a continuous spacetime DDMC method. As our method uses the same procedure as [26] to obtain the continuum limit of the critical temperature we are able to directly compare our data at finite lattice spacing, as shown in Fig. 6.13. From the plot we can see that the two data sets are consistent with each other within statistical error. The difference in the continuum result could be attributed to the different fitting range. In this work we only fit points with $\nu^{1/3} < 0.75$, while points at higher values of the filling factor were included in [26]. If the filling factor is too high second order lattice corrections become significant and can distort the correct continuum result. In support of this, note that the three lowest density points from [26] lie above the linear extrapolation.

The authors of [23] found an upper bound of $T_c/\varepsilon_F \lesssim 0.15(1)$. They used an auxiliary field Monte Carlo approach and extracted the critical temperature from the finite-size scaling of the condensate fraction using the same procedure as in [26]. The difference between our results might be attributed to the approximation made through this fitting method, which was discussed in chapter 3. A less recent result by the same group [24, 25] is $T_c/\varepsilon_F = 0.23(2)$. Through extrapolating Monte Carlo results of low-density neutron matter, the authors of [65] found a value of $T_c/\varepsilon_F = 0.189(12)$ at

unitarity. Their value agrees with our result within errors. This work does not use the finite-size scaling approach with systematic error, but determines T_c from the inflexion point of the interpolated curve of the order parameter [66]. There are also results obtained with the Restricted Path Integral Monte Carlo method [22], $T_c/\varepsilon_F \approx 0.245$, and an upper bound of $T_c/\varepsilon_F < 0.14$ obtained with a hybrid Monte Carlo method [21].

For completeness we also compare with several analytical predictions. A brief overview over the methods was given in section 1.3. With the $1/N$ -expansion [15] one obtains $T_c/\varepsilon_F = 0.136$ to leading order in $1/N$. The beyond mean-field calculation [20] yields $T_c/\varepsilon_F = 0.225$, however this result was matched with the less recent Monte Carlo result from [24, 25], which has since then been updated to a lower value [23]. A value of $T_c/\varepsilon_F = 0.160$ was obtained with the self-consistent approach [16]. Results from the ϵ -expansion [17, 18] include $T_c/\varepsilon_F = 0.249$ using the expansion around $d = 4$ and several other values obtained from expansions around two and four dimensions with different extrapolations. Together the results from these extrapolations range around $T_c/\varepsilon_F = 0.180(12)$, see [19] for a review. For comparison, the critical temperature in the BEC limit is $T_{\text{BEC}} = 0.218\varepsilon_F$.

The authors of [63] conjecture that the leading order change of the critical temperature is linear in $k_F r_e$, where r_e is the effective range of the potential, with a model independent coefficient. Using the extrapolation of the balanced data our result for the linear slope is $\Delta T_c/\varepsilon_F = -0.16(1)$, which is larger in magnitude than the value from [26].

Our result for the energy per particle $E/E_{\text{FG}} = 0.440(15)$ shows excellent agreement with the value $E/E_{\text{FG}} = 0.45(1)$ at T_c quoted in [23]. The value quoted in [26] is $E/N\varepsilon_F = 0.31(1)$, which roughly corresponds to $E/E_{\text{FG}} = 0.52(2)$. Our result for the chemical potential $\mu/\varepsilon_F = 0.429(7)$ differs from $\mu/\varepsilon_F = 0.493(14)$ quoted in [26], but is consistent with the value $\mu/\varepsilon_F = 0.43(1)$ quoted in [23]. Although the numerical method used in [23] is different from our approach, our results for the energy per particle and the chemical potential are in excellent agreement with each other. This supports our claim that the discrepancy in the critical temperature between [23] and this work is due to the systematic error in the finite-size scaling analysis of the order parameter used in [23]. Analytical results for the chemical potential and the energy per particle include $\mu/\varepsilon_F = 0.459$ and $E/N\varepsilon_F = 0.400$ from [20], $\mu/\varepsilon_F = 0.394$ and $E/N\varepsilon_F = 0.304$ from [16] and $\mu/\varepsilon_F = 0.18$ and $E/N\varepsilon_F = 0.212$ from [18].

Since the chemical potential and the energy are expected to stay almost constant at temperatures below T_c we also make a comparison to values from the literature obtained at zero temperature. In the zero temperature limit the quantities μ/ε_F and E/E_{FG} are equal and Monte Carlo estimates range between approximately 0.40(1) and 0.44(1) [67, 68, 69, 70]. Our value for the chemical potential falls within this range, the value for the total energy is slightly higher, which is consistent with the fact that the energy must increase at finite temperature. These numerical estimates are consistent

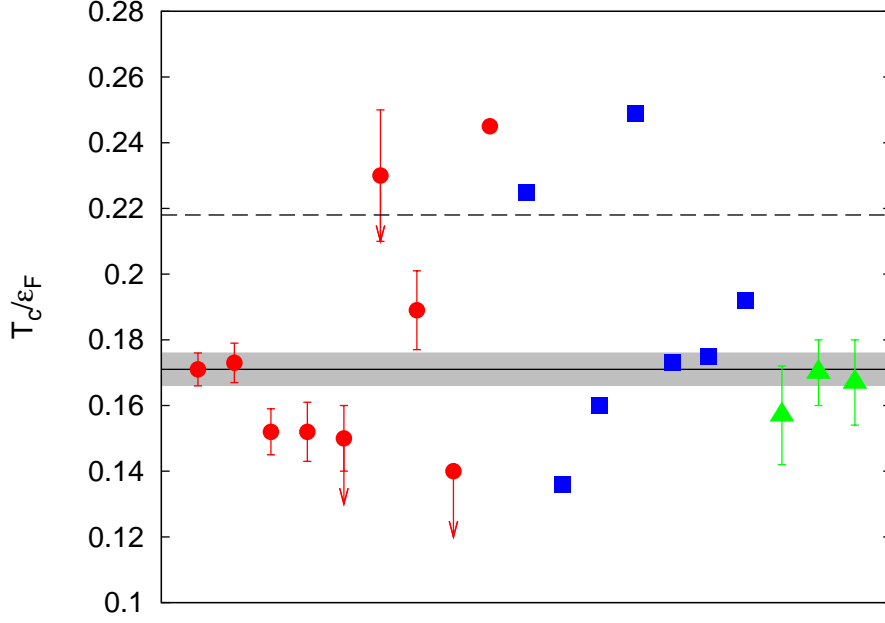


Figure 6.14: Different predictions for the critical temperature at unitarity from the literature. Red circles denote numerical, blue squares analytical, and green triangles experimental results. The solid line and the shaded area denote our most precise result and the error margin. From left to right the numerical results are: the result from this work [6], the result from this work using only balanced data [6], and the results from [26, 64, 23, 24, 65, 21, 22]. The analytical results are from [20, 15, 16] and four results obtained with the ϵ -expansion [17, 18]. The experimental results are from [77, 78, 79]. For comparison the dashed line denotes the critical temperature in the BEC limit.

with experiment [31, 71, 72].

Some predictions for the finite temperature contact density are also available, for instance with a T -matrix approach [73] or by extracting the contact from the large frequency tail of the shear viscosity [74]. The theoretical prediction [75] uses a nonperturbative virial expansion at high temperatures and compares different approximative strong coupling theories at low temperatures. With the auxiliary field quantum Monte Carlo approach the contact can be extracted from the high momentum tail of the density distribution [76]. Our result for the contact density at the critical point is in good agreement with all these predictions. There are also results obtained at temperatures much lower than T_c (see [62] and references therein).

Finally, we make a comparison with recent experimental studies of the homogeneous unitary Fermi gas. A direct measurement of the critical temperature and the chemical potential of the uniform gas has been presented in [77]. Their experimental value $T_c/\varepsilon_F = 0.157(15)$ agrees well with our result. However, the value of the chemical potential at the critical point $\mu/\varepsilon_F = 0.49(2)$ differs from our value. Another experimental determination of the critical temperature and thermodynamic functions, including the

energy and the chemical potential, is described in [78]. Their values $T_c/\varepsilon_F = 0.17(1)$ and $\mu/\varepsilon_F = 0.43(1)$ at T_c show excellent agreement with our results. Their result for the energy per particle $E/N\varepsilon_F = 0.34(2)$ at T_c is higher than our value. In another experimental work [80] an estimate for the critical temperature at zero imbalance is extrapolated from data at higher values of imbalance. In the most recent experimental study of the superfluid transition of a homogeneous unitary Fermi gas [79] the critical temperature is determined from the sudden rise of the specific heat at the critical point, yielding $T_c/\varepsilon_F = 0.167(13)$, which agrees very well with our result. Their value for the chemical potential at T_c is $\mu/\varepsilon_F = 0.42(1)$, which is also consistent with our result. An experimental value for the contact density of the homogeneous unitary Fermi gas at zero temperature, $\mathcal{C}/\varepsilon_F^2 = 0.1184(64)$, is presented in [81]. In Fig. 6.14 we compare the different values of the critical temperature found in the literature with our results.

Observables beyond the critical point

So far we have been limited to observables calculated at the critical point. Now we want to study how the chemical potential, the energy per particle and the contact density change with temperature. Although the lattice temperature $T = 1/\beta$ is a tunable parameter, fixing the physical temperature for different filling factors is a non-trivial task. The critical point is special in this respect, as it has a unique physical property that allows us to distinguish it from other points in the phase diagram. By looking at the behaviour of the order parameter we can identify the critical lattice temperature for any given value of the lattice chemical potential μ , and hence create a linear extrapolation, for instance like the one presented in Fig. 6.2. Hence it is convenient to use the lattice critical temperature $T_c(\mu)$ as a benchmark to fix the temperature scale.

When working on the lattice, in addition to the physical length scale determined by the interparticle distance we have another (artificial) length scale given by the lattice spacing b . The lattice spacing is responsible for the non-zero slope of the linear extrapolations of physical observables and is eventually removed through taking the continuum limit. Remember from chapter 2 that we set the lattice spacing via $\nu = nb^3$. For instance we could have used an experimental value for the density n of an atomic gas at the critical point to compute b at any given filling factor in physical units. In practice, due to the universality of the unitary Fermi gas, a matching with experimental values is not necessary.

Now let us vary the temperature. The simplest approach is to hold the lattice chemical potential fixed and to vary $T = 1/\beta$. We now set the lattice spacing such that it is independent of T ,

$$b(\mu, T) = b(\mu, T_c) = \left(\frac{\nu(\mu, T_c)}{n(\mu, T_c)} \right)^{1/3}. \quad (7.1)$$

This can also be understood as a temperature-independent renormalisation condition. If we fix the lattice temperature ratio $r = T(\mu)/T_c(\mu)$ for each value of the lattice chemical potential, we will move along a line of constant temperature $T = rT_c$ analogous to the linear extrapolations at T_c discussed in the previous chapter.

For coarse lattices this scheme will break down as the presence of the lattice spacing will change the relation between ν and T . We need to ensure that for the temperature

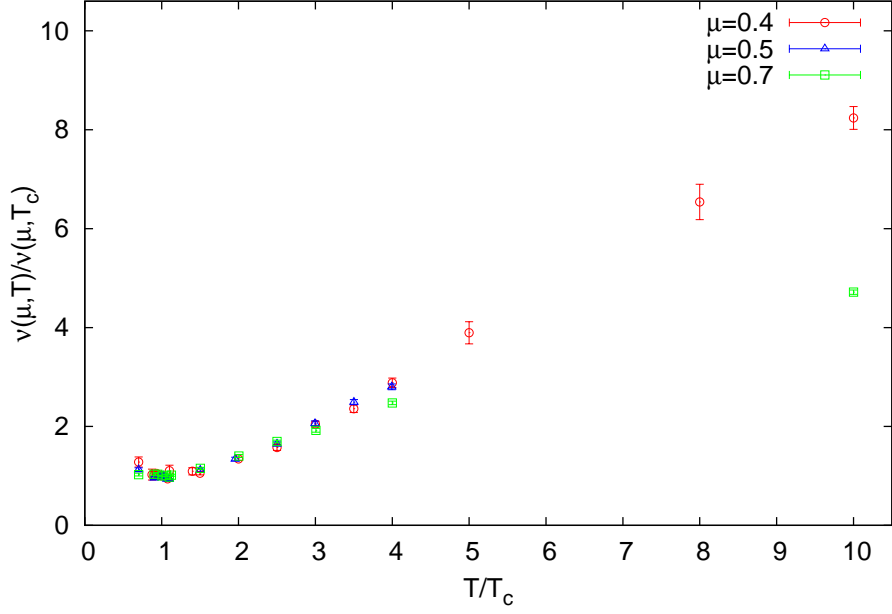


Figure 7.1: The normalised filling factor $\nu(\mu, T)/\nu(\mu, T_c)$ versus the temperature ratio T/T_c for different values of the lattice chemical potential μ .

range considered in this analysis the lattice artefacts are negligible. Note that the filling factor normalised by its value at the critical point must be independent of the lattice chemical potential. Figure 7.1 shows the normalised filling factor versus T/T_c for several values of μ . It is clearly visible that we can access temperature ratios $T/T_c \leq 4$ provided that the chemical potential is small enough. For instance the chemical potential value $\mu = 0.7$ in lattice units is too large to access the temperature ratio $T/T_c = 4$, but small enough for $T/T_c \leq 3$. The deviation becomes more evident for very large temperature ratios. In general, high temperatures are hard to access as they require us to go to very low chemical potentials and consequently very large lattice sizes.

In the following sections we will study the temperature dependence of the chemical potential, the energy per particle and the contact density of the balanced unitary Fermi gas. Data was taken below the critical temperature at $T/T_c = 0.7$ and for six different temperature ratios above the critical temperature, up to $T/T_c = 4$. This analysis is still work in progress and the results presented in the following are preliminary. In particular, simulations at the lowest filling factor that was used for the analysis at T_c are still ongoing. At high temperature and low filling finite-size effects are more pronounced and force us to use large lattice sizes which require long simulation times.

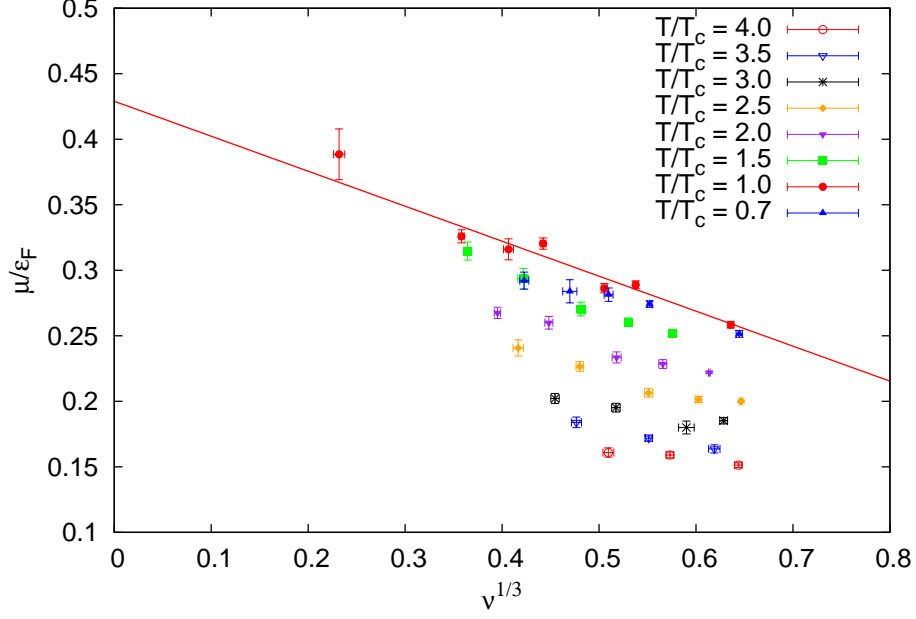


Figure 7.2: The chemical potential versus filling factor for different temperatures. The continuum limit corresponds to $\nu \rightarrow 0$. The solid line is the continuum extrapolation at T_c .

T/T_c	linear fit for μ/ε_F	$\chi^2/\text{d.o.f.}$
4.0	$0.20(2) - 0.08(3)\nu^{1/3}$	0.76
3.5	$0.25(2) - 0.14(4)\nu^{1/3}$	0.16
3.0	$0.25(1) - 0.10(2)\nu^{1/3}$	1.37
2.5	$0.29(1) - 0.15(2)\nu^{1/3}$	3.44
2.0	$0.35(1) - 0.20(2)\nu^{1/3}$	1.67
1.5	$0.41(2) - 0.27(3)\nu^{1/3}$	1.12
0.7	$0.38(1) - 0.20(2)\nu^{1/3}$	0.80

Table 7.1: Linear fits of the numerical data for the chemical potential μ/ε_F at different temperatures.

7.1 The equation of state for the density

Figure 7.2 displays the numerical data for the chemical potential at different temperatures. For lucidity the linear fits at $T \neq T_c$ are not shown, but a list of all fit results is given in Table 7.1. It is clearly visible from the plot that the chemical potential decreases with increasing temperature. Figure 7.3 shows the continuum limit of the chemical potential as a function of the temperature.

For comparison with the literature we will now rewrite the equation of state in terms of the density as a function of $\beta\mu$. At unitarity the dimensionless density $n\lambda_B^3$, where $\lambda_B = \sqrt{2\pi/mT}$ is the thermal de Broglie wavelength, must be a universal function of

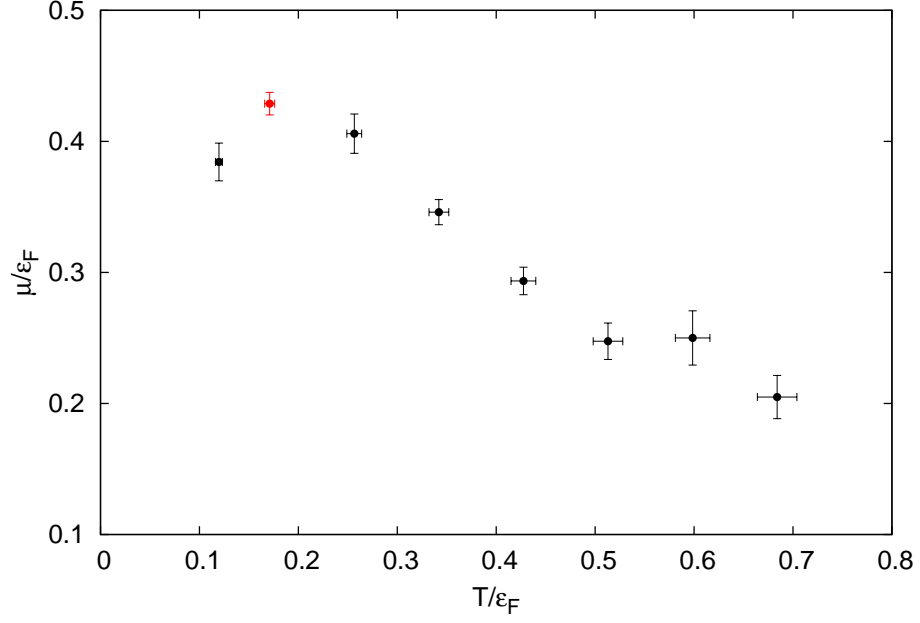


Figure 7.3: The chemical potential in the continuum limit versus the temperature. The red symbol indicates the value at the critical point.

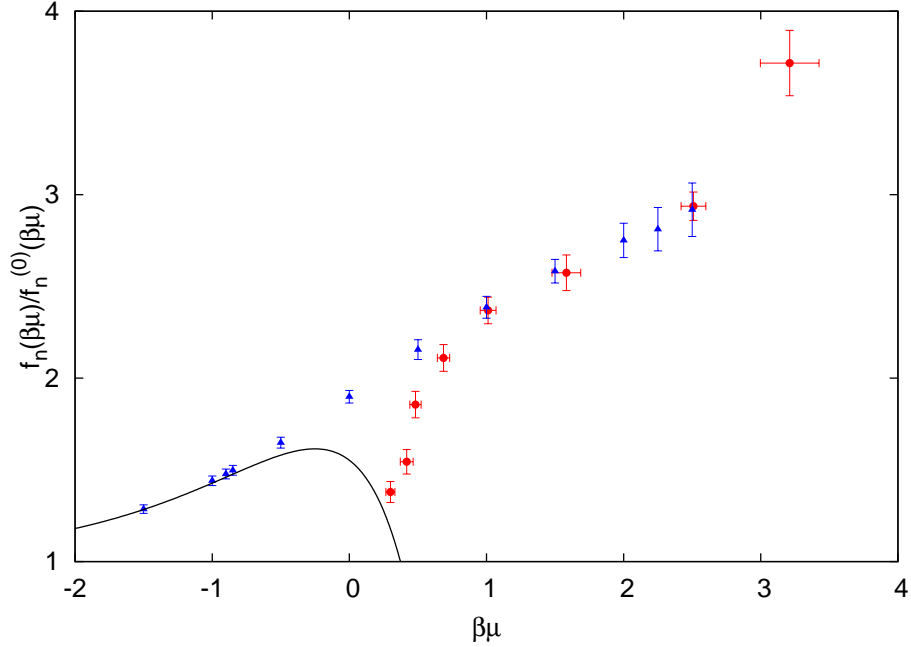


Figure 7.4: The density $f_n(\beta\mu)/f_n^{(0)}(\beta\mu)$ normalised in terms of the density of the ideal gas. We compare our results (red circles) with preliminary results obtained with bold diagrammatic Monte Carlo [82] (blue triangles) and the third order virial expansion [83] (solid line).

$\beta\mu$,

$$n\lambda_B^3 = f_n(\beta\mu). \quad (7.2)$$

Using the definition of the Fermi energy $\varepsilon_F = (3\pi^2 n)^{2/3}/(2m)$ we can rewrite

$$f_n(\beta\mu) = n\lambda_B^3 = \frac{8}{3\sqrt{\pi}}(T/\varepsilon_F)^{-3/2}. \quad (7.3)$$

For an ideal two-component Fermi gas this universal function can be evaluated explicitly from the Fermi-Dirac distribution,

$$f_n^{(0)}(\beta\mu) = n^{(0)}\lambda_B^3 = 2 \int \frac{d^3p}{(2\pi)^3} \frac{1}{1 + e^{\beta(\frac{p^2}{2m} - \mu)}} \left(\frac{2\pi}{mT} \right)^{3/2} = -2\text{Li}_{3/2}(-e^{\beta\mu}), \quad (7.4)$$

where $\text{Li}_n(z) = \sum_{k=1}^{\infty} (z^k/k^n)$ is the polylogarithm. Figure 7.4 shows our results for the density normalised in terms of the density of the ideal gas. We also compare with the unpublished preliminary results obtained using bold diagrammatic Monte Carlo¹ [82] and with a theoretical prediction valid at high temperatures obtained from the virial expansion (the power series expansion of thermodynamic quantities in terms of the fugacity $e^{\beta\mu}$). For theoretical background on the virial expansion of the unitary Fermi gas and the second virial coefficient see for instance [85] and references therein. The third virial coefficient for the unitary Fermi gas was calculated in [83]. We can see good agreement between our results and the results from [82]. At very high temperatures lattice artefacts become more pronounced and the results start to deviate. The results obtained with the auxiliary field quantum Monte Carlo method [23] (not shown in the plot) also agree with our predictions.

7.2 The equation of state for the pressure

The numerical results for the energy per particle for different temperatures are shown in Fig. 7.5. Again only the linear extrapolation at T_c is shown and the fit results are summarised in Table 7.2. As expected the energy per particle increases with increasing temperature. A plot of E/E_{FG} in the continuum limit versus the temperature is shown in Fig. 7.6.

Using universal thermodynamic relations we can express the pressure P of the gas in terms of the temperature, the chemical potential and the energy density. On dimensional grounds we obtain

$$P\lambda_B^3 = T f_P(\beta\mu), \quad (7.5)$$

where $f_P(\beta\mu)$ is a universal function. The pressure can be related to the energy density

¹A more recent version of these results and a description of the method can be found in [84].

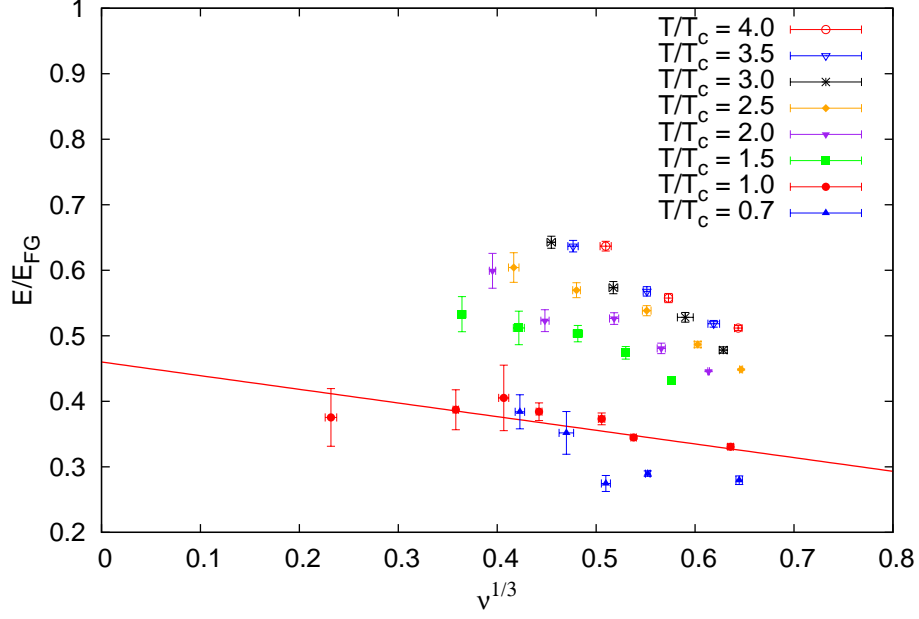


Figure 7.5: The energy per particle versus filling factor for different temperatures. The continuum limit corresponds to $\nu \rightarrow 0$. The solid line is the continuum extrapolation at T_c .

T/T_c	linear fit for E/E_{FG}	$\chi^2/\text{d.o.f.}$
4.0	$1.08(5) - 0.89(7)\nu^{1/3}$	4.45
3.5	$1.03(5) - 0.82(8)\nu^{1/3}$	0.48
3.0	$1.06(4) - 0.92(6)\nu^{1/3}$	1.21
2.5	$0.96(3) - 0.79(5)\nu^{1/3}$	1.76
2.0	$0.86(4) - 0.68(6)\nu^{1/3}$	2.39
1.5	$0.79(4) - 0.63(8)\nu^{1/3}$	1.53
0.7	$0.39(4) - 0.18(7)\nu^{1/3}$	4.58

Table 7.2: Linear fits of the numerical data for the energy per particle E/E_{FG} at different temperatures.

of the gas [47] via $P = (2/3)E/V$. From this we get

$$f_P(\beta\mu) = \frac{P\lambda_B^3}{T} = \frac{2E\lambda_B^3}{3VT} = \frac{16}{15\sqrt{\pi}}(E/E_{\text{FG}})(T/\varepsilon_F)^{-5/2}. \quad (7.6)$$

Again we would like to normalise the pressure in terms of the pressure of the ideal two-component Fermi gas,

$$f_P^{(0)}(\beta\mu) = \frac{2E^{(0)}\lambda_B^3}{3VT} = \frac{4}{3T} \int \frac{d^3p}{(2\pi)^3} \frac{p^2/2m}{1 + e^{\beta(\frac{p^2}{2m} - \mu)}} \left(\frac{2\pi}{mT} \right)^{3/2} = -2\text{Li}_{5/2}(-e^{\beta\mu}). \quad (7.7)$$

Figure 7.7 shows our results for the equation of state for the pressure. For comparison

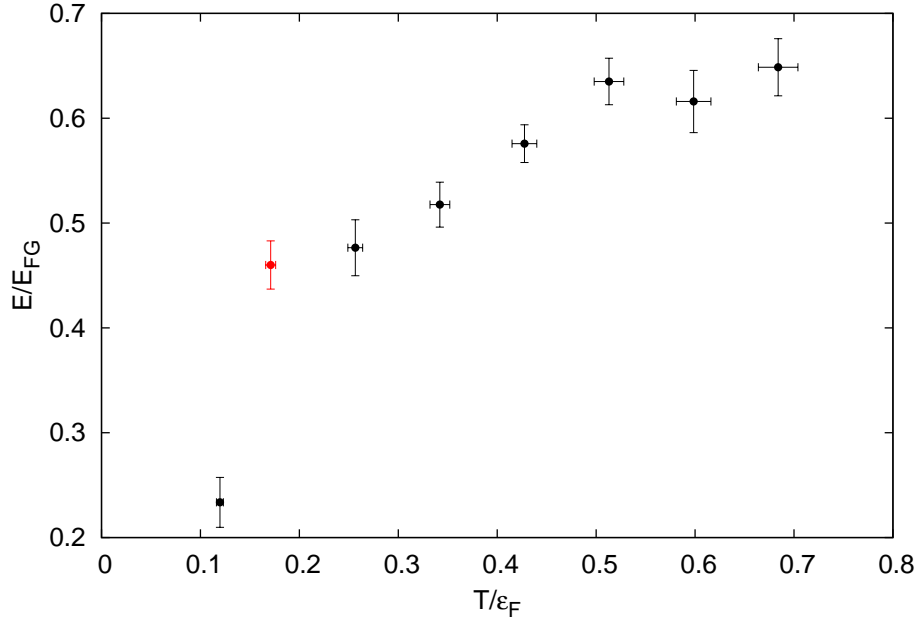


Figure 7.6: The energy per particle in the continuum limit versus the temperature. The red symbol indicates the value at the critical point.

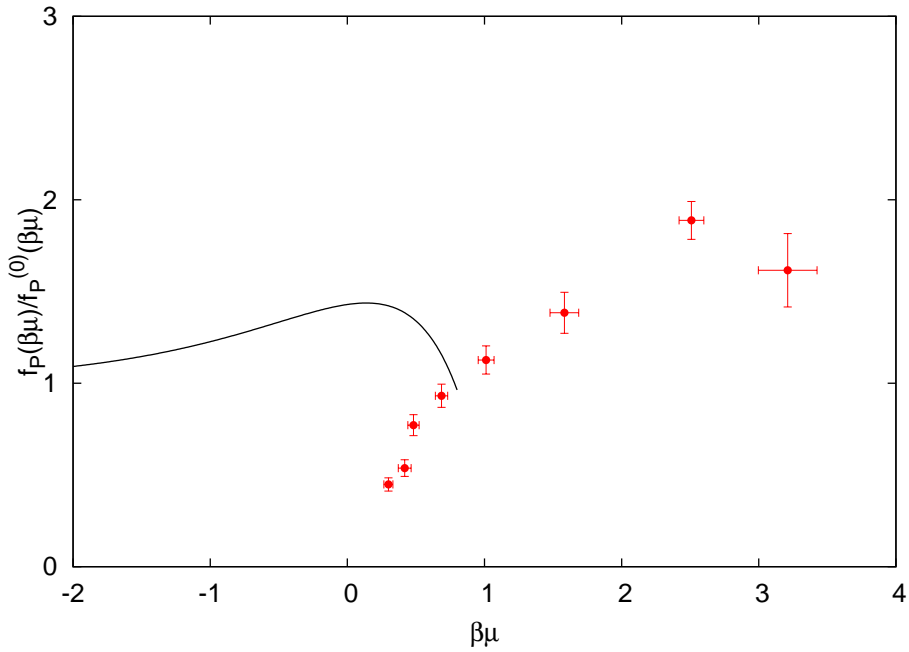


Figure 7.7: The pressure $f_P(\beta\mu)/f_P^{(0)}(\beta\mu)$ normalised in terms of the pressure of the ideal gas. We compare our results (red circles) with the third order virial expansion [83] (solid line).

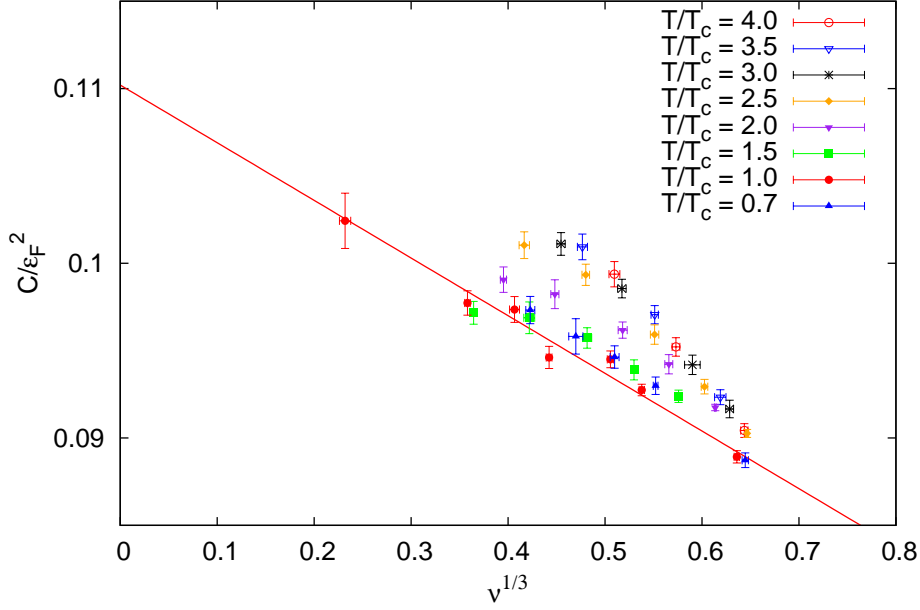


Figure 7.8: The contact density versus filling factor for different temperatures. The continuum limit corresponds to $\nu \rightarrow 0$. The solid line is the continuum extrapolation at T_c .

we also show the high temperature prediction from the virial expansion. The agreement here is less good than in the case of the equation of state for the density. We expect an improvement of the data when results at the lowest filling factor become available.

7.3 The temperature dependence of the contact

Figure 7.8 shows our data for the contact density at different temperatures and the linear fit at T_c . Like the energy per particle the contact appears to increase with increasing temperature. The fit results are listed in Table 7.3. Figures 7.9 and 7.10 show the contact density versus the temperature and versus $\beta\mu$ in the continuum limit. We also compare our results to the literature. There is a discrepancy to the preliminary results from [82] where the contact was found to be increasing with increasing $\beta\mu$. On the other hand we see excellent agreement with the auxiliary field quantum Monte Carlo results [76] that show the same trend of the contact density with respect to $\beta\mu$ as our results. We also agree with the T -matrix calculation in [73]. Our result at the lowest temperature value $T/T_c = 0.7$ shows excellent agreement with the zero-temperature experimental result [81].

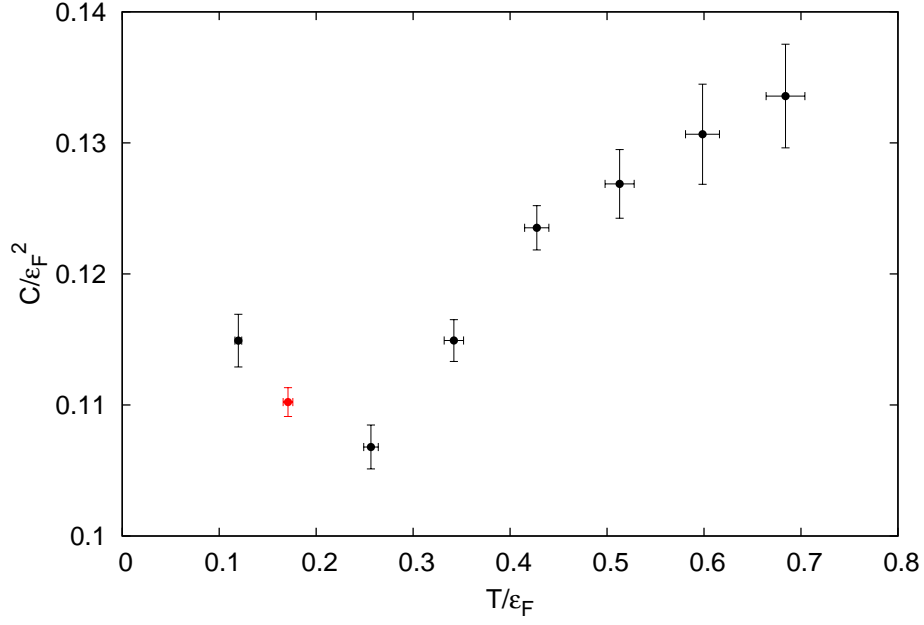


Figure 7.9: The contact density in the continuum limit versus the temperature. The red symbol indicates the value at the critical point.

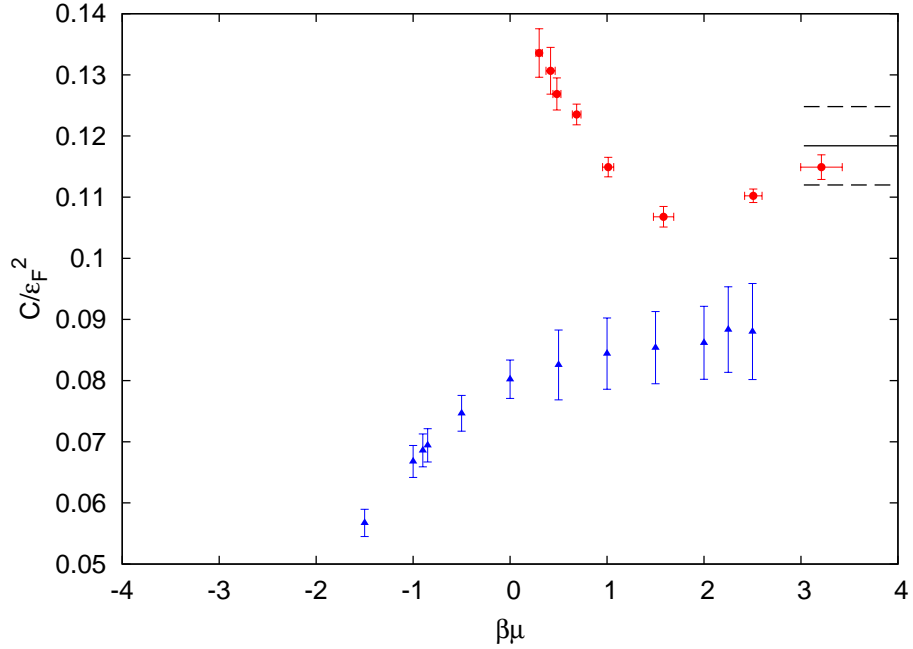


Figure 7.10: The contact density in the continuum limit versus $\beta\mu$. Red circles are the results from this work, blue triangles the preliminary results from [82] and the lines indicate the experimental zero-temperature result [81] with the error margin.

T/T_c	linear fit for $\mathcal{C}/\varepsilon_F^2$	$\chi^2/\text{d.o.f.}$
4.0	$0.134(4) - 0.067(7)\nu^{1/3}$	0.01
3.5	$0.131(4) - 0.062(7)\nu^{1/3}$	0.72
3.0	$0.127(3) - 0.056(5)\nu^{1/3}$	0.66
2.5	$0.124(2) - 0.051(3)\nu^{1/3}$	1.43
2.0	$0.115(2) - 0.038(3)\nu^{1/3}$	1.79
1.5	$0.107(2) - 0.025(3)\nu^{1/3}$	1.16
0.7	$0.115(2) - 0.040(4)\nu^{1/3}$	0.43

Table 7.3: Linear fits of the numerical data for the contact density $\mathcal{C}/\varepsilon_F^2$ at different temperatures.

Simulation of the Boltzmann equation

The previous chapters were devoted to the homogeneous unitary Fermi gas at or near the critical point. Now we will move to higher temperatures, when a semiclassical description is applicable. We shall also include an external potential and consider a range of large but finite values for the scattering length a . Our goal is to access dynamical properties, in particular related to spin transport, using a numerical simulation of the Boltzmann equation.

8.1 Distributions in a trap

Again we consider a system of two-component fermions with equal mass m , labelled by the spin index $s = \{\uparrow, \downarrow\}$. As we have seen in section 1.2, fermions of opposite spin can interact via s -wave scattering and the cross section is given by (1.13),

$$\sigma = \frac{4\pi a^2}{1 + k^2 a^2}, \quad (8.1)$$

where $2k = |\mathbf{p}_\uparrow - \mathbf{p}_\downarrow| = |\mathbf{p}_{\text{rel}}|$ is the relative momentum of the two atoms.

We assume that the system is in the normal phase and that the temperature is sufficiently high, so that the two spin distributions can be described semiclassically in terms of functions $f_s(\mathbf{r}, \mathbf{p}, t)$ [3, 13]. The distribution function $f_s(\mathbf{r}, \mathbf{p}, t)$ gives the probability density to find a particle with spin s at the phase space point (\mathbf{r}, \mathbf{p}) at the time t . Within the local density approximation the equilibrium distribution for fermions is given by the Fermi-Dirac distribution

$$f_s^{(\text{FD})}(\mathbf{r}, \mathbf{p}) = \frac{1}{e^{(p^2/2m + V(\mathbf{r}) - \mu_s)/T} + 1}, \quad (8.2)$$

where T is the temperature and μ_s the chemical potential defined by the normalisation condition

$$N_s = N/2 = \int d^3r n_s(\mathbf{r}, t) = \int d^3r \int \frac{d^3p}{(2\pi)^3} f_s(\mathbf{r}, \mathbf{p}, t). \quad (8.3)$$

The atom number for each species is assumed to be equal, $N_\uparrow = N_\downarrow = N/2$, and will be

held fixed during the simulation. The trapping potential is assumed to be harmonic,

$$V(\mathbf{r}) = \frac{1}{2}m(\omega_x^2 x^2 + \omega_y^2 y^2 + \omega_z^2 z^2), \quad (8.4)$$

with the three trapping frequencies ω_x , ω_y and ω_z . In the following we will only consider the isotropic case $\omega_x = \omega_y = \omega_z$ or a cigar shaped trap with $\omega_z < \omega_x = \omega_y$.

It will prove useful to derive the corresponding energy distribution by performing a change of variables,

$$f_s^{(\text{FD})}(E) = \int d^3r \frac{d^3p}{(2\pi)^3} f_s^{(\text{FD})}(\mathbf{r}, \mathbf{p}) \delta(E - E(\mathbf{r}, \mathbf{p})) \quad (8.5)$$

$$= \int_{E(\mathbf{r}, \mathbf{p})=E} d^3r \frac{d^3p}{(2\pi)^3} \frac{f_s^{(\text{FD})}(\mathbf{r}, \mathbf{p})}{\sqrt{\sum_i (\partial E / \partial r_i)^2 + \sum_i (\partial E / \partial p_i)^2}}, \quad (8.6)$$

where $E(\mathbf{r}, \mathbf{p}) = p^2/2m + V(\mathbf{r})$ is the total energy. Performing the integral in momentum space we then obtain

$$f_s^{(\text{FD})}(E) = \frac{1}{e^{(E-\mu_s)/T} + 1} \frac{m}{\pi^2} \int_{E-V(\mathbf{r}) \geq 0} d^3r \frac{E - V(\mathbf{r})}{\sqrt{2(E - V(\mathbf{r}))/m + m^2 \sum_i \omega_i^4 r_i^2}}. \quad (8.7)$$

On dimensional grounds and given the integration condition $E - V(\mathbf{r}) \geq 0$ it is now easy to see that the integral must be proportional to E^2 . From normalisation we obtain

$$f_s^{(\text{FD})}(E) = \frac{E^2/2\omega_0^3}{e^{(E-\mu_s)/T} + 1}, \quad (8.8)$$

where $\omega_0 = (\omega_x \omega_y \omega_z)^{1/3}$ is the geometric average over the three trapping frequencies. The chemical potential at zero temperature defines the Fermi energy,

$$\tilde{\varepsilon}_F = \mu_s(T = 0), \quad (8.9)$$

which in the presence of interactions differs from the Fermi energy ε_F of the free non-interacting gas [3]. An explicit expression for $\tilde{\varepsilon}_F$ can be obtained from the normalisation of the energy distribution at zero temperature,

$$N_s = \lim_{T \rightarrow 0} \frac{1}{2\omega_0^3} \int_0^\infty \frac{E^2 dE}{e^{(E-\tilde{\varepsilon}_F)/T} + 1} = \frac{1}{2\omega_0^3} \int_0^{\tilde{\varepsilon}_F} E^2 dE = \frac{\tilde{\varepsilon}_F^3}{6\omega_0^3}, \quad (8.10)$$

which yields

$$\tilde{T}_F = \tilde{\varepsilon}_F = (6N_s)^{1/3} \omega_0 = (3N)^{1/3} \omega_0. \quad (8.11)$$

For better comparison with the experiment we will sometimes also use ε_F as a unit of energy. Since in the presence of an external potential the gas is no longer homogeneous,

we need to redefine ε_F in terms of a local density. We take

$$T_F = \varepsilon_F = \frac{1}{2m}(3\pi^2 n(\mathbf{0}))^{2/3}, \quad (8.12)$$

where $n(\mathbf{0})$ is the total atomic density $n(\mathbf{0}) = n_\uparrow(\mathbf{0}) + n_\downarrow(\mathbf{0})$ in the trap centre. The local density of the trapped gas is temperature-dependent and consequently ε_F and $k_F = \sqrt{2m\varepsilon_F}$ defined in terms of $n(\mathbf{0})$ will change if the temperature of the system changes. The zero-temperature Fermi energy $\tilde{\varepsilon}_F$ is defined in terms of only the total particle number and the trap geometry and stays invariant if we hold these quantities fixed. Note that in contrast to the dilute homogeneous gas which can be described entirely in terms of the density, the temperature and the scattering length, the trapping frequencies introduce three additional scales into the problem.

The zero-temperature Fermi energy $\tilde{\varepsilon}_F$ can be used to determine the typical scales of the cloud,

$$\tilde{\varepsilon}_F = \frac{\tilde{k}_F^2}{2m} = \frac{1}{2}m\omega_x^2 R_x^2 = \frac{1}{2}m\omega_y^2 R_y^2 = \frac{1}{2}m\omega_z^2 R_z^2, \quad (8.13)$$

where \tilde{k}_F is the zero-temperature Fermi momentum and R_x , R_y and R_z are the Thomas-Fermi radii in the three spatial directions. The Fermi momentum and the Thomas-Fermi radii give the width of the zero-temperature momentum and density distributions respectively. They are therefore useful quantities to describe the extent of the fermionic cloud in momentum and coordinate space. To see the correspondence between these quantities and the widths of the distributions let us look, for instance, at the Fermi-Dirac density distribution in the zero-temperature limit,

$$\lim_{T \rightarrow 0} n_s^{(\text{FD})}(\mathbf{r}) = \lim_{T \rightarrow 0} \int \frac{d^3p}{(2\pi)^3} \frac{1}{e^{(p^2/2m + V(\mathbf{r}) - \mu_s)/T} + 1} = \int_{p^2/2m + V(\mathbf{r}) \leq \tilde{\varepsilon}_F} \frac{d^3p}{(2\pi)^3}. \quad (8.14)$$

Using rotational symmetry we obtain

$$\lim_{T \rightarrow 0} n_s^{(\text{FD})}(\mathbf{r}) = \int_0^{\sqrt{2m(\tilde{\varepsilon}_F - V(\mathbf{r}))}} \frac{4\pi p^2 dp}{(2\pi)^3} = \frac{1}{6\pi^2} (2m(\tilde{\varepsilon}_F - V(\mathbf{r})))^{3/2} \quad (8.15)$$

and inserting the definition of the Thomas-Fermi radii from (8.13) we arrive at

$$\lim_{T \rightarrow 0} n_s^{(\text{FD})}(\mathbf{r}) = \frac{8N_s}{\pi^2 R_x R_y R_z} \left(1 - \frac{x^2}{R_x^2} - \frac{y^2}{R_y^2} - \frac{z^2}{R_z^2} \right)^{3/2}. \quad (8.16)$$

Analogously

$$\lim_{T \rightarrow 0} n_s^{(\text{FD})}(\mathbf{p}) = \lim_{T \rightarrow 0} \int d^3r f_s^{(\text{FD})}(\mathbf{r}, \mathbf{p}) = \frac{8N_s}{\tilde{k}_F^3} \left(1 - \frac{p^2}{\tilde{k}_F^2} \right)^{3/2}. \quad (8.17)$$

Note that unlike the density distribution the momentum distribution is isotropic in the three directions, even if the trap frequencies are not equal.

For sufficiently high temperatures the exponential $e^{-(p^2/2m+V(\mathbf{r})-\mu_s)/T}$ becomes small such that we can expand the Fermi-Dirac distribution in this quantity and obtain

$$f_s^{(\text{FD})}(\mathbf{r}, \mathbf{p}) = \frac{e^{-(p^2/2m+V(\mathbf{r})-\mu_s)/T}}{1 + e^{-(p^2/2m+V(\mathbf{r})-\mu_s)/T}} \rightarrow e^{-(p^2/2m+V(\mathbf{r})-\mu_s)/T}, \quad (8.18)$$

which is the classical Maxwell-Boltzmann distribution. Using the normalisation condition (8.3) we can rewrite it explicitly in terms of the particle number rather than the chemical potential,

$$f_s^{(\text{MB})}(\mathbf{r}, \mathbf{p}) = N_s \frac{\omega_0^3}{T^3} e^{-(p^2/2m+V(\mathbf{r}))/T}. \quad (8.19)$$

The corresponding energy distribution is

$$f_s^{(\text{MB})}(E) = N_s \frac{E^2}{2T^3} e^{-E/T}. \quad (8.20)$$

The classical Maxwell-Boltzmann distribution is applicable if the de Broglie wavelength is much smaller than the average interparticle distance, which corresponds to $T/\tilde{T}_F \gtrsim 1$.

8.2 The Boltzmann equation

Within the scope of kinetic gas theory a many-body system is treated as a collection of discrete particles moving randomly [49, 86]. If the system is sufficiently dilute such that the size of the particles is negligible compared to the interparticle separation, the particles can be viewed as structureless point-like objects. They will propagate freely most of the time, interparticle interactions being limited to rare elastic two-body collisions. If the de Broglie wavelength is sufficiently small the free propagation follows the classical equations of motion.

We are interested in the non-equilibrium properties of the system and hence want to look at the time-evolution of the distribution function f_s at the phase space point (\mathbf{r}, \mathbf{p}) . For a closed system the distribution function can only change due to collisional processes. Hence its total time derivative can be written as

$$\frac{d}{dt}f_s = \frac{\partial}{\partial t}f_s + \dot{\mathbf{p}} \cdot \nabla_{\mathbf{p}}f_s + \dot{\mathbf{r}} \cdot \nabla_{\mathbf{r}}f_s = -I, \quad (8.21)$$

where the quantity I represents the effect of two-body collisions and in general depends on the two-body distribution function $f_{s\bar{s}}^{(2)}(\mathbf{r}_s, \mathbf{p}_s, \mathbf{r}_{\bar{s}}, \mathbf{p}_{\bar{s}}, t)$. The analogous time-evolution equation for $f^{(2)}$ will in turn involve the three-body distribution $f^{(3)}$ and so on [86]. In order to obtain a closed form for the time-evolution equation we need to make an additional assumption. In a dilute gas of point-like particles with short-range

interactions collisions are rare and hence it is justified to assume that before a collision the two particles are uncorrelated,

$$f_{s\bar{s}}^{(2)}(\mathbf{r}_s, \mathbf{p}_s, \mathbf{r}_{\bar{s}}, \mathbf{p}_{\bar{s}}, t) = f_s(\mathbf{r}_s, \mathbf{p}_s, t) f_{\bar{s}}(\mathbf{r}_{\bar{s}}, \mathbf{p}_{\bar{s}}, t). \quad (8.22)$$

This is called the molecular chaos assumption or Stoßzahlansatz. After the collision of course, the two particles become strongly correlated due to momentum and energy conservation. But since they are unlikely to encounter each other again before scattering on other particles has erased the memory of their prior collision the molecular chaos assumption remains valid. More precisely, it can be shown that the probability for such a repeated scattering event is exponentially small with time [86].

Now let us derive an explicit form for the collisional contribution I taking into account all assumptions discussed above [49]. The change of the distribution function f_s at the phase space point (\mathbf{r}, \mathbf{p}) can be decomposed into a gain and a loss term, the gain term representing atoms of spin s with final state (\mathbf{r}, \mathbf{p}) after the collision and the loss term representing the contribution of collisions from the initial spin s state (\mathbf{r}, \mathbf{p}) into other final states $(\mathbf{r}, \mathbf{p}')$. Now consider a specific collision between a spin s atom in the initial state $(\mathbf{r}, \mathbf{p}_s)$ and an atom of opposite spin \bar{s} in the initial state $(\mathbf{r}, \mathbf{p}_{\bar{s}})$, which brings the two atoms into the final states $(\mathbf{r}, \mathbf{p}'_s)$ and $(\mathbf{r}, \mathbf{p}'_{\bar{s}})$ respectively. Collisions are assumed to be local, meaning that the two atoms are at the same position \mathbf{r} during the collision. The total number of such collisions with fixed initial and final momenta divided by the phase space volume is given by the initial particle density $f_s(\mathbf{r}, \mathbf{p}_s)$ times the probability for each spin s atom to exhibit such a collision. The latter in turn equals the product of the number of possible scattering partners $f_{\bar{s}}(\mathbf{r}, \mathbf{p}_{\bar{s}}) d^3 p_{\bar{s}}$ with the probability to end up in the required final state, $|\mathbf{v}_s - \mathbf{v}_{\bar{s}}| d\sigma = |\mathbf{v}_s - \mathbf{v}_{\bar{s}}| \frac{d\sigma}{d\Omega} d\Omega$, where Ω is the solid angle between the incoming and outgoing relative velocities as discussed in section 1.2. The change of f_s due to all such collisions becomes an integral over all possible initial momenta of the collision partners $\mathbf{p}_{\bar{s}}$ and over all possible angles Ω . For “classical fermions” this collision integral then takes the form

$$I_{\text{class}}[f_s, f_{\bar{s}}] = \int \frac{d^3 p_{\bar{s}}}{(2\pi)^3} \int d\Omega \frac{d\sigma}{d\Omega} \frac{|\mathbf{p}_s - \mathbf{p}_{\bar{s}}|}{m} [f_s f_{\bar{s}} - f'_s f'_{\bar{s}}], \quad (8.23)$$

where the primed variables refer to quantities after the collision. Since fermions obey the Fermi-Dirac statistics a particle can only scatter into a previously unoccupied quantum state. This reduces the scattering probability by a so-called Pauli blocking term proportional to $(1 - f'_s)(1 - f'_{\bar{s}})$. Taking this into account the collision integral reads

$$I[f_s, f_{\bar{s}}] = \int \frac{d^3 p_{\bar{s}}}{(2\pi)^3} \int d\Omega \frac{d\sigma}{d\Omega} \frac{|\mathbf{p}_s - \mathbf{p}_{\bar{s}}|}{m} [f_s f_{\bar{s}} (1 - f'_s)(1 - f'_{\bar{s}}) - f'_s f'_{\bar{s}} (1 - f_s)(1 - f_{\bar{s}})]. \quad (8.24)$$

If we now insert the explicit form for the collision integral and the classical equations

of motion into (8.21) we arrive at the Boltzmann equation which describes the time-evolution of the distribution function $f_s(\mathbf{r}, \mathbf{p}, t)$ for each spin species,

$$\partial_t f_s + (\mathbf{p}/m) \cdot \nabla_r f_s - \nabla_r V \cdot \nabla_p f_s = -I[f_s, f_{\bar{s}}]. \quad (8.25)$$

The left-hand side represents the propagation of the atoms in the potential while the right-hand side stands for the collision integral given by Eq. (8.24) for fermions or by Eq. (8.23) for classical particles.

8.3 Numerical setup

The results presented in the following were published in [8].

Our numerical setup is based to the one described in [87]. We do not attempt to calculate the collision integral (8.24) directly, as this is numerically intractable. Instead we start from the semiclassical picture of a dilute gas of point-like particles propagating in space and scattering on each other via rare elastic two-body collisions. We introduce a discrete time step Δt , such that during each time step the atoms propagate collision-free following their classical trajectories. At the end of each time step collisions between the atoms are evaluated. The point-like particle picture is a discrete approximation of the continuous distribution function $f_s(\mathbf{r}, \mathbf{p}, t)$ through δ -functions, which allows us to handle the propagation step efficiently. In order for this approximation to be accurate we will represent each fermion by several test particles [87, 88, 89]. The higher the ratio \tilde{N}/N of test particles to atoms, the more precisely the continuous distribution function will be approximated,

$$f_s(\mathbf{r}, \mathbf{p}, t) \rightarrow \frac{N_s}{\tilde{N}_s} \sum_{i=1}^{\tilde{N}_s} (2\pi)^3 \delta(\mathbf{r} - \mathbf{r}_i(t)) \delta(\mathbf{p} - \mathbf{p}_i(t)). \quad (8.26)$$

Physical observables need to be rescaled, for instance the test particle cross section becomes $\tilde{\sigma} = \sigma(N/\tilde{N})$. A generic thermal expectation value of a single-particle observable $X(\mathbf{r}, \mathbf{p})$ can be easily calculated within the test particle picture, as the integration reduces to a sum over all test particles,

$$\langle X \rangle = \sum_s \frac{1}{N_s} \int d^3r \frac{d^3p}{(2\pi)^3} f_s(\mathbf{r}, \mathbf{p}, t) X(\mathbf{r}, \mathbf{p}) = \frac{1}{\tilde{N}} \sum_{i=1}^{\tilde{N}} X(\mathbf{r}_i, \mathbf{p}_i). \quad (8.27)$$

The trajectories of the test particles are the same as the trajectories of the atoms and are

given by the stationary solution of the Boltzmann equation with a harmonic potential,

$$r_i(t_{n+1}) = r_i(t_n) \cos(\omega_i \Delta t) + (p_i(t_n)/m\omega_i) \sin(\omega_i \Delta t), \quad (8.28)$$

$$p_i(t_{n+1}) = p_i(t_n) \cos(\omega_i \Delta t) - r_i(t_n) m\omega_i \sin(\omega_i \Delta t). \quad (8.29)$$

Note that since the time step is fixed the trigonometric functions only need to be evaluated once during the entire simulation, so that using the exact solution is more efficient than using the Verlet algorithm, as for instance in Refs. [87, 88], in which case the accelerations need to be recalculated for every time step. The Verlet algorithm is more general as it is applicable for any potential. Since in this work we will only consider harmonic potentials, we will use the exact solution which is both more precise and more efficient to calculate.

We evaluate collisions in the same way as described in [87]. First we test whether a pair of test particles reaches the point of closest approach during the present time step. This condition is important to prevent particles from attempting to collide with each other repeatedly for several consecutive time steps. If the closest approach condition is true we check if the minimal distance d_{\min} of the test particles fulfils the classical condition for scattering: $\pi d_{\min}^2 < \tilde{\sigma}$. If this condition is also satisfied we propose a collision at the time of closest approach. However due to Pauli statistics, even if the classical conditions for scattering are fulfilled, a collision can only take place if the new state of the particles was previously unoccupied. To take this into account we calculate the quantum mechanical scattering probability given by the Pauli term $(1 - f'_s)(1 - f'_s)$ in the collision integral (8.24) and accept or reject the collision according to this probability. Clearly the point-like particle picture is unsuitable for the calculation of this probability. To return to a continuous distribution we therefore have to smear out the δ -functions representing the test particles, e.g. by Gaussians in position and momentum space:

$$\delta(\mathbf{p} - \mathbf{p}_i) \delta(\mathbf{r} - \mathbf{r}_i) \longrightarrow \frac{e^{-(\mathbf{p}-\mathbf{p}_i)^2/w_p^2}}{(\sqrt{\pi}w_p)^3} \frac{e^{-(x-x_i)^2/w_x^2}}{\sqrt{\pi}w_x} \frac{e^{-(y-y_i)^2/w_y^2}}{\sqrt{\pi}w_y} \frac{e^{-(z-z_i)^2/w_z^2}}{\sqrt{\pi}w_z}. \quad (8.30)$$

The widths of these Gaussians, w_x , w_y , w_z and w_p , need to be tuned so that on the one hand fluctuations due to the discrete nature of the test particle picture are smoothed out, but on the other hand the physical structure of the distribution function f_s remains preserved [87]. The statistical fluctuations are of the order of $(\tilde{N}w_p^3w_xw_yw_z/N)^{-1/2}$, so that the first condition is equivalent to

$$w_p w_r \gg (N/\tilde{N})^{1/3}, \quad (8.31)$$

where we introduced $w_r = (w_x w_y w_z)^{1/3}$, the geometric average of the spatial widths. The second condition implies $w_i \ll R_i$ and $w_p \ll \tilde{k}_F$, where the Fermi momentum

and the Thomas-Fermi radii were defined in (8.13). Additionally at low temperature it is crucial to resolve the rapid change of the distribution function around the Fermi surface, such that

$$w_p \ll \tilde{k}_F(T/\tilde{T}_F) \quad \text{and} \quad w_i \ll R_i(T/\tilde{T}_F). \quad (8.32)$$

Note that the smearing width in momentum space is isotropic, while in position space the smearing width can be different depending on the spatial direction, if the corresponding trap frequencies are unequal. This is a direct consequence of the isotropy of the momentum space distribution (8.17) that was discussed in section 8.1. Since the Thomas-Fermi radii are inversely proportional to the corresponding trap frequencies it is sensible to choose $w_i = w_r \omega_0 / \omega_i$ for the spatial widths. Furthermore Eq. (8.32) together with the definition (8.13) imply $w_p = m w_r$. Hence all four smearing widths can be reduced to only one free parameter. At very low temperatures the margin given by the conditions (8.31) and (8.32) becomes so narrow that it is impossible to find smearing widths satisfying both conditions, without having to significantly increase the number of test particles. This limits the applicability of this setup to temperatures above approximately $0.2\tilde{T}_F$ for $\tilde{N}/N = 10$. Moreover, at very low temperatures the system undergoes a phase transition into a superfluid state. This algorithm does not include the relevant degrees of freedom of the superfluid Fermi gas and is only applicable in the normal phase.

The main numerical challenge is to efficiently evaluate collisions between the test particles. The total number of pairs of opposite spin is $\tilde{N}^2/4$, which is an unfavourable scaling given that we want to use large particle numbers and a high test particle to particle ratio. In this work we develop a more efficient method than to check all possible test particle pairs. The key observation is that since the cross section is decreasing with increasing relative momentum it can never exceed $\tilde{\sigma}_{\max} = 4\pi a^2 N/\tilde{N}$ and consequently the maximal distance two colliding test particles can have is $d_{\max} = 2a\sqrt{N/\tilde{N}}$. Having this in mind we superpose a cubic grid with cell size d_{\max} on the continuous space. The grid has finite extent which can be set by demanding that a certain proportion, for instance at least 95%, of the test particles are within the grid. For a cigar shaped trap the grid must have larger extent in the axial direction. At the end of each time step we move systematically through all grid cells starting in one of the corners and note all possible collision partners that fulfill the classical scattering conditions. To make sure that we do not miss collisions due to boundary effects, for each particle we check not only all opposite spin particles in the same grid cell, but also in all neighbouring cells (the ones sharing a face, an edge or a vertex with the given cell). This ensures that all particles in a sphere of radius d_{\max} around a given particle are definitely accounted for. This makes a total of $3^3 = 27$ cells for each particle, however to avoid double counting we only need to evaluate cells in the positive direction.

A small systematic error source remains with this setup. If the relative velocity of

two particles is large they can be in non-neighbouring cells at the beginning and at the end of a time step, although in the course of the time step they come within each other's allowed collision range. Such a possible collision will then not be accounted for. However this systematic error can be minimised by choosing the time step to be sufficiently small and also by choosing the cell size to be larger than d_{max} . Also note that for large relative velocities the cross section is small and collisions between very fast particles are rare events.

After having searched the entire grid for classically allowed collision pairs we proceed to choose which collisions will indeed take place. To do so we consecutively select random pairs from the list. We then propagate both particles to the point of their closest approach, let them scatter (the exact setup for determining the new positions and momenta after scattering is described below) and then propagate them back to the original time. To account for quantum statistics we then calculate the Pauli blocking factors using the new distributions $f'_s = f_s(\mathbf{r}', \mathbf{p}')$. The continuous distributions are obtained by replacing the δ -functions in (8.26) according to (8.30),

$$f_s(\mathbf{r}', \mathbf{p}') = \frac{N_s}{\tilde{N}_s} \sum_{i=1}^{\tilde{N}_s} (2\pi)^3 \frac{e^{-(\mathbf{p}' - \mathbf{p}_i)^2/w_p^2}}{(\sqrt{\pi}w_p)^3} \frac{e^{-(x' - x_i)^2/w_x^2}}{\sqrt{\pi}w_x} \frac{e^{-(y' - y_i)^2/w_y^2}}{\sqrt{\pi}w_y} \frac{e^{-(z' - z_i)^2/w_z^2}}{\sqrt{\pi}w_z}. \quad (8.33)$$

If we obtain a value $f'_s > 1$ from the summation we set $f'_s = 1$. The probability that the collision is accepted is then given by $(1 - f'_s)(1 - f'_{\bar{s}})$. Regardless if a collision is accepted or rejected neither of the particles concerned is allowed to collide again with another particle during the present time step. If the collision is accepted we keep the new positions and momenta. If the collision is rejected we return to the values before the collision. This procedure is repeated until all possible pairs have been evaluated.

To calculate the new coordinates and momenta of the two particles after a collision we use the following procedure. As collisions are local, disregard for the moment the external potential and go to the centre of mass frame of the two particles. Motivated by the analogue of classical scattering we wish to conserve the total momentum, the total energy and the total angular momentum of the system during the collision. Conservation of the total momentum $\mathbf{p} = \mathbf{p}_s + \mathbf{p}_{\bar{s}}$ and the total energy $E = E_{\text{kin}} = (p_s^2 + p_{\bar{s}}^2)/2m$ together imply the conservation of the modulus of the relative momentum $p_{\text{rel}} = |\mathbf{p}_s - \mathbf{p}_{\bar{s}}|$, since $p^2 + p_{\text{rel}}^2 = 2(p_s^2 + p_{\bar{s}}^2) = 4mE$. The direction of the relative momentum vector can change during the collision. Conservation of the angular momentum $\mathbf{L} = \mathbf{r}_{\text{rel}} \times \mathbf{p}_{\text{rel}}$ implies that the relative momentum vector can only be rotated in the plane spanned by \mathbf{r}_{rel} and \mathbf{p}_{rel} , or in other words \mathbf{p}_{rel} must be rotated around the axis defined by the vector \mathbf{L} . The angle of this rotation is the only degree of freedom of the collision and is determined at random. To conserve the modulus of the angular momentum, the relative position vector \mathbf{r}_{rel} must be rotated by the same angle as \mathbf{p}_{rel} . The relative distance of the particles $|\mathbf{r}_{\text{rel}}|$ still remains unchanged. It is easy to see that the angular momen-

tum and the relative position vector cannot be simultaneously conserved. We chose a setup in which momentum, energy and angular momentum are conserved at the cost of a rotation of the relative position vector of the particles. From the new values \mathbf{p}'_{rel} and \mathbf{r}'_{rel} the new values of the momenta and positions of the individual particles can be recovered using total momentum conservation and the centre of mass coordinates respectively.

So far we have ignored the external potential, which is justified since the collisions are local and hence the presence of an external potential should not play a role for the calculation of the new coordinates and momenta. In practice however, in our setup the two colliding particles are not exactly at the same position and their relative position changes after a successful collision. Thus potential energy is not conserved and energy conservation is not exact during a collision if the potential is non-isotropic. On average of course, energy conservation still holds since in a many-particle system these small effects will cancel each other out. It is possible to preserve energy conservation exactly by employing a different setup, for instance as in [87]. In this reference, the relative position stays fixed during a collision and the relative momentum vector is rotated by a random angle in space (such a rotation has two degrees of freedom). As a direct consequence of the unrestricted rotation this setup violates angular momentum conservation. On the other hand it is arguable that angular momentum is not conserved during the propagation step either if the external potential is non-isotropic. As in this work we will always consider either isotropic or axially symmetric potentials, either the total angular momentum or its axial component L_z are conserved.

To study the impact of the collisional setup on the outcome of the simulation we have implemented the setup from [87] in addition to our setup described above, and confirmed that they generate the same results for both equilibrium and non-equilibrium systems. We compared the equilibrium collision rates as well as the time evolutions of the centre of mass coordinates in response to a perturbation. The differences between the two setups were found to be smaller than the statistical fluctuations. It is therefore well-grounded to say that the two setups are equivalent on a macroscopical scale and we have the freedom to choose whichever option appears more convenient. We adopt the angular momentum conserving setup, not only because of this property, but also since the setup from [87] has a small technical disadvantage. Since the new direction of the relative momentum vector is chosen uniformly on a sphere, in many cases the particles are found to approach each other again after a successful collision. This implies that in the following time step they are likely to undergo another collision. To avoid this overcounting of collisions one needs to implement an additional routine that prevents particles from colliding with each other repeatedly within short time intervals. In other words the molecular chaos assumption does not hold with the setup from [87] and needs to be enforced artificially. In our setup repeated scattering is so rare that this effect can be neglected.

Since the picture of colliding point-like particles with well-defined positions and momenta is a classical interpretation of a quantum mechanical scattering process, it is unsurprising that there is some ambiguity in the implementation of the collisional setup. In the semiclassical particle picture each collision has 12 degrees of freedom: three position and three momentum components for each of the two particles, or equivalently three components of the total and relative positions and momenta. In quantum mechanics we consider wave packets rather than particles and concepts like particle position or momentum are not well-defined. Instead the system is described by operators which, depending on the symmetries of the system, commute with the Hamiltonian and define quantum numbers corresponding to conserved quantities. The concept of a trajectory does not exist, as a particle is not localised in phase space but rather smeared out over a certain phase space volume in accordance with Heisenberg's uncertainty principle. It is therefore not necessary to preserve for instance the exact positions of the two atoms during a collision. In the presence of an axially symmetric external potential for instance, the only conserved quantities are the total energy and L_z .

From this quantum mechanical picture we can develop the following general collisional setup. To preserve macroscopical averages we keep the centre of mass coordinates and momentum fixed and work with the six degrees of freedom for the relative momentum and position. Based on the idea of a delocalised particle pair, we assume that the relative phase space coordinates of the particles are distributed according to a Gaussian. We then choose the new relative position and momentum randomly according to the Gaussian probability distribution with the additional constraints given by the symmetries of the problem. Energy and L_z conservation for instance reduce the problem by two degrees of freedom. If energy and total angular momentum are conserved the problem is reduced by four degrees of freedom and so on. As the macroscopical outcome was found to be insensitive towards the details of the microscopical setup we do not explore this general collisional setup in the present work, but use the simpler method described above.

8.4 Tests and optimal parameters

How accurately the numerical setup represents the physical picture depends crucially on the values of the simulation parameters, in particular \tilde{N}/N , the time step Δt and the smearing widths w_r and w_p . In all our simulations we use $\tilde{N}/N = 10$, which is sufficient for temperatures $T \geq 0.2\tilde{T}_F$. The optimal value of Δt depends on the physical parameters of the system. Obvious requirements are that the time step must be smaller than the typical time between two collisions and that the average distance travelled during a time step must be much smaller than the diameter of the cross section, $\langle v_{\text{rel}} \rangle \Delta t \ll \sqrt{\langle \tilde{\sigma} \rangle / \pi}$. Another constraint is that the time step must be smaller than the

half-period with respect to the largest trap frequency, $\Delta t < \pi/\omega_{\max}$, but for the aspect ratios considered in this study this condition is much weaker than the other ones. There is no lower bound on the time step, however the simulation slows down with decreasing Δt . All tests described below were performed for systems with $N = 10000$ atoms.

We performed several tests of the simulation to ensure that it accurately captures the relevant physics. As mentioned above, we checked that total energy conservation is indeed satisfied for the whole system to a high accuracy. To obtain the correct dynamical properties, for instance the damping time of excitation modes later on, we need to ensure that the equilibrium collision rate observed in the simulation corresponds to the correct theoretical value. The number of collisions in a given time interval can be very easily obtained from the simulation, simply by counting all test particle collisions and then multiplying by the ratio (N/\tilde{N}) . The theoretical value for the collision rate γ in the presence of Pauli blocking is given by the following integral,

$$\gamma_{\text{block}} = \int d^3r \int \frac{d^3p_s}{(2\pi)^3} \frac{d^3p_{\bar{s}}}{(2\pi)^3} \int d\Omega \frac{d\sigma}{d\Omega} |\mathbf{p}_s - \mathbf{p}_{\bar{s}}| f_s f_{\bar{s}} (1 - f'_s)(1 - f'_{\bar{s}}). \quad (8.34)$$

After inserting the Fermi-Dirac distribution this integral can be calculated numerically [87]. Our numerical setup also provides the powerful tool to artificially switch off Pauli blocking. This allows to separately check for errors related to the general numerical setup and the calculation of the Pauli blocking factors. Without Pauli blocking the integral is simpler and can be solved analytically for the Maxwell-Boltzmann distribution,

$$\gamma_{\text{noblock}} = \int d^3r \int \frac{d^3p_s}{(2\pi)^3} \frac{d^3p_{\bar{s}}}{(2\pi)^3} \int d\Omega \frac{d\sigma}{d\Omega} |\mathbf{p}_s - \mathbf{p}_{\bar{s}}| f_s f_{\bar{s}} \quad (8.35)$$

$$= N_{\uparrow} N_{\downarrow} \frac{2\omega_0^3}{\pi T^2} \left(1 + \frac{1}{ma^2T} e^{\frac{1}{ma^2T}} \text{Ei} \left(-\frac{1}{ma^2T} \right) \right), \quad (8.36)$$

where $\text{Ei}(x) = \int_{-\infty}^x (e^t/t) dt$ is the exponential integral. Furthermore we can obtain the theoretical prediction for the Pauli blocking probability by solving the integral (8.35) for the Fermi-Dirac distribution. The probability p_{Pauli} that two classically colliding fermions will indeed scatter is then be given by the ratio of γ_{block} to this integral.

To find the optimal value for Δt for each system we measure the collision rate in the absence of Pauli blocking for decreasing values of the time step and compare it to the theoretical prediction. The time step is small enough when we reach good agreement. It is important to switch off Pauli blocking for the tuning of the time step, as in the presence of Pauli blocking the collision rate is sensitive to the values of the smearing widths, which can obscure inaccuracies due to a time step that is too large. After having found the optimal time step we check that repeated collisions of the same particle pair are rare. This has always been found to be the case with our collisional setup. We then

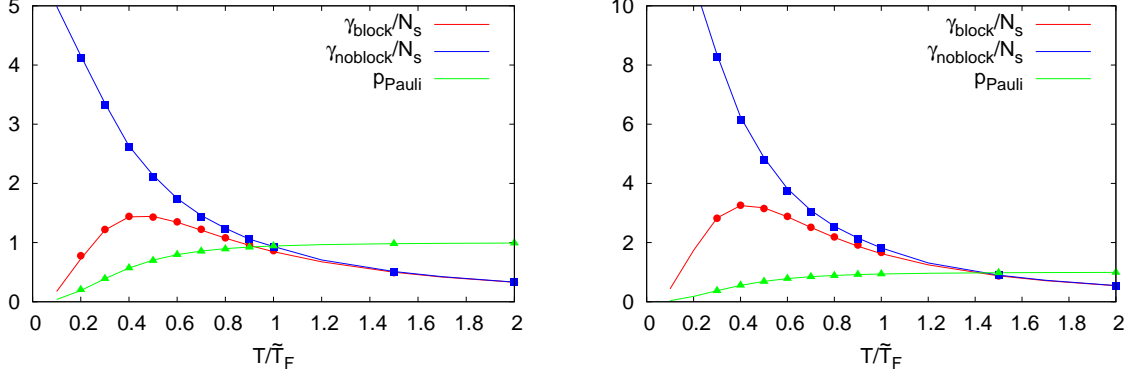


Figure 8.1: The equilibrium collision rates per particle with and without Pauli blocking, as well as the Pauli probability for a successful scattering versus temperature for $|\tilde{k}_F a| = 1$ (left) and $|\tilde{k}_F a| = 2$ (right). The lines correspond to the theoretical prediction and the symbols to the values obtained with the simulation.

use this optimal value for Δt to establish the optimal values of the smearing widths. We first identify the allowed interval for w_p and w_r given by the conditions (8.31) and (8.32) and perform the same collision rate matching as described above, this time with Pauli blocking switched on. We find that the optimal widths lie between $w_r = w_p/m = 1.0l_{\text{ho}}$ for the lowest and $w_r = w_p/m = 2.0l_{\text{ho}}$ for the highest temperatures used in our analysis, where $l_{\text{ho}} = 1/\sqrt{m\omega_0}$ is the natural harmonic oscillator length unit.

The measured collision rates for the optimal choice of parameters with and without Pauli blocking together with the theoretical predictions are shown in Fig. 8.1. For sufficiently high temperatures the agreement is very good. At very low temperatures it becomes increasingly difficult to resolve the conditions (8.31) and (8.32) for the Gaussian smearing widths simultaneously. For larger values of the scattering length this problem gets worse since larger cross sections can lead to collisions between test particles which are further apart [87] and therefore the continuous distribution function needs to be resolved accurately over larger scales.

Another important test is to check that the system thermalises to the correct equilibrium energy distribution, independently of the initial distribution. In the presence of Pauli blocking the energy is distributed according to the Fermi-Dirac distribution (8.8), as shown in section 8.1. Without Pauli blocking the particles will be distributed according to the Maxwell-Boltzmann distribution (8.20). Figures 8.2 and 8.3 show the results of this test for a low temperature system with $|\tilde{k}_F a| = 1$ and isotropic trap frequencies. The parameter values for the time step and the smearing widths are optimal. We performed two tests of the thermalisation. First we initialised the system according to the Fermi-Dirac distribution for $T = 0.2\tilde{T}_F$ (Fig. 8.2) and ran the simulation without Pauli blocking. After a short time the system thermalised according to the Maxwell-Boltzmann distribution for $T = 0.31\tilde{T}_F$. Note that the temperatures of the two distributions are not necessarily equal, since the equipartition theorem does

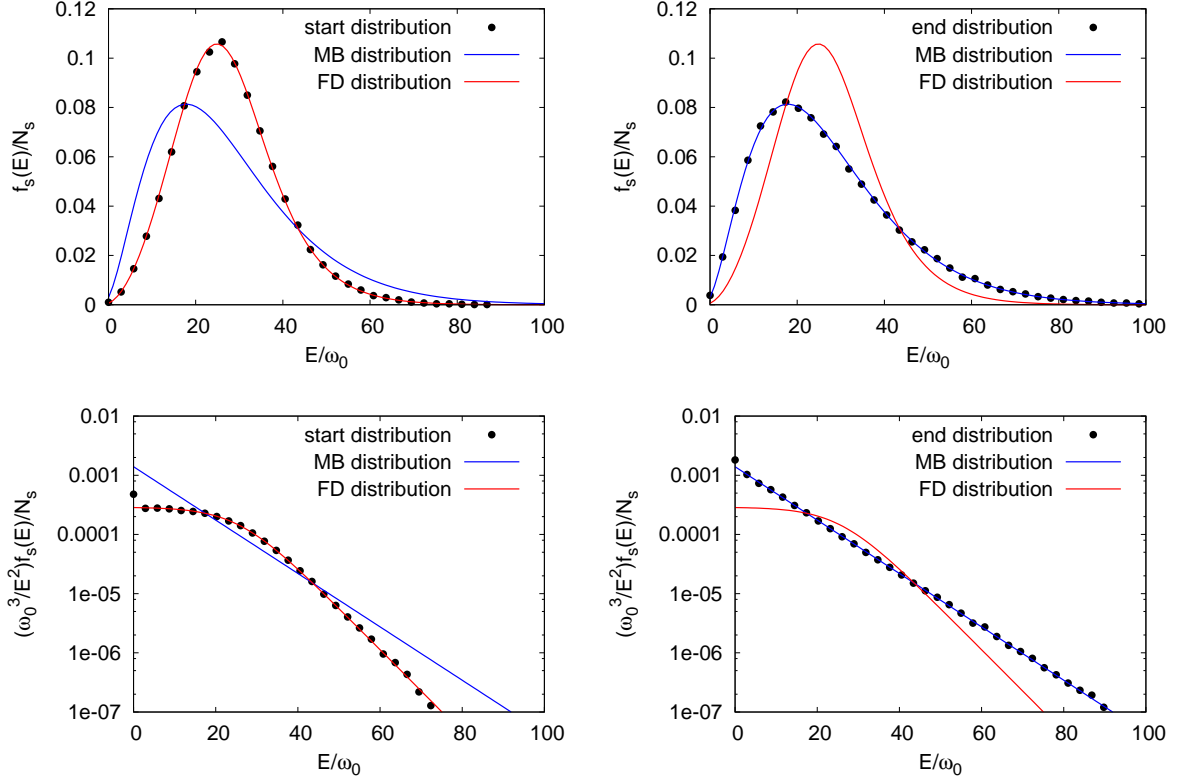


Figure 8.2: The equilibrium energy distributions without Pauli blocking. The top panel shows the energy distributions on a linear scale, the bottom panel shows the energy distributions scaled by ω_0^3/E^2 on a logarithmic scale. The start distribution (left) is Fermi-Dirac and the end distribution (right) is Maxwell-Boltzmann as expected.

not hold for the Fermi-Dirac distribution. For the Maxwell-Boltzmann distribution we have

$$\langle E \rangle = 2\langle E_{\text{kin}} \rangle = 3TN, \quad (8.37)$$

while for the Fermi-Dirac distribution we have

$$\langle E \rangle = \int_0^\infty \frac{(E^3/\omega_0^3)dE}{1 + e^{(E-\mu_s)/T}} = -\frac{6T^4}{\omega_0^3} \text{Li}_4(-e^{\mu_s/T}), \quad (8.38)$$

where $\text{Li}_n(z) = \sum_{k=1}^\infty \frac{z^k}{k^n}$ is the polylogarithm. When changing from one distribution to the other the average energy of the system remains conserved and hence the temperature of the new equilibrium state is different. Figure 8.3 shows the corresponding results for the reverse situation: the initial distribution is Maxwell-Boltzmann with $T = 0.31\tilde{T}_F$ and Pauli blocking is switched on. It is clearly visible from both figures that the correct equilibrium distribution is always attained at the end of the simulation. This agreement improves further at higher temperatures.

Collective excitations emerge when a many-particle system is perturbed away from equilibrium. Here we will discuss three different excitation modes, the sloshing mode

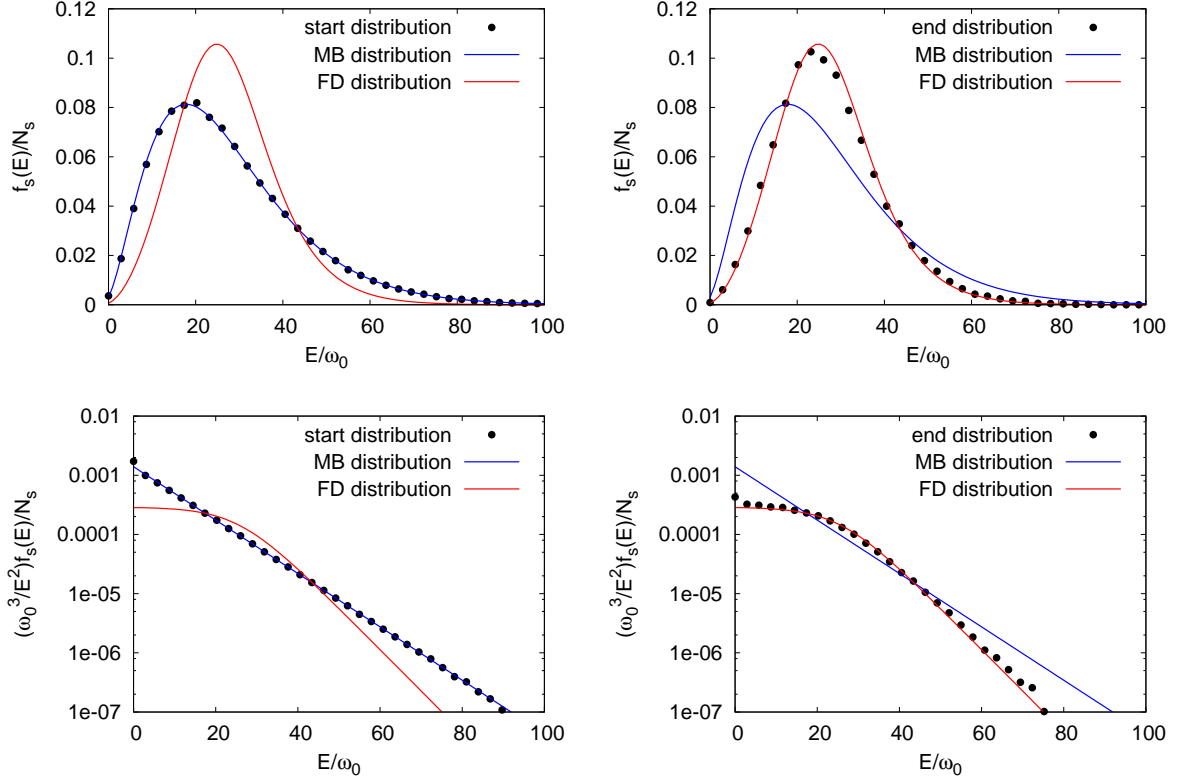


Figure 8.3: The equilibrium energy distributions with Pauli blocking. The top panel shows the energy distributions on a linear scale, the bottom panel shows the energy distributions scaled by ω_0^3/E^2 on a logarithmic scale. The start distribution (left) is Maxwell-Boltzmann and the end distribution (right) is Fermi-Dirac as expected.

(also known as dipole or Kohn mode), the breathing mode (monopole mode) and the quadrupole mode. We will confirm that the simulation gives the correct frequencies and damping properties of these modes. The following tests were performed for a spherical trap $\omega_x = \omega_y = \omega_z = \omega_0$.

The sloshing mode is excited by a small displacement of the centre of mass from its equilibrium position, or equivalently by a short-lived force represented by an additional linear term in the potential. It is easy to see that the position and momentum of the centre of mass of the system must obey the same equations of motion as the individual particles. As a collision does not change the centre of mass coordinates or momentum either, $\langle \mathbf{r} \rangle$ and $\langle \mathbf{p} \rangle$ must obey the harmonic oscillator equations. Hence the time evolution of each of the three centre of mass coordinates $\langle r_i \rangle$ is an undamped oscillation with the corresponding harmonic oscillator frequency ω_i . Figure 8.4 shows such an oscillation for a system at $|\tilde{k}_F a| = 1$ and $T = 0.2\tilde{T}_F$.

The breathing mode can be excited by compressing or expanding the cloud. In a spherical trap this yields an undamped oscillation of $\langle r^2 \rangle$ with frequency $2\omega_0$ around its equilibrium value. To see this consider the averages of the kinetic and the potential

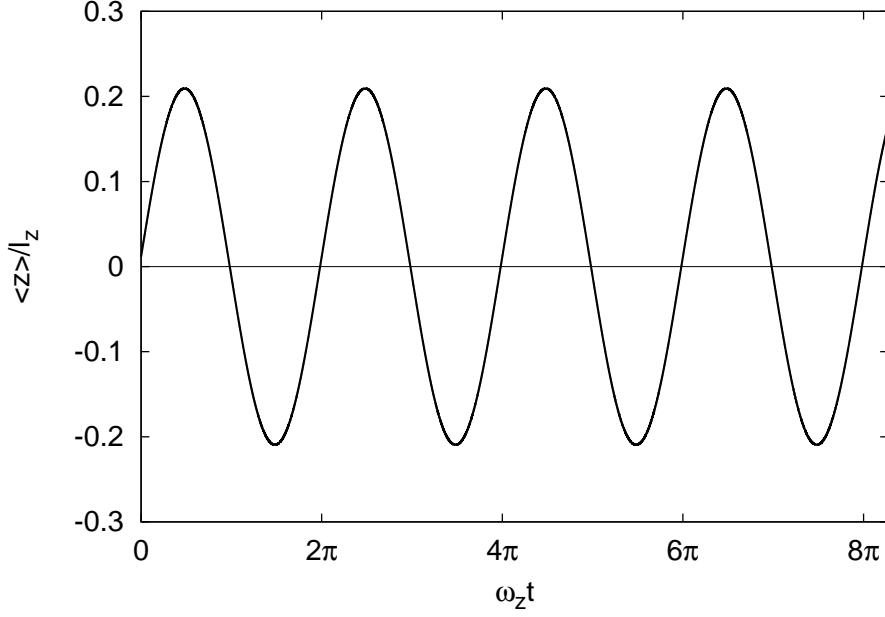


Figure 8.4: Simulation of the equilibrium sloshing mode $\langle z \rangle / l_z$, where $l_z = 1/\sqrt{m\omega_z}$. In agreement with the theory the mode is undamped and the oscillation frequency equals ω_z .

energy $\langle E_{\text{kin}} \rangle = \langle p^2 \rangle / 2m$ and $\langle E_{\text{pot}} \rangle = m\omega_0^2 \langle r^2 \rangle / 2$. Inserting the harmonic oscillator equations of motion $\dot{\mathbf{r}} = \mathbf{p}/m$ and $\dot{\mathbf{p}} = -m\omega_0^2 \mathbf{r}$ we obtain

$$\frac{d}{dt}(\langle E_{\text{kin}} \rangle - \langle E_{\text{pot}} \rangle) = -2\omega_0^2 \langle \mathbf{r} \cdot \mathbf{p} \rangle, \quad (8.39)$$

$$\frac{d}{dt} \langle \mathbf{r} \cdot \mathbf{p} \rangle = 2(\langle E_{\text{kin}} \rangle - \langle E_{\text{pot}} \rangle). \quad (8.40)$$

These are again the equations for an undamped harmonic oscillator, this time with the frequency $2\omega_0$. Let us now consider the effect of collisions. Conservation of the total momentum and the modulus of the relative momentum of the two colliding particles implies that $\langle E_{\text{kin}} \rangle$ is unchanged during a collision. By the same reasoning conservation of the centre of mass coordinates and the relative distance of the two particles implies that $\langle E_{\text{pot}} \rangle$ is unchanged for an isotropic potential. Since the two particles are approximately at the same point in space when they collide the term $\langle \mathbf{r} \cdot \mathbf{p} \rangle$ also stays approximately unchanged due to momentum conservation. Hence the term $\langle E_{\text{kin}} \rangle - \langle E_{\text{pot}} \rangle$ oscillates around zero with frequency $2\omega_0$ and this oscillation is undamped. This implies that after a small perturbation $\langle r^2 \rangle$ will perform an undamped oscillation with frequency $2\omega_0$ around its equilibrium value $\langle r^2 \rangle_{\text{eq}} = \langle p^2 \rangle / (m^2 \omega_0^2)$. Figure 8.5 illustrates the breathing mode for a system with $|\tilde{k}_F a| = 1$ and $T = 0.2\tilde{T}_F$.

By perturbing the system via a short-lived small increase in one or several of the trap frequencies we can excite the quadrupole mode. This is equivalent to a small momentum shift that equals the gradient of the perturbation potential [87]. We excite

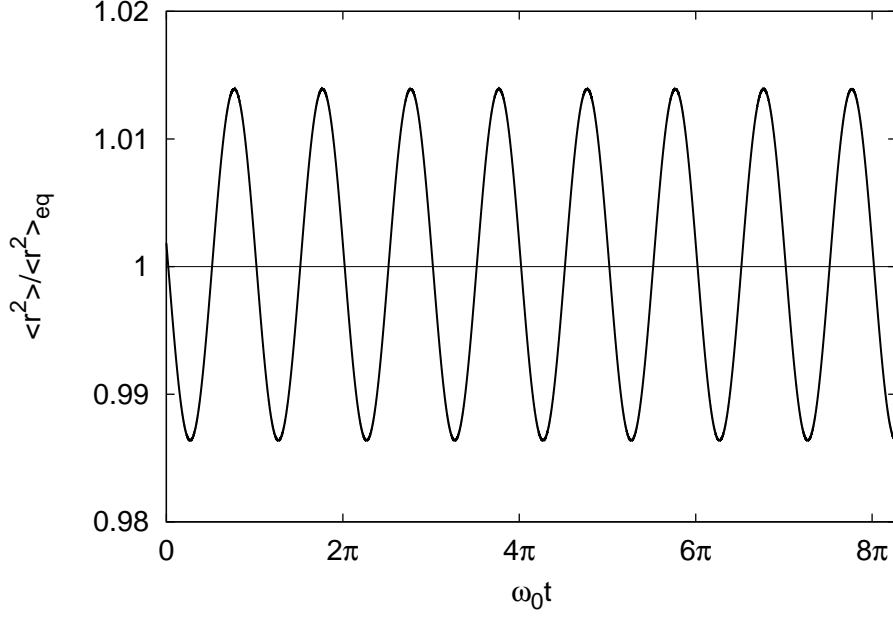


Figure 8.5: Simulation of the normalised equilibrium breathing mode $\langle r^2 \rangle / \langle r^2 \rangle_{\text{eq}}$. In agreement with the theory the mode is undamped and the oscillation frequency equals $2\omega_z$.

the quadrupole mode $Q(t) = \langle x^2 \rangle - \langle y^2 \rangle$ by applying the perturbation $\Delta p_x = -cx$ and $\Delta p_y = cy$ with $c = 0.2m\omega_0$ in the same way as in [87]. Unlike the sloshing and the breathing mode this mode is damped. The frequency of the quadrupole mode at high temperatures approaches the ideal gas value $2\omega_0$, while at low temperatures it is closer to the hydrodynamic frequency $\sqrt{2}\omega_0$ [87]. Figure 8.6 shows the quadrupole mode for $|\tilde{k}_F a| = 1$ in the high and in the low temperature regime. In both cases the damping of the mode is clearly visible. The damping is stronger at lower temperatures when collisions are more frequent. The frequency of the oscillation can be extracted from the corresponding Fourier transform $Q(\omega) = \int_0^\infty dt Q(t) e^{i\omega t}$ and is in agreement with the theoretical prediction.

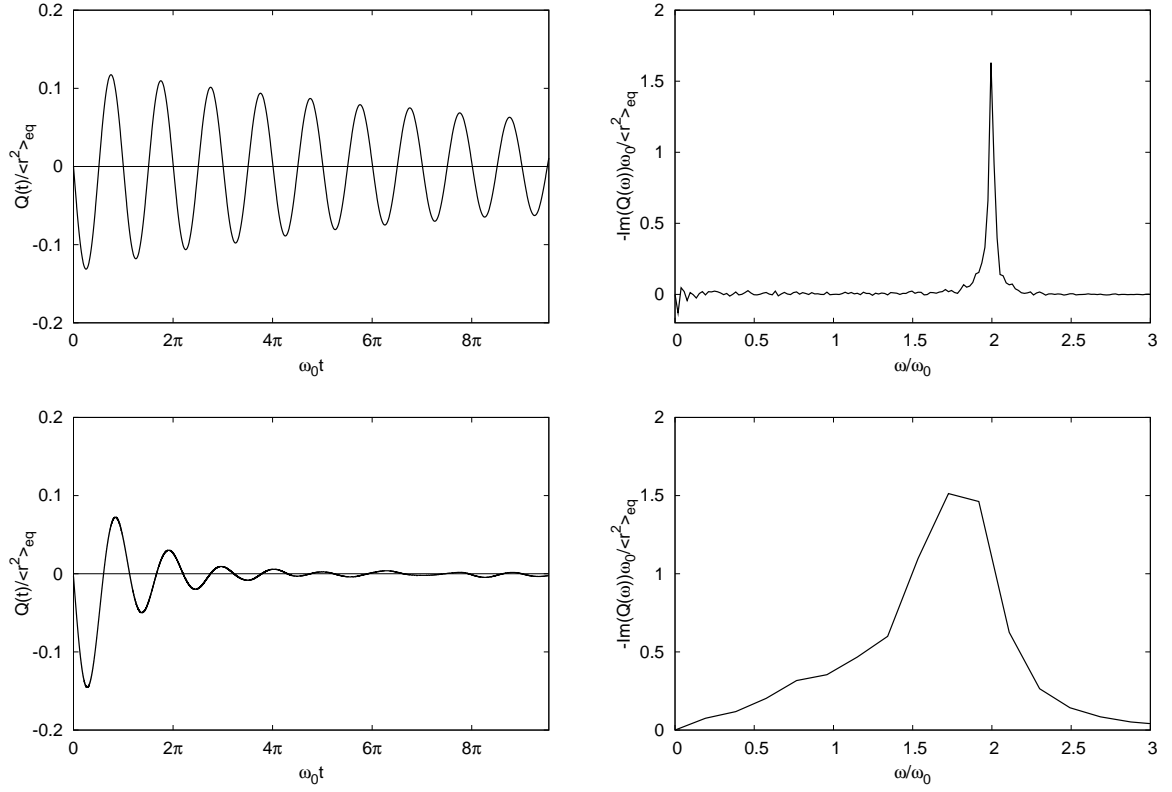


Figure 8.6: Left: Simulation of the normalised equilibrium quadrupole mode $Q(t)/\langle r^2 \rangle_{\text{eq}}$ at high temperature $T = 2\tilde{T}_F$ (top panel) and at low temperature $T = 0.4\tilde{T}_F$ (bottom panel). Right: The imaginary part of the corresponding Fourier transforms of the numerical data gives information about the oscillation frequency.

Collision of two fermionic clouds

We will now apply the numerical setup introduced in the previous chapter to study the collision of two fermionic clouds with opposite spin polarisation in a cigar shaped harmonic trap. This research is motivated by the recent experiments of A. Sommer et al. [37, 40]. Our approach is complementary to the experimental one given our ability to measure experimentally inaccessible observables such as the local collision rate. A recent theoretical work using a hydrodynamic approach based on a many-body equation of state addresses similar issues [90].

The initial distributions are created by sampling a Fermi-Dirac distribution given by Eq. (8.2). Then each spin distribution is displaced in opposite directions along the z -axis by $d_0/2$. In the subsequent time evolution, the clouds begin to move towards the centre under the harmonic trapping force resulting in a collision between them. After a sufficiently long time the centre of mass energy $2 \cdot \frac{1}{2} m \omega_z^2 (d_0/2)^2$ will be transformed completely into the internal energy of the gas and a new equilibrium state will be reached, characterised by a new Fermi-Dirac distribution with temperature T_{final} (and a chemical potential μ_{final}). Note that T_{final} is a function of only the atom number, the initial temperature T_{init} and the initial cloud separation d_0 and can be calculated exactly from these values using energy conservation. In the following whenever we refer to the final temperature of the system we use the theoretical value obtained from the initial system properties.

Simulations were carried out for a range of initial cloud temperatures $0.2 \leq T_{\text{init}}/\tilde{T}_F \leq 10$, interaction strength $0.5 \leq |\tilde{k}_F a| \leq 10$, and initial distances between the centres of mass of the two clouds $0.4\sigma_z \leq d_0 \leq 16\sigma_z$, where $\sigma_z = \sqrt{T_{\text{init}}/m\omega_z^2}$. All numerical data presented in this chapter was obtained for $N = 10000$, $\tilde{N} = 10N$ and $\omega_x/\omega_z = \omega_y/\omega_z = 100$.

9.1 Qualitative Behaviour

The behaviour of the clouds during the simulation can be studied by measuring the distance between their centres of mass $d(t) = \langle z_{\uparrow} - z_{\downarrow} \rangle(t)$. As in [37], we find that before they come to rest at thermal equilibrium, the motion of the clouds exhibits three typical behaviours, see Fig. 9.1.

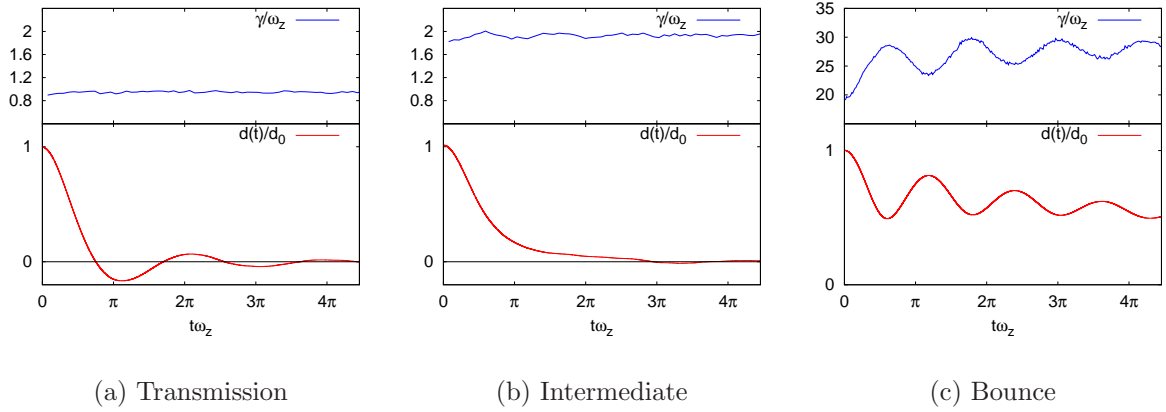


Figure 9.1: Bottom panel: The normalised dipole mode $d(t)/d_0$ for the three different behaviours: transmission (a), intermediate (b) and bounce (c). Top panel: the corresponding collision rate per particle γ/ω_z measured in the region with $|z| \leq \sigma_z/2$ around the trap centre, where $\sigma_z = \sqrt{T_{\text{init}}/m\omega_z^2}$.

Transmission: For sufficiently high temperatures and small interactions, the clouds oscillate through each other (i.e. $d(t)$ crosses zero at short times) with decreasing amplitude, see Fig. 9.1(a).

Bounce: At low temperatures and strong interactions the clouds bounce off each other several times (in each bounce the motion of the centre of mass of each cloud is reversed at short times and without $d(t)$ crossing zero) before a longer period of slow approach, see Fig. 9.1(c).

Intermediate: Between the transmission and bounce regimes there is a range of temperatures and interactions where the slow approach behaviour is visible from the start and neither bounces nor transmissions are observed, see Fig. 9.1(b).

The dependence of the behaviour on temperature and interactions is related to the variation in collision rate γ in the overlap region between the two clouds. As the collision rate decreases, the system behaviour changes from the bounce regime, to intermediate and finally to the transmission regime. From the top panel of Fig. 9.1 we see that, in the bounce regime, the oscillations in the collision rate integrated over a volume in the overlap region follow closely the oscillations of $d(t)$, whereas no such variation is apparent in the transmission regime. In addition, we can compare the collision rate with the typical timescale for macroscopic motion (ω_z^{-1}). We see that the gas is strongly hydrodynamic in the bounce regime ($\omega_z/\gamma \ll 1$) and becoming collisionless in the transmission regime ($\omega_z/\gamma \sim 1$).

Note that no artificial repulsion between the atoms was included in the numerical setup. The repulsive behaviour of the centres of mass of the clouds in the bounce regime arises naturally from the purely attractive interaction between the individual

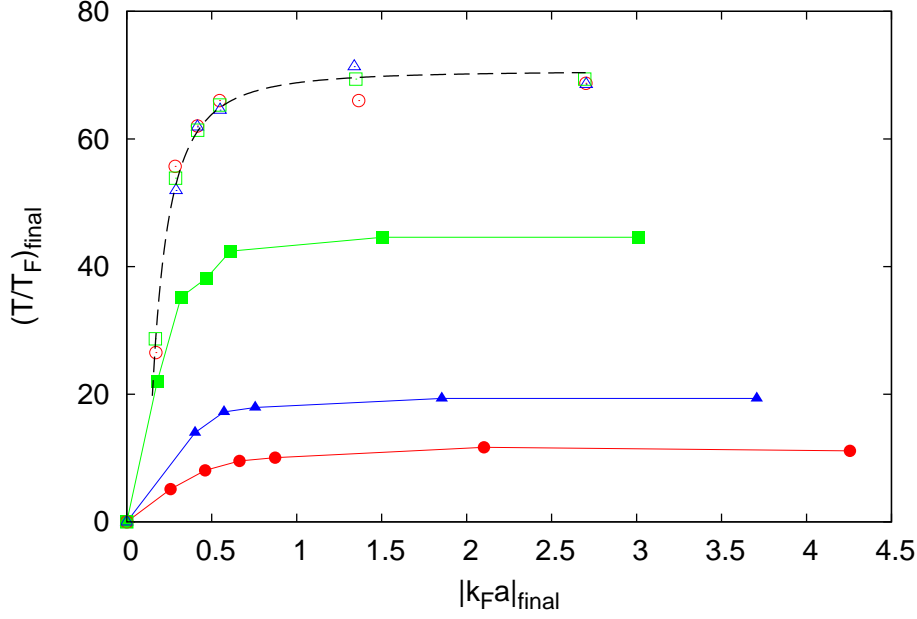


Figure 9.2: The transition between bounce and intermediate regimes (filled symbols, lines to guide the eye) and between intermediate and transmission regimes (empty symbols). Red circles correspond to $d_0 = 43.1l_z$, blue triangles to $d_0 = 64.6l_z$ and green squares to $d_0 = 129.3l_z$, where $l_z = 1/\sqrt{m\omega_z}$. It is clearly visible that the intermediate-transmission transition is independent of d_0 . The dashed line corresponds to constant relaxation time $1/\tau_{\text{dip}} = 1.83\omega_z$.

particles. We have also seen that the bounce can be understood purely in terms of semiclassical collisions, without the need for mean fields or other more complicated many-body effects. In particular our approach predicts that all quantities considered here depend only on the square of the scattering length and not on its sign, a fact that was also observed in [37]. In contrast, in [90] the bounce is understood from the equation of state of the so-called “repulsive” branch and therefore, according to that work, would in principle exhibit different behaviour on opposite sides of the resonance.

9.2 Transitions between regimes

Figure 9.2 shows the transitions between the three regimes of behaviour in the $(T/T_F)_{\text{final}}$, $|k_F a|_{\text{final}}$ plane for different values of d_0 in units $l_z = 1/\sqrt{m\omega_z}$. Remember that as the density is a function of the temperature, T_F and k_F defined in (8.12) change during the simulation and hence $k_F a$ varies during the evolution. The quantities given here are equilibrium values for $t \rightarrow \infty$.

The transition between transmission and intermediate regimes is defined as $d(t)$ reaching but not crossing zero at short times. It is clearly visible from Fig. 9.2 that this transition is independent of the initial separation d_0 and hence can be understood entirely from the final equilibrium properties of the system. More precisely, it can be

understood as a consequence of the change in the relaxation time τ_{dip} of the spin dipole mode of the $d_0 = 0$ system, which is closely related to the collision rate per atom. For sufficiently high temperatures $T \gtrsim \tilde{T}_F$ the relaxation time can be calculated from the Maxwell-Boltzmann distribution and equals

$$\frac{1}{\tau_{\text{dip}}} = \frac{2N}{3\pi T^2} \omega_0^3 f\left(\frac{1}{ma^2 T}\right), \quad (9.1)$$

where $f(y) = 1 - y + y^2 e^y \Gamma(0, y)$, as was shown in [91]. The incomplete Γ -function is hereby defined as $\Gamma(0, y) = -\text{Ei}(-y) = \int_y^\infty (e^{-t}/t) dt$. By comparison with (8.36) we can see that the relaxation time is closely related to the equilibrium collision rate for the Maxwell-Boltzmann distribution. For sufficiently low collision rate ($\omega_z \tau_{\text{dip}} \gg 1$), the gas can be said to be collisionless and therefore the clouds undergo independent oscillations without interacting strongly with each other. In the transmission regime $d(t)$ is simply the solution of the classical damped harmonic oscillator equations [91],

$$d(t) = e^{-t/2\tau_{\text{dip}}} (A \sin(\omega t) + B \cos(\omega t)), \quad (9.2)$$

where A and B are given by the initial conditions and the oscillation frequency equals $\omega = \sqrt{\omega_z^2 - 1/(2\tau_{\text{dip}})^2}$. Hence the oscillation frequency is related to the damping. When $1/\tau_{\text{dip}} \rightarrow 0$ the frequency becomes exactly ω_z and there is no damping (non-interacting gas). At finite τ_{dip} the frequency is smaller than ω_z . For $1/\tau_{\text{dip}} > 2\omega_z$ the dipole mode is overdamped [91, 92] as ω becomes ill-defined. To compare with the simulations, we can calculate the value of τ_{dip} for the various points lying on the curve separating the transmission and intermediate regimes of Fig. 9.2 using Eq. (9.1). We find that they lie on the curve of constant $1/\tau_{\text{dip}} = 1.83(1)\omega_z$.

The transition between the intermediate and the bounce regime is defined to occur when the first bounce ceases to reverse the motion of the clouds, or in other words when $d(t)$ ceases to have a minimum and becomes a monotonically decreasing function of t . This transition depends on d_0 . In the bounce regime we typically see an initial strong collision followed by oscillations of $d(t)$ which eventually die out as $d(t) \rightarrow 0$. This oscillatory behaviour continues into the intermediate regime. As the damped harmonic oscillator can never produce such a bounce solution, this regime must be the consequence of a different mechanism. In the following section we will relate it to a non-linear coupling between the spin dipole mode and the breathing mode.

9.3 Coupling between excitation modes

We have already discussed collective excitations of systems close to equilibrium in section 8.4. The spin dipole mode is an oscillation of the centre of mass of the system. In our case we consider $d(t)/d_0$, the distance between the z -coordinates of the centres of

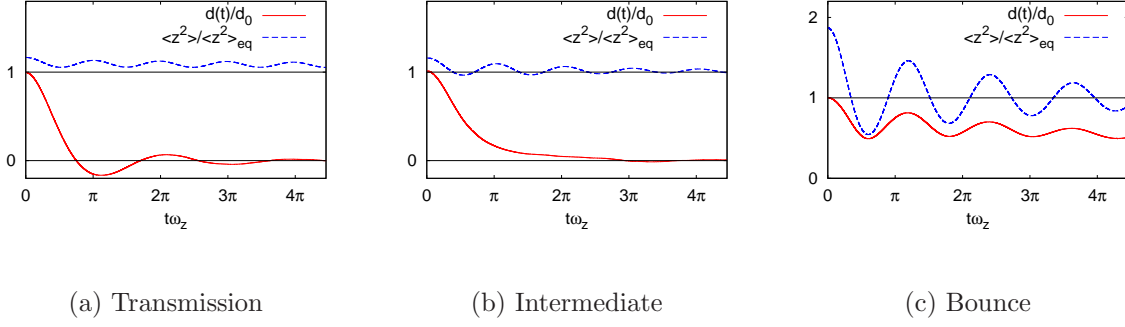


Figure 9.3: The normalised dipole mode $d(t)/d_0$ (red solid lines) and breathing mode $b(t)/b_\infty$ (blue dashed lines) for the three different behaviours: transmission (a), intermediate (b) and bounce (c).

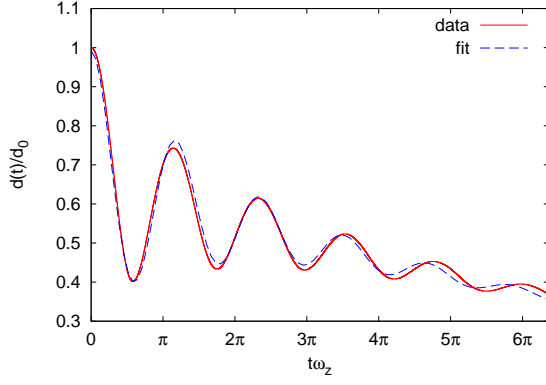
mass of the two clouds, normalised by their initial separation. We will compare it to the axial breathing mode $b(t) = \langle z_\uparrow^2 + z_\downarrow^2 \rangle(t)$. Figure 9.3 shows plots in the three regimes of the normalised amplitude of the dipole mode $d(t)/d_0$ and normalised amplitude of the breathing mode $b(t)/b_\infty$. We can see from Fig. 9.3(c) that in the bounce regime the frequency of $d(t)$ is identical to the frequency of $b(t)$. This suggests the existence of a non-linear coupling between the two modes. As we move towards the intermediate regime shown in Fig. 9.3(b) the frequency of the dipole mode becomes ill-defined due to the strong damping. In the transmission regime, see Fig. 9.3(a), it becomes closer to the frequency of the dipole mode of the non-interacting gas ω_z , as discussed in the previous section. This indicates that the dipole mode decouples from the breathing mode.

For a more quantitative analysis we fit $d(t)$ with the function

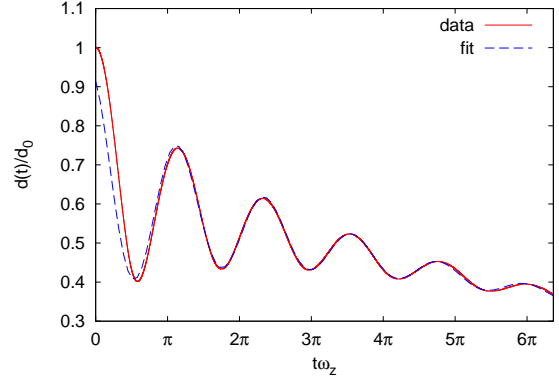
$$d(t) = B e^{-t/C} (1 + D e^{-t/E} \sin(\omega t + \phi)). \quad (9.3)$$

The first term is related to the spin drag coefficient measured in [37], which we will analyse in section 9.4. It dominates the overdamped behaviour of $d(t)$ at long times with a characteristic timescale C . The second term was not quantitatively analysed in [37] since it takes into account the short time behaviour which includes a damped oscillation with a typically shorter damping time scale E .

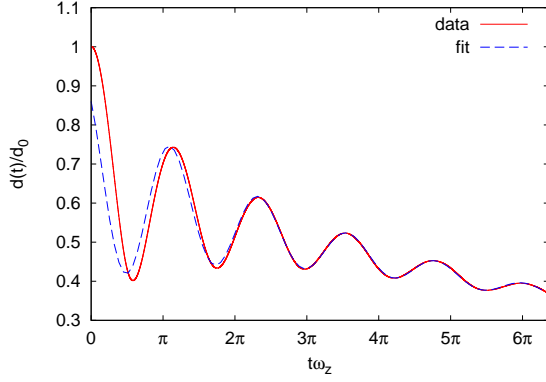
For displacements $d_0 \gtrsim 2\sigma_z$ the values of the fit parameters depend significantly on the range of the data included in the fit. To illustrate this Fig. 9.4 shows fits for different data ranges for the system with $T_{\text{init}} = 0.4\tilde{T}_F$, $|\tilde{k}_F a| = 1$ and $d_0 = 3\sigma_z$. Table 9.1 compares the corresponding fit parameter values. The frequency ω/ω_z for instance becomes smaller with increasing cut-off times. Since the frequency shows this weak time dependence we ignore early times by imposing a cut-off d_c on the amplitude and fitting only times $t > t_c$ for which $d(t) < d_c$. Since the function $d(t)$ is not monotonic



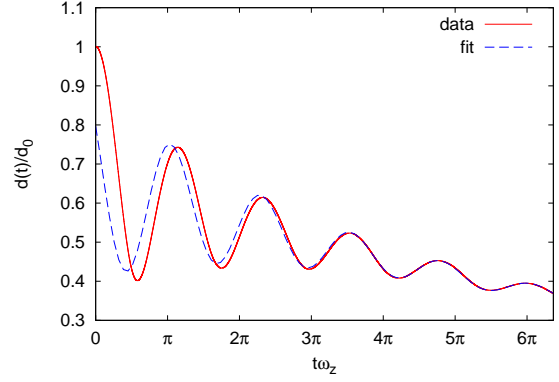
(a) full data range, $t_c\omega_z = 0$



(b) without first bounce, $t_c\omega_z \approx 1.1\pi$



(c) without first two bounces, $t_c\omega_z \approx 2.3\pi$



(d) without first three bounces, $t_c\omega_z \approx 3.5\pi$

Figure 9.4: Dependence of the best fit of the normalised dipole mode $d(t)/d_0$ to Eq. (9.3) on the range of the data used for the fit. All data were obtained for the system $T_{\text{init}} = 0.4\tilde{T}_F$, $|\tilde{k}_F a| = 1$, $d_0 = 3\sigma_z$.

	$t_c\omega_z$	B/d_0	$C\omega_z$	D	$E\omega_z$	ω/ω_z	ϕ
full data range	0	0.668	32.7	0.488	6.59	1.71	0.459π
without first bounce	1.1π	0.652	34.9	0.425	8.11	1.64	0.606π
without first two bounces	2.3π	0.652	34.9	0.392	8.66	1.62	0.696π
without first three bounces	3.5π	0.655	34.5	0.379	8.86	1.59	0.806π

Table 9.1: Dependence of the best fit parameters to Eq. (9.3) on the data range used for the fit. All data were obtained for the system $T_{\text{init}} = 0.4\tilde{T}_F$, $|\tilde{k}_F a| = 1$, $d_0 = 3\sigma_z$.

the corresponding time cut-off t_c is not continuous with changing d_0 , which leads to a small systematic error. We estimate this error from the cut-off dependence of the fit parameters. The statistical error of the fit is several orders of magnitude smaller and hence negligible.

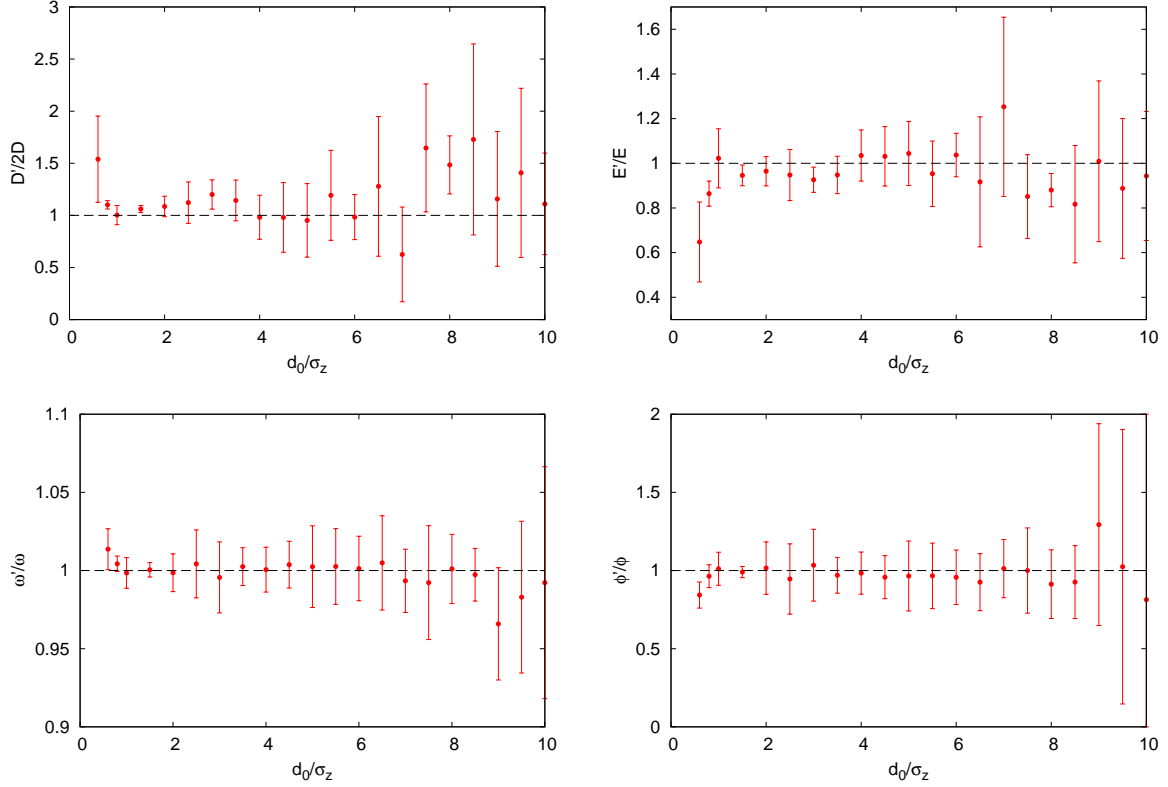


Figure 9.5: Comparison between the fit parameters in (9.3) and (9.4) for $|\tilde{k}_F a| = 1$, $T_{\text{init}} = 0.4\tilde{T}_F$ and different values of initial separation. The numerical results confirm the relations (9.5).

The oscillations of the axial size of the cloud are fitted using the dependence

$$b(t)/b_\infty = 1 + D'e^{-t/E'} \sin(\omega't + \phi'). \quad (9.4)$$

From the fit to our simulations, we observe that

$$D' \simeq 2D, \quad (9.5a)$$

$$E' \simeq E, \quad (9.5b)$$

$$\omega' \simeq \omega, \quad (9.5c)$$

$$\phi' \simeq \phi, \quad (9.5d)$$

as shown in Fig. 9.5. This result can be explained by noting that in the hydrodynamic and the collisionless regimes, the spin dipole and breathing modes can be described by a shift and a scaling of the phase space density. We assume that this also applies here and take for the variation of the density of the spin species s along the z -axis the ansatz

$$n_s(z, t) = \alpha n_s(\alpha z \pm \beta, 0), \quad (9.6)$$

where $\alpha = \alpha(t)$ and $\beta = \beta(t)$ represent the breathing and spin dipole modes respectively. Using this ansatz, we can express $b(t)$ and $d(t)$ as functions of α and β :

$$\langle z \rangle = \int z n_s(z, t) dz, \quad (9.7)$$

$$= \int z \alpha n_s(\alpha z \pm \beta, 0) dz, \quad (9.8)$$

$$= \frac{1}{\alpha} \int (u_{\pm} \mp \beta) n_s(u_{\pm}, 0) du_{\pm}, \quad \text{with } u_{\pm} = \alpha z \pm \beta, \quad (9.9)$$

$$= \mp \frac{\beta}{\alpha}, \quad (9.10)$$

using $\int n_s(u) du = 1$ and $\int u n_s(u) du = 0$. Hence

$$d(t) = \langle z_{\uparrow} - z_{\downarrow} \rangle(t) = 2 \frac{\beta(t)}{\alpha(t)}. \quad (9.11)$$

Similarly

$$\langle z^2 \rangle = \int z^2 \alpha n_s(\alpha z \pm \beta, 0) dz, \quad (9.12)$$

$$= \frac{1}{\alpha^2} \int (u_{\pm} \mp \beta)^2 n_s(u_{\pm}, 0) du_{\pm}, \quad (9.13)$$

$$= \frac{1}{\alpha^2} (\langle u^2 \rangle_{\text{eq.}} + \beta^2), \quad (9.14)$$

as the linear term again vanishes. If we also ignore the second order contribution in β we obtain

$$\frac{b(t)}{b_{\infty}} = \frac{\langle z_{\uparrow}^2 + z_{\downarrow}^2 \rangle(t)}{\langle z^2 \rangle_{\text{eq.}}} \approx \frac{1}{\alpha^2(t)}. \quad (9.15)$$

Now we assume that $\beta(t)$ is overdamped,

$$\beta(t) = B e^{-t/C}, \quad (9.16)$$

and that $\alpha(t)$ is a damped oscillation,

$$\alpha(t) = 1 + D e^{-t/E} \sin(\omega t + \phi), \quad (9.17)$$

and then by expanding Eqs. (9.11) and (9.15) to leading order we obtain the time dependence in Eqs. (9.3) and (9.4) together with the corresponding relations between the coefficients (9.5).

We are also able to study the temperature dependence of the frequency of the two modes, see Fig. 9.6. We obtain the frequency by fitting to the functions (9.3) for the dipole mode and (9.4) for the breathing mode. As we increase the temperature, the frequency of the spin dipole and breathing modes increases from $\sqrt{12/5} \omega_z \approx 1.55 \omega_z$,

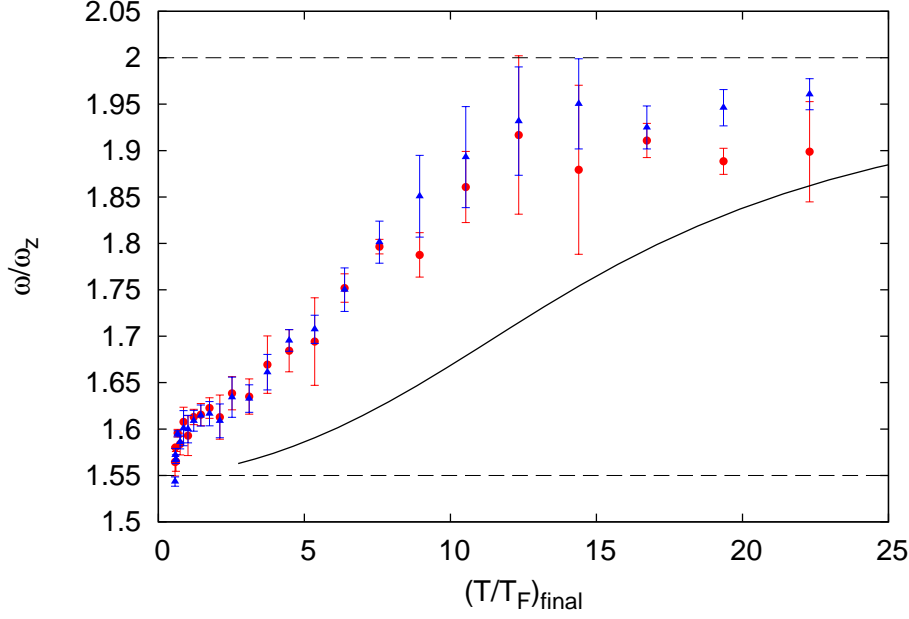


Figure 9.6: The frequency ω/ω_z of the dipole mode $d(t)$ (red circles) and the breathing mode $b(t)$ (blue triangles) versus the final temperature for $|\tilde{k}_F a| = 1$. All data were obtained for equal initial temperature $T_{\text{init}} = 0.4\tilde{T}_F$ by varying d_0 . The solid line is the prediction from [93].

the frequency of the hydrodynamic axial breathing mode [93, 94], and approaches $2\omega_z$, the non-interacting value. This is in agreement with the value for the bounce frequency at unitarity $\omega = 1.63(2)\omega_z$ measured in [37]. At higher temperatures the spin dipole mode frequency becomes ill-defined due to large damping. If we continue to increase the temperature, the damping becomes progressively smaller and the dipole mode frequency approaches ω_z , the value for the non-interacting gas, as was discussed above. We also compare our results with an earlier prediction for the frequency of the breathing mode [93]. The two dependencies are close to each other although some discrepancy remains. We attribute it to the fact that to estimate the collisional rate in the cloud Ref. [93] neglects the Pauli principle and assumes a Gaussian phase-space density. The temperature dependence of the frequency remains the same if we change the scattering length or the initial temperature of the system, as shown in Fig. 9.7.

9.4 Transport coefficients

Transport coefficients characterise the macroscopic response of a system towards an external perturbation. Usually we consider linear response to weak perturbations with the transport coefficient being the proportionality factor. In this section we will discuss how different transport coefficients can be calculated from the numerical data.

The spin drag coefficient Γ_{sd} characterises the linear response in the relative spin

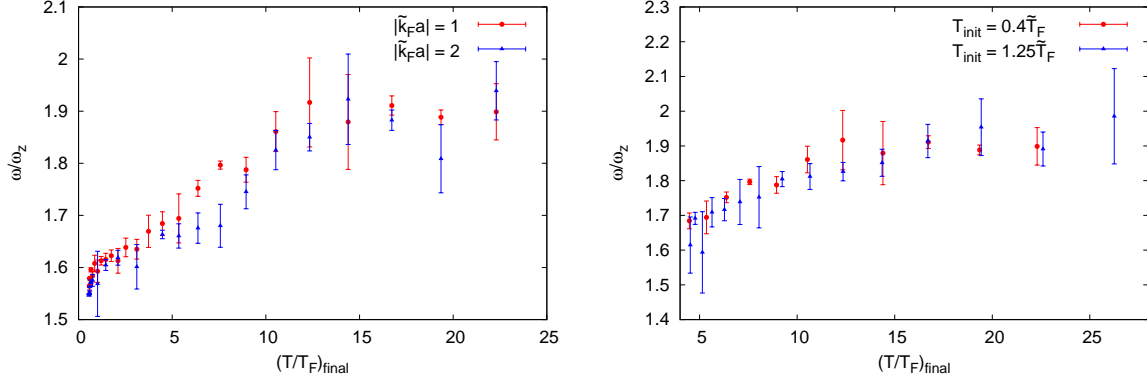


Figure 9.7: The frequency ω/ω_z of the dipole mode $d(t)$ versus the final temperature for $T_{\text{init}} = 0.4\tilde{T}_F$ and two different values of the scattering length (left), and for $|\tilde{k}_F a| = 1$ and two different values of the initial temperature (right). No dependence on either the scattering length or the initial temperature is visible.

current towards a weak external force. It is defined through

$$\langle \mathbf{F}_{\uparrow\downarrow} \rangle = -\Gamma_{\text{sd}} \langle \mathbf{p}_{\uparrow} - \mathbf{p}_{\downarrow} \rangle, \quad (9.18)$$

where $\langle \mathbf{F}_{\uparrow\downarrow} \rangle = -(\nabla V(\langle \mathbf{r}_{\uparrow} \rangle) - \nabla V(\langle \mathbf{r}_{\downarrow} \rangle))$ is the force between the centres of mass of the two fermionic clouds [95]. If the clouds are displaced along the z -direction in a harmonic external potential we obtain

$$\omega_z^2 d + \Gamma_{\text{sd}} \dot{d} = 0, \quad (9.19)$$

for small displacements from equilibrium. The solution to this equation is

$$d(t) \propto e^{-t\omega_z^2/\Gamma_{\text{sd}}}, \quad (9.20)$$

in agreement with the overdamped behaviour (9.16) near equilibrium which is seen in the experiment and the numerical simulation at sufficiently long times. Hence the spin drag coefficient can be obtained from the fit coefficient C via

$$\Gamma_{\text{sd}} = C\omega_z^2. \quad (9.21)$$

An explicit form for the spin drag of the homogeneous gas at non-degenerate temperatures can be obtained by solving the Boltzmann equation in the classical regime with a variational approach, as shown for instance in the supplementary material to [37] and references therein. One obtains

$$\Gamma_{\text{sd}}^{(\text{hom})} = \frac{8}{3} n \sigma(a, T) \left(\frac{T}{\pi m} \right)^{1/2}, \quad (9.22)$$

where

$$\sigma(a, T) = 4\pi a^2 \int du \frac{u^5 e^{-u^2}}{1 + u^2 m a^2 T} \quad (9.23)$$

$$= \frac{2\pi}{mT} \left(1 - \frac{1}{m a^2 T} - \frac{1}{(m a^2 T)^2} e^{\frac{1}{m a^2 T}} \text{Ei} \left(-\frac{1}{m a^2 T} \right) \right). \quad (9.24)$$

For weak interactions the cross section stays nearly constant, $\sigma(m a^2 T \ll 1) = 4\pi a^2$, and the spin drag is proportional to the square root of the temperature. In the limit of large scattering length ($m a^2 T \gg 1$) expression (9.24) simplifies to

$$\sigma(m a^2 T \gg 1) = \frac{2\pi}{mT}, \quad (9.25)$$

which is the square of the thermal de Broglie wavelength. Therefore the dimensionless spin drag coefficient at unitarity is

$$\frac{\Gamma_{\text{sd}}^{(\text{hom})}}{\varepsilon_F} = \frac{32\sqrt{2}}{9\pi^{3/2}} \left(\frac{T}{T_F} \right)^{-1/2} \approx 0.90 \left(\frac{T}{T_F} \right)^{-1/2}. \quad (9.26)$$

At very low temperatures there is no reliable microscopic theory that could predict the spin drag coefficient. In [38] the spin relaxation time, which is inversely proportional to the spin drag, is calculated also at low temperature using Fermi liquid theory to include the effect of strong correlations. The calculation reveals that $\Gamma_{\text{sd}}^{(\text{hom})}$ has a maximum in the strong coupling limit. At unitarity this maximum is found at temperatures around the Fermi temperature T_F . At low temperatures the spin drag behaves according to $\Gamma_{\text{sd}}^{(\text{hom})}/\varepsilon_F \sim (T/T_F)^2$ at unitarity, and $\Gamma_{\text{sd}}^{(\text{hom})}/\varepsilon_F \sim (T/T_F)^2 (k_F a)^2$ for weak interactions. This is in agreement with the experimental observations [37]. To understand the temperature dependence of the spin drag qualitatively note that for a classical gas the cross section increases with decreasing temperature. The maximum of the spin drag can be understood as a consequence of the onset of Pauli blocking at low temperatures, which causes the cross section to decrease again.

In the presence of a non-uniform external potential the spin drag will depend on the spatial position. From a fit to $d(t)$ we can obtain only the trap average Γ_{sd} which is related to the local spin drag $\Gamma_{\text{sd}}(\mathbf{r})$ via

$$\Gamma_{\text{sd}} \dot{d} = \Gamma_{\text{sd}} \langle v_{\text{rel},z}(\mathbf{r}) \rangle = \langle \Gamma_{\text{sd}}(\mathbf{r}) v_{\text{rel},z}(\mathbf{r}) \rangle. \quad (9.27)$$

The z -component of the relative velocity $v_{\text{rel},z}$ consists of the equilibrium term and the drift velocity term $\pm v_d(\mathbf{r})$ describing the directed motion of the spin up and spin down atoms towards the trap centre in response to the displacement of the clouds. The average equilibrium velocity is zero, due to symmetry of the equilibrium distribution.

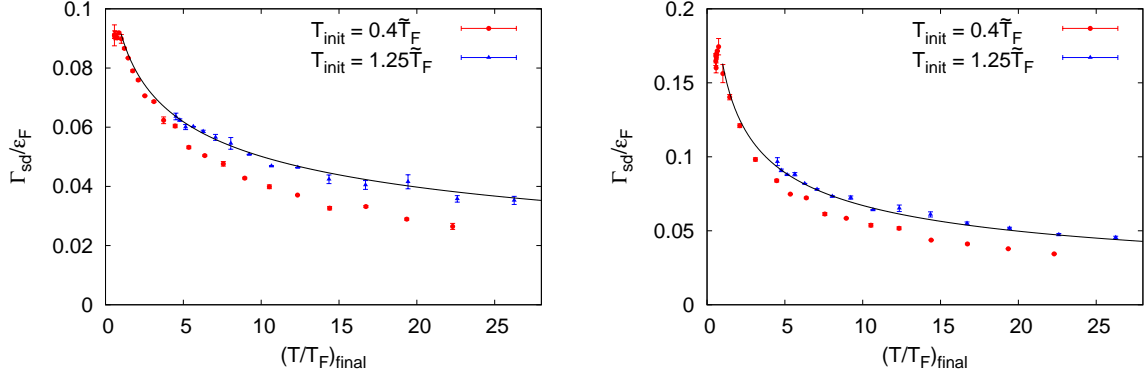


Figure 9.8: The average spin drag Γ_{sd} versus final temperature for $|\tilde{k}_F a| = 1$ (left) and $|\tilde{k}_F a| = 2$ (right). Red circles denote simulation results obtained for $T_{\text{init}} = 0.4\tilde{T}_F$ and blue triangles simulation results obtained for $T_{\text{init}} = 1.25\tilde{T}_F$, by varying the initial separation. The lines are fits of the data for $T_{\text{init}} = 1.25\tilde{T}_F$ to $\Gamma_{\text{sd}}^{(\text{hom})}/\alpha$, where the homogeneous spin drag is given by (9.22) and α is a free fit parameter.

Hence we can write for the average spin drag,

$$\Gamma_{\text{sd}} = \frac{\langle \Gamma_{\text{sd}}(\mathbf{r}) v_{\text{rel},z}(\mathbf{r}) \rangle}{\langle v_{\text{rel},z}(\mathbf{r}) \rangle} = \frac{\int d^3r \Gamma_{\text{sd}}(\mathbf{r}) n(\mathbf{r}) v_d(\mathbf{r})}{\int d^3r n(\mathbf{r}) v_d(\mathbf{r})}. \quad (9.28)$$

The local spin drag $\Gamma_{\text{sd}}(\mathbf{r})$ can be approximated by the homogeneous value (9.22) with the uniform density n replaced by the local density $n(\mathbf{r})$. This yields

$$\Gamma_{\text{sd}} = \frac{\Gamma_{\text{sd}}(\mathbf{0}) \int d^3r n^2(\mathbf{r}) v_d(\mathbf{r})}{n(\mathbf{0}) \int d^3r n(\mathbf{r}) v_d(\mathbf{r})}. \quad (9.29)$$

Hence the average spin drag coefficient is proportional to the local value at the trap centre, $\Gamma_{\text{sd}} = \Gamma_{\text{sd}}(\mathbf{0})/\alpha$, where the coefficient α is given by

$$\alpha = \frac{n(\mathbf{0}) \int d^3r n(\mathbf{r}) v_d(\mathbf{r})}{\int d^3r n^2(\mathbf{r}) v_d(\mathbf{r})} \quad (9.30)$$

and can only be calculated by making an assumption about the drift velocity profile of the gas [37]. In a harmonic potential, one obtains $\alpha = 2^{3/2} \approx 2.83$ assuming a uniform drift velocity, and $\alpha = 2^{5/2} \approx 5.66$ if one assumes a quadratic drift velocity profile. Compared to the local spin drag at the trap centre the average spin drag is lower by the factor α .

Our results for the spin drag coefficient for $|\tilde{k}_F a| = 1$ and $|\tilde{k}_F a| = 2$ are presented in Fig. 9.8 together with a fit to the analytical prediction (9.22) at high temperatures. A key observation is that, unlike the oscillation frequency, the average spin drag shows a dependence on the initial temperature and displacement and is not purely a function of the final temperature. We compare two data sets for each scattering length, one

obtained at a low initial temperature $T_{\text{init}} = 0.4\tilde{T}_F$ and one at a high initial temperature $T_{\text{init}} = 1.25\tilde{T}_F$. The data at the high initial temperature is fitted well by the analytical prediction for $\Gamma_{\text{sd}}^{(\text{hom})}/\alpha$, where the homogeneous spin drag is given by (9.22) and α is a free fit parameter. For $|\tilde{k}_F a| = 1$ the fit yields $\alpha = 3.34(8)$ and for $|\tilde{k}_F a| = 2$ the fit yields $\alpha = 3.52(11)$. These two values are consistent with each other within error. If we fit both data sets together we obtain $\alpha = 3.35(15)$.

The high temperature tail of the data obtained using $T_{\text{init}} = 0.4\tilde{T}_F$ and large initial separations is on the other hand not well-fitted by the theoretical prediction. We attribute this to the fact that for large initial separations non-linear effects strongly influence the drift velocity profile and hence the points in the tail do not all correspond to the same value of α . This obscures the proportionality relation between the average spin drag and the homogeneous value. In support of this argument note that the points for $T_{\text{init}} = 0.4\tilde{T}_F$ and final temperatures between approximately T_F and $5T_F$ lie close to the fit to the analytical prediction. Only when the final temperature increases further, for which larger initial separations are needed, does the data start to deviate.

We can also see the predicted maximum of the spin drag around the Fermi temperature. The spin drag then starts to decrease again as we go to even lower temperatures but this regime is not yet fully accessible with the simulation.

The values for α extracted from the fits lie between the predictions for a uniform and a quadratic velocity profile. In [37] a higher value for α was found at unitarity, closer to the prediction for a quadratic drift velocity profile. In the experimental setup fast particles evaporate from the trap, such that the time-evolution of the clouds is isothermal. In our numerical setup the particle number is conserved, but not the temperature. This affects the drift velocity profile and hence the relation between the average and the local spin drag coefficients. In our setup the average spin drag coefficient is closer to the homogeneous value.

It is possible to access also other transport coefficients, for instance the spin diffusion coefficient D_s which is given by Fick's law,

$$\langle \mathbf{j}_{\uparrow\downarrow} \rangle = -D_s \nabla(n_{\uparrow} - n_{\downarrow}), \quad (9.31)$$

where $\langle \mathbf{j}_{\uparrow\downarrow} \rangle = n \langle \mathbf{v}_{\uparrow} - \mathbf{v}_{\downarrow} \rangle$ is the spin current [37, 38]. Note that in the presence of an external potential this definition is in terms of the local densities. Using values at the trap centre the spin diffusion coefficient can be extracted from the simulation data via

$$D_s = -\frac{n(\mathbf{0})\dot{d}}{g(0)} = \frac{n(\mathbf{0})\omega_z^2 d}{\Gamma_{\text{sd}} g(0)}, \quad (9.32)$$

where $g(z) = \partial_z(n_{\uparrow} - n_{\downarrow})$ is the slope of the local density difference at $x = y = 0$. The above formula is only valid close to equilibrium when $d(t)$ decreases exponentially with time satisfying Eq. (9.19). The quantities d , $n(\mathbf{0})$ and $g(0)$ are time-dependent,

however these dependencies should cancel, such that D_s is constant close to equilibrium. Similarly one can also obtain the spin susceptibility via

$$\chi_s = \frac{g(0)}{md\omega_z^2}. \quad (9.33)$$

The calculation of these and other transport coefficients will be subject of future research.

Conclusions and Outlook

In the first part of this thesis we discussed a Monte Carlo calculation of the critical temperature and other thermodynamic observables of the homogeneous unitary Fermi gas with equal and unequal chemical potentials for the two spin components. This work contains two main improvements compared to previous DDMC studies: a new update scheme which is less susceptible to autocorrelations than the original worm algorithm, and an alternative procedure for extracting the thermodynamic limit of the critical temperature from the numerical data that avoids a systematic error present in several other studies. Due to these improvements we could provide a more accurate estimate on the critical temperature than the previously established value. We also generalised the DDMC algorithm to the imbalanced case using the sign quenched method allowing for the first time to numerically access the thermodynamic properties of the spin imbalanced unitary Fermi gas.

Our most precise values (using data at both zero and non-zero imbalance) for the temperature, the chemical potential, the energy per particle and the contact density of the balanced unitary Fermi gas at the critical point are

$$T_c/\varepsilon_F = 0.171(5), \quad (10.1)$$

$$\mu/\varepsilon_F = 0.429(7), \quad (10.2)$$

$$E/E_{\text{FG}} = 0.440(15), \quad (10.3)$$

$$\mathcal{C}/\varepsilon_F^2 = 0.1101(9). \quad (10.4)$$

The value for the contact density was the first numerically obtained finite temperature result for this quantity.

For unequal chemical potentials in the two components we extracted the dependence of the critical temperature on the imbalance $h = \Delta\mu/\varepsilon_F$ close to the balanced limit. Our analysis is consistent with $T_c/\varepsilon_F = \text{const.}$ for the range of imbalances considered ($h \lesssim 0.2$). We also derived a lower bound on the leading order term in the expansion of the critical temperature $T_c(h) - T_c(0) > -0.5\varepsilon_F h^2$. With the additional assumption that the linear dependence of the lattice critical temperature T_c/ε_F on $\nu^{1/3}$ remains unchanged in the presence of a small imbalance, a tighter lower bound of $T_c(h) - T_c(0) > -0.04\varepsilon_F h^2$ could be obtained. We also analysed the behaviour of the energy,

the chemical potential and the contact density in the presence of an imbalance. In all cases we saw good agreement with experimental results.

We also studied the above mentioned quantities for the balanced gas at temperatures above and below T_c . We found that the chemical potential decreases with increasing temperature, while the energy and the contact density increase with increasing temperature. This is still work in progress; in particular we expect to increase the precision of our results when data at the lowest filling factor used for the analysis at T_c becomes available. So far we have not studied the spin imbalanced gas at temperatures beyond T_c , which will be explored in future work.

Our DDMC study could provide results for several thermodynamic observables with an accuracy of a few percent. Nevertheless there is still much room for improvement. A major source of statistical errors is the continuum extrapolation of the data. Due to lattice discretisation effects observables calculated at finite values of the chemical potential do not equal the physical observables in the continuum limit. Since due to technical limitations we cannot use arbitrarily large lattice sizes, we cannot work arbitrarily close to continuum. The slope of the continuum extrapolation is large due to the significant difference between the lattice dispersion relation and the parabolic continuous dispersion relation. Reducing this slope would allow us to get more precise continuum values without having to go to very low values of the chemical potential. To achieve this a more complex dispersion relation than the one used in this work can be invoked. We have already briefly discussed dispersion relations that completely suppress leading order lattice corrections and aim to investigate such dispersion relations in future work.

The efficiency of the simulation can be further increased by inventing more elaborate update schemes. For instance updates that insert or remove entire vertex chains into the configuration would change the configuration significantly in only one Monte Carlo step. This would further reduce errors associated with autocorrelations and speed the simulations.

The improved DDMC algorithm with sign quenching also offers the intriguing possibility to explore the case of unequal masses of the two species. If $m_\uparrow \neq m_\downarrow$ the dispersion relations are different for the two components and the mass ratio enters as a new parameter. As in the spin-imbalanced case the two matrix determinants no longer need to be identical, so that sign quenching is required. The mass ratio is expected to influence the behaviour of the system significantly, so that exploring the phase diagram promises many new interesting insights.

To access dynamical properties of a Fermi gas above the critical temperature and at finite values of the scattering length, we have implemented and tested a numerical simulation of the Boltzmann equation. With this simulation we have studied the collision of two spin polarised Fermi clouds in a cigar shaped harmonic trap. In agreement with recent experimental observations [37] we identified three distinct regimes of behaviour

which can be characterised in terms of the centre of mass separation between the two clouds. For weak interactions the clouds pass through each other. If interactions are increased they approach each other exponentially and for strong interactions they bounce off each other several times. We characterised the transitions between these regimes as a function of interaction strength and temperature, and related them to the collision rate in the overlap region between the clouds. We then explained the occurrence of the bouncing as the consequence of a non-linear coupling between the spin dipole mode and the axial breathing mode, which is enforced by collisions. Such a non-linear coupling between collective modes has, to our knowledge, never before been studied in a Fermi gas. We also determined the frequency of the bounce as a function of the final temperature of the equilibrated system. Finally, we discussed how spin transport coefficients can be extracted from the numerical data. We calculated the trap average of the spin drag coefficient and found good agreement with the analytical prediction.

In future we aim to extend this study to other closely related problems such as the collision of clouds with unequal populations [40], between clouds of atoms with unequal masses [96], and to the Fermi liquid regime at $T \ll T_F$, using the Landau-Boltzmann equation. The low temperature regime is especially fascinating as, although it is experimentally accessible, very few analytical results are known.

Our numerical setup gives us precise control over all system parameters and allows us to monitor quantities not easily accessible in an experiment. We can follow the trajectory of any given particle and obtain local collision rates, density and velocity profiles as a function of time. In particular the velocity profile is interesting as it gives insight about the relation between homogeneous and trap averaged transport coefficients. Without knowledge of the drift velocity no theory for the average spin drag in a trap can be formulated. We plan to resolve this question by a detailed study of the time-dependent drift velocity profile as a function of the temperature, the scattering length and the initial separation of the clouds. Apart from the spin drag we intend to calculate also other transport coefficients like the spin diffusion coefficient or the spin susceptibility.

So far we have not studied the dynamics of the trapped unitary Fermi gas. At unitarity the s -wave cross section diverges for small relative momenta of the two colliding atoms. This regime can be made accessible by enforcing a low-momentum cut-off, which we aim to explore this in future work.

Matrix update procedure

In [50] Rubtsov et al. develop a fast update algorithm designed for the types of matrix updates described in chapter 5. It is based on calculating the inverse of the matrices, which gives the determinants as a side product. The calculation of the determinant of an arbitrary $N \times N$ matrix requires order N^3 operations. If a matrix, which determinant is already known, is modified, e.g. by changing one or several rows and/or columns, the calculation of the determinant of the updated matrix can sometimes be performed in less than N^3 operations. In the following, we will derive all three kinds of update and give the number of operations needed to perform them. Note that Einstein's summation convention is not used: all sums are indicated explicitly and a repeated index is not necessarily summed over.

A.1 The Sherman-Morrison Formula

Suppose that we have already inverted a matrix A and want to obtain the inverse of a modified matrix A' , that differs from A in some elements, e.g. in a row or a column. A matrix inversion from scratch requires order N^3 operations, but having already inverted A we can hope to calculate the inverse of A' more efficiently. If the change in the matrix is of the form

$$A' = A + u \otimes v, \tag{A.1}$$

where $u \otimes v$ is a matrix whose (i, j) element is the product $u_i v_j$, the Sherman-Morrison formula gives the inverse of A' as

$$(A + u \otimes v)^{-1} = A^{-1} - \frac{(A^{-1}u) \otimes (v \cdot A^{-1})}{1 + v \cdot A^{-1}u}. \tag{A.2}$$

It can be derived as follows [97]:

$$(A + u \otimes v)^{-1} = (1 + A^{-1} \cdot u \otimes v)^{-1} \cdot A^{-1} \quad (\text{A.3})$$

$$= (1 - A^{-1} \cdot u \otimes v + A^{-1} \cdot u \otimes v \cdot A^{-1} \cdot u \otimes v \mp \dots) \cdot A^{-1} \quad (\text{A.4})$$

$$= A^{-1} - A^{-1} \cdot u \otimes v \cdot A^{-1} + A^{-1} \cdot u \otimes v \cdot A^{-1} \cdot u \otimes v \cdot A^{-1} \mp \dots \quad (\text{A.5})$$

$$= A^{-1} - A^{-1} \cdot u \otimes v \cdot A^{-1} (1 - \Lambda + \Lambda^2 \mp \dots) \quad (\text{A.6})$$

$$= A^{-1} - \frac{(A^{-1} \cdot u) \otimes (v \cdot A^{-1})}{1 + \Lambda}, \quad (\text{A.7})$$

where $\Lambda \equiv v \cdot (A^{-1}u)$ and Taylor expansion was used in (A.4). In (A.6) the scalars Λ were factored out and in (A.7) the series was written as $(1 + \Lambda)^{-1}$ using Taylor expansion again.

Let us count the number of operations required for the calculation of $(A + u \otimes v)^{-1}$, first for arbitrary vectors u and v and then for the special cases $u = e_n$ or $v = e_n$, which correspond to changing all elements of the n th row or n th column of the matrix respectively. The quantities that need to be computed are

$A^{-1}u$	(vector)	\rightarrow	N^2 mult.,	$(N - 1)^2$ add.
$v \cdot A^{-1}$	(vector)	\rightarrow	N^2 mult.,	$(N - 1)^2$ add.
$\Lambda = (v \cdot A^{-1})u$	(scalar)	\rightarrow	N mult.,	$N - 1$ add.
$\frac{A^{-1}u}{1 + \Lambda}$	(vector)	\rightarrow	N mult.,	1 add. $(1 + \Lambda)$
$\frac{A^{-1}u}{1 + \Lambda} \otimes (v \cdot A^{-1})$	(matrix)	\rightarrow	N^2 mult.,	(1 for each matrix element)
$A^{-1} - \frac{A^{-1}u}{1 + \Lambda} \otimes (v \cdot A^{-1})$	(matrix)	\rightarrow	N^2 add.,	(1 for each matrix element)

So, in general, this method requires order $3N^2$ multiplications and $3N^2$ additions. Modifying a single row or column of A corresponds to setting either u or v to a unit vector e_n . In this case the computation of either $A^{-1}u$ or $v \cdot A^{-1}$ reduces to just picking the n th column or the n th row of A^{-1} respectively. This saves us N^2 multiplications and $(N - 1)^2$ additions, so that the total cost reduces to order $2N^2$ multiplications and $2N^2$ additions. Unfortunately, a change in one row and one column of a matrix cannot be written in the form $u \otimes v$, so that for this update we need to perform the row and the column update separately, yielding order $4N^2$ multiplications and additions.

The worm type updates involve additions and removals of one row and one column. This can be reformulated in terms of changing an existing row and column in the following way: We can first add a “unit” row n and a “unit” column m to A , with $A_{nj} = \delta_{mj}$ and $A_{im} = \delta_{in}$. This does not change the determinant. The inverse matrix is also almost unchanged, it only gets an extra “unit” row m and “unit” column n , with $A_{mj}^{-1} = \delta_{nj}$ and $A_{in}^{-1} = \delta_{im}$ (note that m and n get swapped for the inverse). Now we can modify the added row and column in the usual way using the Sherman-Morrison formula. Removing a row and a column can be done analogously: We change the row

n and column m we want to remove to $A_{nj} = \delta_{mj}$ and $A_{im} = \delta_{in}$ using Sherman-Morrison and then drop them and also drop the corresponding row m and column n in the inverse matrix. The number of operations for this type of updates is also order $4N^2$ multiplications and same for additions.

The updates proposed in [50] are an extension of the Sherman-Morrison formula. In the following three sections, we will derive the three kinds of update and calculate their complexity.

A.2 Adding one row and one column

Let us first consider the update that adds an $(N + 1)$ st row and column to an $N \times N$ matrix A (the order of rows and columns is not important, since a permutation of rows/columns of A yields a permutation of columns/rows of A^{-1}). As described at the end of the previous section, we first extend the $N \times N$ matrix A to an $(N + 1) \times (N + 1)$ matrix with $A_{N+1,j} = A_{i,N+1} = 0$ for $i, j = 1, \dots, N$ and $A_{N+1,N+1} = 1$,

$$A = \begin{pmatrix} A_{1,1} & \cdots & A_{1,N} \\ \vdots & & \vdots \\ A_{N,1} & \cdots & A_{N,N} \end{pmatrix} \rightarrow \left(\begin{array}{ccc|c} & & & 0 \\ & A & & \vdots \\ & & & 0 \\ \hline 0 & \cdots & 0 & 1 \end{array} \right) = \begin{pmatrix} A_{1,1} & \cdots & A_{1,N} & 0 \\ \vdots & & \vdots & \vdots \\ A_{N,1} & \cdots & A_{N,N} & 0 \\ 0 & \cdots & 0 & 1 \end{pmatrix}. \quad (\text{A.8})$$

This does not change the determinant and the inverse of A also gets extended in the same way,

$$A^{-1} = \begin{pmatrix} A_{1,1}^{-1} & \cdots & A_{1,N}^{-1} \\ \vdots & & \vdots \\ A_{N,1}^{-1} & \cdots & A_{N,N}^{-1} \end{pmatrix} \rightarrow \left(\begin{array}{ccc|c} & & & 0 \\ & A^{-1} & & \vdots \\ & & & 0 \\ \hline 0 & \cdots & 0 & 1 \end{array} \right) = \begin{pmatrix} A_{1,1}^{-1} & \cdots & A_{1,N}^{-1} & 0 \\ \vdots & & \vdots & \vdots \\ A_{N,1}^{-1} & \cdots & A_{N,N}^{-1} & 0 \\ 0 & \cdots & 0 & 1 \end{pmatrix}. \quad (\text{A.9})$$

The extended matrices will be denoted with the same letters as the original ones, since from here on only the former will be used. The extension enables us to perform matrix additions and multiplications of the original and the updated matrix, for it is only possible to perform these operations with matrices of the same size. We want to find the inverse of the updated matrix $A' = A + \Delta$, where

$$\Delta = \begin{pmatrix} 0 & \cdots & 0 & A_{1,N+1} \\ \vdots & & \vdots & \vdots \\ 0 & \cdots & 0 & A_{N,N+1} \\ A_{N+1,1} & \cdots & A_{N+1,N} & A_{N+1,N+1} - 1 \end{pmatrix}. \quad (\text{A.10})$$

As in (A.3) we write

$$A'^{-1} = (A + \Delta)^{-1} = A^{-1}(1 + \Delta A^{-1})^{-1}. \quad (\text{A.11})$$

The next step in the derivation of the Sherman-Morrison formula was Taylor expanding the inverse of the term in brackets. In our case however, since Δ cannot be decomposed into a direct product of two vectors, this will not yield the desired result. Instead we can try to invert $1 + \Delta A^{-1}$ directly. For this consider

$$\begin{aligned} \Delta A^{-1} &= \begin{pmatrix} 0 & \cdots & 0 & A_{1,N+1} \\ \vdots & & \vdots & \vdots \\ 0 & \cdots & 0 & A_{N,N+1} \\ A_{N+1,1} & \cdots & A_{N+1,N} & A_{N+1,N+1} - 1 \end{pmatrix} \cdot \begin{pmatrix} A_{1,1}^{-1} & \cdots & A_{1,N}^{-1} & 0 \\ \vdots & & \vdots & \vdots \\ A_{N,1}^{-1} & \cdots & A_{N,N}^{-1} & 0 \\ 0 & \cdots & 0 & 1 \end{pmatrix} \\ &= \begin{pmatrix} 0 & \cdots & 0 & A_{1,N+1} \\ \vdots & & \vdots & \vdots \\ 0 & \cdots & 0 & A_{N,N+1} \\ R_1 & \cdots & R_N & A_{N+1,N+1} - 1 \end{pmatrix}, \end{aligned} \quad (\text{A.12})$$

where $R_j \equiv \sum_k A_{N+1,k} A_{k,j}^{-1}$. Thus

$$1 + \Delta A^{-1} = \left(\begin{array}{cccc|c} 1 & 0 & \cdots & 0 & A_{1,N+1} \\ 0 & 1 & & 0 & \\ \vdots & & \ddots & \vdots & \vdots \\ 0 & \cdots & 1 & & A_{N,N+1} \\ \hline R_1 & \cdots & R_N & & A_{N+1,N+1} \end{array} \right). \quad (\text{A.13})$$

This matrix is naturally partitioned into four blocks, an $N \times N$ block in the upper left corner, containing the unit matrix, a 1×1 “block” containing the single element $A_{N+1,N+1}$ and the two remaining blocks ($1 \times N$ and $N \times 1$) forming a row and a column of size N . In general, the inverse of a partitioned matrix \mathbf{B} ,

$$\mathbf{B} = \begin{pmatrix} \mathbf{P} & \mathbf{Q} \\ \mathbf{R} & \mathbf{S} \end{pmatrix} \quad (\text{A.14})$$

has the form [97]

$$\mathbf{B}^{-1} = \begin{pmatrix} \tilde{\mathbf{P}} & \tilde{\mathbf{Q}} \\ \tilde{\mathbf{R}} & \tilde{\mathbf{S}} \end{pmatrix}, \quad (\text{A.15})$$

where

$$\tilde{\mathbf{P}} = \mathbf{P}^{-1} + (\mathbf{P}^{-1} \cdot \mathbf{Q}) \cdot (\mathbf{S} - \mathbf{R} \cdot \mathbf{P}^{-1} \cdot \mathbf{Q})^{-1} \cdot (\mathbf{R} \cdot \mathbf{P}^{-1}), \quad (\text{A.16})$$

$$\tilde{\mathbf{Q}} = -(\mathbf{P}^{-1} \cdot \mathbf{Q}) \cdot (\mathbf{S} - \mathbf{R} \cdot \mathbf{P}^{-1} \cdot \mathbf{Q})^{-1}, \quad (\text{A.17})$$

$$\tilde{\mathbf{R}} = -(\mathbf{S} - \mathbf{R} \cdot \mathbf{P}^{-1} \cdot \mathbf{Q})^{-1} \cdot (\mathbf{R} \cdot \mathbf{P}^{-1}), \quad (\text{A.18})$$

$$\tilde{\mathbf{S}} = (\mathbf{S} - \mathbf{R} \cdot \mathbf{P}^{-1} \cdot \mathbf{Q})^{-1}. \quad (\text{A.19})$$

These formulae can be easily checked by multiplying \mathbf{B} with its inverse. The determinant of a partitioned matrix can be computed through

$$\det \mathbf{B} = \det \mathbf{P} \det(\mathbf{S} - \mathbf{R} \cdot \mathbf{P}^{-1} \cdot \mathbf{Q}) = \det \mathbf{S} \det(\mathbf{P} - \mathbf{Q} \cdot \mathbf{S}^{-1} \cdot \mathbf{R}). \quad (\text{A.20})$$

In our case, $\mathbf{P} = \mathbb{1}_N$, $\mathbf{Q} = (A_{1,N+1} \dots A_{N,N+1})^T$, $\mathbf{R} = (R_1 \dots R_N)$ and $\mathbf{S} = A_{N+1,N+1}$, so the inverse takes the form

$$\begin{aligned} \tilde{\mathbf{P}} &= \mathbb{1} + \mathbf{Q} \cdot (\mathbf{S} - \mathbf{R} \cdot \mathbf{Q})^{-1} \cdot \mathbf{R} = \mathbb{1} + \frac{1}{\lambda} \mathbf{Q} \cdot \mathbf{R} \\ &= \begin{pmatrix} 1 + \lambda^{-1} A_{1,N+1} R_1 & \lambda^{-1} A_{1,N+1} R_2 & \dots & \lambda^{-1} A_{1,N+1} R_N \\ \lambda^{-1} A_{2,N+1} R_1 & 1 + \lambda^{-1} A_{2,N+1} R_2 & \dots & \lambda^{-1} A_{2,N+1} R_N \\ \vdots & \vdots & \ddots & \vdots \\ \lambda^{-1} A_{N,N+1} R_1 & \lambda^{-1} A_{N,N+1} R_2 & \dots & 1 + \lambda^{-1} A_{N,N+1} R_N \end{pmatrix} \end{aligned} \quad (\text{A.21})$$

$$\tilde{\mathbf{Q}} = -\mathbf{Q} \cdot (\mathbf{S} - \mathbf{R} \cdot \mathbf{Q})^{-1} = -\frac{1}{\lambda} \mathbf{Q} = -\frac{1}{\lambda} (A_{1,N+1} \dots A_{N,N+1})^T, \quad (\text{A.22})$$

$$\tilde{\mathbf{R}} = -(\mathbf{S} - \mathbf{R} \cdot \mathbf{Q})^{-1} \cdot \mathbf{R} = -\frac{1}{\lambda} \mathbf{R} = -\frac{1}{\lambda} (R_1 \dots R_N), \quad (\text{A.23})$$

$$\tilde{\mathbf{S}} = (\mathbf{S} - \mathbf{R} \cdot \mathbf{Q})^{-1} = \frac{1}{\lambda}, \quad (\text{A.24})$$

where $\lambda \equiv \det(\mathbf{S} - \mathbf{R} \cdot \mathbf{Q}) = \mathbf{S} - \mathbf{R} \cdot \mathbf{Q} = A_{N+1,N+1} - \sum_i R_i A_{i,N+1}$. From equation (A.20) we see that $\lambda = \det(1 + \Delta A^{-1})$. This can also be obtained from the explicit expression (A.13) by expanding around the last row and then the last column. Consequently, using equation (A.11), λ is the ratio of determinants of A' and A :

$$A'^{-1} = A^{-1}(1 + \Delta A^{-1})^{-1} \Rightarrow \frac{\det A'}{\det A} = \frac{\det A^{-1}}{\det A'^{-1}} = \det(1 + \Delta A^{-1}) = \lambda \quad (\text{A.25})$$

Now it becomes clear why the inverse of the matrix A' has to be computed – the terms R_i in the expression for λ depend on all elements $A_{k,i}^{-1}$ of the inverse of A . For an update of A' in turn we will need the inverse A'^{-1} . Using equation (A.11) we finally arrive at

an explicit expression for A'^{-1} :

$$A'^{-1} = A^{-1}(1 + \Delta A^{-1})^{-1} = \left(\begin{array}{ccc|c} & & & -\lambda^{-1}L_1 \\ & & & \vdots \\ & & & -\lambda^{-1}L_N \\ \hline -\lambda^{-1}R_1 & \cdots & -\lambda^{-1}R_N & \lambda^{-1} \end{array} \right), \quad (\text{A.26})$$

where $L_i \equiv \sum_k A_{i,k}^{-1} A_{k,N+1}$.

Let us now count the number of operations required for the calculation of $\det A'$ and A'^{-1} . For λ we need to compute the following quantities:

$$\begin{aligned} R_i = \sum_k A_{N+1,k} A_{k,i}^{-1} : & \quad N^2 \text{ mult. } (N \text{ for each } i), \quad (N-1)N \text{ add. } (N-1 \text{ for each } i) \\ \sum_i R_i A_{i,N+1} : & \quad N \text{ mult.}, \quad N-1 \text{ add.} \end{aligned}$$

So in total, to compute $\lambda = A_{N+1,N+1} - \sum_i R_i A_{i,N+1}$, $N^2 + N$ multiplications and N^2 additions have to be performed. For the inverse matrix we need additionally:

$$\begin{aligned} L_i = \sum_k A_{i,k}^{-1} A_{k,N+1} : & \quad N^2 \text{ mult. } (N \text{ for each } i), \quad (N-1)N \text{ add. } (N-1 \text{ for each } i) \\ \lambda^{-1} : & \quad 1 \text{ mult.} \\ -\lambda^{-1} R_i : & \quad N \text{ mult. } (1 \text{ for each } i) \\ -\lambda^{-1} L_i : & \quad N \text{ mult. } (1 \text{ for each } i) \\ A_{i,j}^{-1} + \lambda^{-1} L_i R_j : & \quad N^2 \text{ mult. } (1 \text{ for each } i \text{ and } j), \quad N^2 \text{ add. } (1 \text{ for each } i \text{ and } j) \end{aligned}$$

In total this makes $2N^2 + 2N + 1$ multiplications and $2N^2 - N$ additions and together with the determinant $3N^2 + 3N + 1$ multiplications and $3N^2 - N$ additions. So the complexity of the algorithm is N^2 and the prefactor is only 3 for both additions and multiplications, which is better than the usual Sherman-Morrison algorithm that has a prefactor of 4 in both cases.

A.3 Removing one row and one column

Assume we want to remove row n and column m from an $N \times N$ matrix A , which inverse and determinant are already known. The resulting $(N-1) \times (N-1)$ matrix A' is extended to an $N \times N$ matrix in a similar manner as before, by replacing the removed elements A_{nj} by δ_{mj} and A_{im} by δ_{in} . Note that extending a matrix by a “unit” row n and a “unit” column m implies extending the inverse matrix by a “unit” row m and “unit” column n (this did not play a role for the previous update, where we had

$m = n$). Again as before (up to a minus sign) we define

$$\Delta \equiv A - A' = \left(\begin{array}{c|c|c} & \vdots & \\ & A_{i,m} & 0 \\ & \vdots & \\ \cdots & A_{n,j} & \cdots \\ \hline & A_{n,m} - 1 & \cdots A_{n,j} \cdots \\ \hline & \vdots & \\ 0 & A_{i,m} & 0 \\ & \vdots & \end{array} \right) \leftarrow n \quad (\text{A.27})$$

\uparrow
 m

and analogous to (A.11),

$$A'^{-1} = (A - \Delta)^{-1} = A^{-1}(1 - \Delta A^{-1})^{-1}. \quad (\text{A.28})$$

Again we want to invert the term in brackets directly. Consider

$$\begin{aligned} \Delta A^{-1} &= \left(\begin{array}{c|c|c} & \vdots & \\ & A_{i,m} & 0 \\ & \vdots & \\ \cdots & A_{n,j} & \cdots \\ \hline & A_{n,m} - 1 & \cdots A_{n,j} \cdots \\ \hline & \vdots & \\ 0 & A_{i,m} & 0 \\ & \vdots & \end{array} \right) \cdot \left(\begin{array}{c} \vdots \\ \cdots A_{i,j}^{-1} \cdots \\ \vdots \\ \cdots A_{m,j}^{-1} \cdots \\ \vdots \\ \cdots A_{i,j}^{-1} \cdots \\ \vdots \end{array} \right) \\ &= \left(\begin{array}{c} \vdots \\ \cdots A_{i,m} A_{m,j}^{-1} \cdots \\ \vdots \\ \cdots \sum_k A_{n,k} A_{k,j}^{-1} - A_{m,j}^{-1} \cdots \\ \vdots \\ \cdots A_{i,m} A_{m,j}^{-1} \cdots \\ \vdots \end{array} \right) \leftarrow n \end{aligned} \quad (\text{A.29})$$

where the m th column of matrix Δ and the m th row of matrix A^{-1} were highlighted, to emphasise that the only contribution to product elements $(\Delta A^{-1})_{ij}$ in the rows $i \neq n$ comes from products $A_{i,m} A_{m,j}^{-1}$ with $i \neq n$. The n th row of matrix Δ (also highlighted)

multiplied with A^{-1} gives the n th row of the matrix ΔA^{-1} which has the form,

$$\sum_k A_{n,k} A_{k,j}^{-1} - A_{m,j}^{-1} = \delta_{nj} - A_{m,j}^{-1}. \quad (\text{A.30})$$

Using this identity we can rewrite (A.29) as

$$\Delta A^{-1} = \left(\begin{array}{ccc} \vdots & & \\ \cdots & A_{i,m} A_{m,j}^{-1} & \cdots \\ \vdots & & \\ \cdots & \delta_{nj} - A_{m,j}^{-1} & \cdots \\ \vdots & & \\ \cdots & A_{i,m} A_{m,j}^{-1} & \cdots \\ \vdots & & \end{array} \right) \leftarrow n \quad (\text{A.31})$$

and consequently

$$1 - \Delta A^{-1} = \left(\begin{array}{ccc} \vdots & & \\ \cdots & \delta_{ij} - A_{i,m} A_{m,j}^{-1} & \cdots \\ \vdots & & \\ \cdots & A_{m,j}^{-1} & \cdots \\ \vdots & & \\ \cdots & \delta_{ij} - A_{i,m} A_{m,j}^{-1} & \cdots \\ \vdots & & \end{array} \right) \leftarrow n \quad (\text{A.32})$$

So the matrix $1 - \Delta A^{-1}$ consists of elements of the form $\delta_{ij} - A_{i,m} A_{m,j}^{-1}$, except row n where the elements are of the form $A_{m,j}^{-1}$. The inverse of this expression, i.e. a matrix M with $\sum_k (1 - \Delta A^{-1})_{ik} M_{kj} = \delta_{ij}$ can be obtained by solving the following set of equations:

$$\sum_k (\delta_{ik} - A_{i,m} A_{m,k}^{-1}) M_{k,j} = \delta_{ij} \quad \text{for } i \neq n, \quad (\text{A.33})$$

$$\sum_k A_{m,k}^{-1} M_{k,j} = \delta_{ij} \quad \text{for } i = n. \quad (\text{A.34})$$

From (A.33) we obtain for $i \neq n$

$$M_{i,j} - A_{i,m} \sum_k A_{m,k}^{-1} M_{k,j} = \delta_{ij} \quad (\text{A.35})$$

and plugging in the identity $\sum_k A_{m,k}^{-1} M_{k,j} = \delta_{nj}$ from (A.34) we arrive at

$$M_{i,j} - A_{i,m} \delta_{nj} = \delta_{ij} \Leftrightarrow M_{i,j} = \delta_{ij} + A_{i,m} \delta_{nj}, \quad (\text{A.36})$$

for $i \neq n$. To determine the values of the remaining elements $M_{n,j}$ we expand (A.34) as follows,

$$\delta_{nj} = \sum_{k \neq n} A_{m,k}^{-1} M_{k,j} + A_{m,n}^{-1} M_{n,j}, \quad (\text{A.37})$$

and then replace $M_{k,j}$ in the sum by the result from (A.36):

$$\delta_{nj} = \sum_{k \neq n} A_{m,k}^{-1} (\delta_{kj} + A_{k,m} \delta_{nj}) + A_{m,n}^{-1} M_{n,j}, \quad (\text{A.38})$$

which we can do since the sum goes over all indices except n . It is now convenient to consider two cases separately, $j = n$ and $j \neq n$. For $j = n$,

$$\begin{aligned} \delta_{nn} = 1 &= \sum_{k \neq n} A_{m,k}^{-1} (\delta_{kn} + A_{k,m} \delta_{nn}) + A_{m,n}^{-1} M_{n,n} \\ &= \sum_{k \neq n} A_{m,k}^{-1} (0 + A_{k,m}) + A_{m,n}^{-1} M_{n,n} \\ &= \sum_{k \neq n} A_{m,k}^{-1} A_{k,m} + A_{m,n}^{-1} M_{n,n}. \end{aligned} \quad (\text{A.39})$$

Using

$$\sum_k A_{i,k}^{-1} A_{k,j} = \delta_{ij} \Rightarrow \sum_{k \neq n} A_{m,k}^{-1} A_{k,m} = \delta_{mm} - A_{m,n}^{-1} A_{n,m} = 1 - A_{m,n}^{-1} A_{n,m} \quad (\text{A.40})$$

equation (A.39) yields

$$1 = 1 - A_{m,n}^{-1} A_{n,m} + A_{m,n}^{-1} M_{n,n} \Leftrightarrow M_{n,n} = A_{n,m}, \quad (\text{A.41})$$

provided $A_{m,n}^{-1} \neq 0$. However this is always the case for a non-singular matrix $1 - \Delta A^{-1}$, since if $A_{m,n}^{-1} = 0$, the elements of the n th column of $1 - \Delta A^{-1}$ are all 0. For the second case, $j \neq n$, (A.38) yields

$$0 = \sum_{k \neq n} A_{m,k}^{-1} (\delta_{kj} + A_{k,m} \cdot 0) + A_{m,n}^{-1} M_{n,j} = A_{m,j}^{-1} + A_{m,n}^{-1} M_{n,j}. \quad (\text{A.42})$$

The sum could be performed as usual, since there exists a $k \neq n$ such that $\delta_{kj} = 1$ for $j \neq n$. Altogether,

$$M_{n,j} = -\frac{A_{m,j}^{-1}}{A_{m,n}^{-1}} \quad \text{for } j \neq n. \quad (\text{A.43})$$

Having calculated all elements of $M \equiv (1 - \Delta A^{-1})^{-1}$ we can write this matrix out explicitly,

$$M = (1 - \Delta A^{-1})^{-1} = \left(\begin{array}{ccc|ccc} 1 & & 0 & \vdots & & \\ & \ddots & & A_{i,m} & & 0 \\ 0 & & 1 & \vdots & & \\ \hline \dots & -\frac{A_{m,j}^{-1}}{A_{m,n}^{-1}} & \dots & A_{n,m} & \dots & -\frac{A_{m,j}^{-1}}{A_{m,n}^{-1}} & \dots \\ \hline & & & \vdots & 1 & & 0 \\ & 0 & & A_{i,m} & & \ddots & \\ & & & \vdots & 0 & & 1 \end{array} \right) \leftarrow n \quad (\text{A.44})$$

\uparrow
 n

The determinant of M is the ratio of determinants of A and A' . It can be either obtained by expanding M , first around the n th row and then each of the resulting matrices around the rows that contain only one non-zero element, or by applying formula (A.20) for the determinant of a partitioned matrix. Here the latter is demonstrated. We partition M as follows: Let \mathbf{P} be the $n \times n$ block in the upper left corner, \mathbf{S} the $(N - n) \times (N - n)$ unit matrix in the lower right corner and \mathbf{Q} and \mathbf{R} the $n \times (N - n)$ and the $(N - n) \times n$ matrices in the upper right and lower left corner respectively. All elements of \mathbf{Q} are 0 except the last row, with elements $-\frac{A_{m,j}^{-1}}{A_{m,n}^{-1}}$ and similar for \mathbf{R} where the non-zero elements $A_{i,m}$ are in the last column. So

$$\det M = \det \mathbf{S} \det(\mathbf{P} - \mathbf{Q} \mathbf{S}^{-1} \mathbf{R}) = \det(\mathbf{P} - \mathbf{Q} \cdot \mathbf{R}). \quad (\text{A.45})$$

The term $\mathbf{Q} \cdot \mathbf{R}$ is an $n \times n$ matrix with only one non-zero element,

$$-\sum_{j=n+1}^N \frac{A_{m,j}^{-1}}{A_{m,n}^{-1}} A_{j,m},$$

in the lower right corner. So the matrix $\tilde{\mathbf{M}} \equiv \mathbf{P} - \mathbf{Q} \cdot \mathbf{R}$ has the form

$$\tilde{\mathbf{M}} = \left(\begin{array}{ccc|ccc} & & & \vdots & & \\ & \mathbb{1} & & A_{i,m} & & \\ & & & \vdots & & \\ \hline \dots & -\frac{A_{m,j}^{-1}}{A_{m,n}^{-1}} & \dots & A_{n,m} + \sum_{j=n+1}^N \frac{A_{m,j}^{-1}}{A_{m,n}^{-1}} A_{j,m} & & \end{array} \right). \quad (\text{A.46})$$

To obtain the determinant of $\tilde{\mathbf{M}}$ we apply (A.20) again,

$$\det \tilde{\mathbf{M}} = \det \tilde{\mathbf{P}} \det(\tilde{\mathbf{S}} - \tilde{\mathbf{R}}\tilde{\mathbf{P}}^{-1}\tilde{\mathbf{Q}}) = \det(\tilde{\mathbf{S}} - \tilde{\mathbf{R}} \cdot \tilde{\mathbf{Q}}), \quad (\text{A.47})$$

where the partitioning is analogous to the one used for the first update,

$$\tilde{\mathbf{P}} = \mathbb{1}_{n-1}, \quad (\text{A.48})$$

$$\tilde{\mathbf{S}} = A_{n,m} + \sum_{j=n+1}^N \frac{A_{m,j}^{-1}}{A_{m,n}^{-1}} A_{j,m}, \quad (\text{A.49})$$

$$\tilde{\mathbf{R}} = (\dots, -\frac{A_{m,j}^{-1}}{A_{m,n}^{-1}}, \dots), \quad (\text{A.50})$$

$$\tilde{\mathbf{Q}} = (\dots, A_{i,m}, \dots)^T. \quad (\text{A.51})$$

Altogether,

$$\begin{aligned} \det M = \det \tilde{\mathbf{M}} &= A_{n,m} + \sum_{j=n+1}^N \frac{A_{m,j}^{-1}}{A_{m,n}^{-1}} A_{j,m} + \sum_{j=1}^{n-1} \frac{A_{m,j}^{-1}}{A_{m,n}^{-1}} A_{j,m} \\ &= A_{n,m} + \sum_{j \neq n} \frac{A_{m,j}^{-1} A_{j,m}}{A_{m,n}^{-1}} \\ &= A_{n,m} + \frac{1 - A_{m,n}^{-1} A_{n,m}}{A_{m,n}^{-1}} \\ &= \frac{1}{A_{m,n}^{-1}} \end{aligned} \quad (\text{A.52})$$

and thus

$$\frac{\det A'}{\det A} = \frac{\det A^{-1}}{\det A'^{-1}} = \frac{1}{\det M} = A_{m,n}^{-1}. \quad (\text{A.53})$$

What remains is to determine $A'^{-1} = A^{-1}(1 - \Delta A^{-1})^{-1}$ by multiplying out the according matrices. We obtain

$$A'_{i,j}{}^{-1} = \sum_k A_{i,k}^{-1} (\delta_{kj} - \frac{A_{m,j}^{-1}}{A_{m,n}^{-1}} \delta_{kn}) = A_{i,j}^{-1} - A_{i,n}^{-1} \frac{A_{m,j}^{-1}}{A_{m,n}^{-1}} \quad \text{for } j \neq n, \quad (\text{A.54})$$

$$A'_{i,j}{}^{-1} = \sum_k A_{i,k}^{-1} A_{k,m} = \delta_{im} \quad \text{for } j = n. \quad (\text{A.55})$$

Note that for $i = m$ (A.54) simplifies to

$$A'_{m,j}{}^{-1} = A_{m,j}^{-1} - A_{m,n}^{-1} \frac{A_{m,j}^{-1}}{A_{m,n}^{-1}} = 0, \quad (\text{A.56})$$

so indeed A'^{-1} has “unit” row m and “unit” column n . These will be dropped at the end of the procedure, yielding an updated matrix of size $(N - 1) \times (N - 1)$. Explicitly:

$$A'^{-1} = \left(\begin{array}{ccc|c|ccc} & & & \vdots & & & \\ & A_{i,j}^{-1} - A_{i,n}^{-1} \frac{A_{m,j}^{-1}}{A_{m,n}^{-1}} & & 0 & A_{i,j}^{-1} - A_{i,n}^{-1} \frac{A_{m,j}^{-1}}{A_{m,n}^{-1}} & & \\ & \vdots & & \vdots & & & \\ \hline \dots & 0 & \dots & 1 & \dots & 0 & \dots \\ \hline & A_{i,j}^{-1} - A_{i,n}^{-1} \frac{A_{m,j}^{-1}}{A_{m,n}^{-1}} & & 0 & A_{i,j}^{-1} - A_{i,n}^{-1} \frac{A_{m,j}^{-1}}{A_{m,n}^{-1}} & & \\ & \vdots & & \vdots & & & \end{array} \right) \leftarrow m \quad (\text{A.57})$$

\uparrow
 n

Let us now count the number of operations for this update. There are no operations required for the determinant. For each of the $(N - 1)^2$ non-trivial elements of A'^{-1} we need to perform two multiplications and one addition. This can be performed even faster, if we first calculate and store the $N - 1$ values of $\frac{A_{m,j}^{-1}}{A_{m,n}^{-1}}$ for each $j \neq n$, which reduces the number of required multiplications per element of A'^{-1} to one. The total number of multiplications is thus $N - 1 + (N - 1)^2 = N^2 - N$ and the total number of additions is $(N - 1)^2 = N^2 - 2N + 1$, both of order N^2 with prefactor 1. This update is three times faster than the one that adds a row and a column.

A.4 Changing the elements of one row

The last update changes all elements in row n of A , for some n . The size of the matrix remains unchanged. With the Sherman-Morrison scheme, this update requires order $2N^2$ additions and $2N^2$ multiplications. Here we apply a method, analogous to the ones used for the previous updates and count the number of operations. First write

$$\Delta \equiv A' - A = \left(\begin{array}{ccc|ccc} 0 & \dots & 0 & & & \\ \vdots & & \vdots & & & \\ 0 & \dots & 0 & & & \\ \hline \Delta_1 & \dots & \Delta_N & & & \\ \hline 0 & \dots & 0 & & & \\ \vdots & & \vdots & & & \\ 0 & \dots & 0 & & & \end{array} \right), \leftarrow n \quad (\text{A.58})$$

where $\Delta_j \equiv A'_{n,j} - A_{n,j}$, and analogous to (A.11),

$$A'^{-1} = (A + \Delta)^{-1} = A^{-1}(1 + \Delta A^{-1})^{-1}. \quad (\text{A.59})$$

It is easy to see that all entries of the matrix ΔA^{-1} are 0, except for row n where the entries are

$$R_j \equiv \sum_k \Delta_k A_{k,j}^{-1} = \sum_k (A'_{n,k} - A_{n,k}) A_{k,j}^{-1} = \sum_k A'_{n,k} A_{k,j}^{-1} - \delta_{nj}. \quad (\text{A.60})$$

From this we get

$$1 + \Delta A^{-1} = \begin{pmatrix} 1 & 0 & 0 & \cdots & 0 \\ & \ddots & \vdots & & \vdots \\ 0 & 1 & 0 & \cdots & 0 \\ \hline \cdots & \sum_k A'_{n,k} A_{k,j}^{-1} & \cdots & & \\ \hline 0 & \cdots & 0 & 1 & 0 \\ \vdots & & \vdots & & \ddots \\ 0 & \cdots & 0 & 0 & 1 \end{pmatrix} \leftarrow n \quad (\text{A.61})$$

Let us invert this matrix. For lucidity we introduce the abbreviation $R'_j \equiv \sum_k A'_{n,k} A_{k,j}^{-1}$. Since $1 + \Delta A^{-1}$ varies from the unit matrix only in row n , then so does its inverse, or in other words

$$(1 + \Delta A^{-1})_{i,j}^{-1} = \delta_{ij} \quad \text{for } i \neq n. \quad (\text{A.62})$$

To obtain the elements $(1 + \Delta A^{-1})_{n,j}^{-1}$ consider

$$\delta_{nj} = \sum_k R'_k (1 + \Delta A^{-1})_{k,j}^{-1} = \sum_{k \neq n} R'_k \delta_{k,j} + R'_n (1 + \Delta A^{-1})_{n,j}^{-1}. \quad (\text{A.63})$$

Again there are two cases $j = n$ and $j \neq n$. We deal with $j = n$ first and obtain,

$$\delta_{nn} = 1 = \sum_{k \neq n} R'_k \delta_{k,n} + R'_n (1 + \Delta A^{-1})_{n,n}^{-1} = R'_n (1 + \Delta A^{-1})_{n,n}^{-1}. \quad (\text{A.64})$$

So, provided $R'_n \neq 0$,

$$(1 + \Delta A^{-1})_{n,n}^{-1} = \frac{1}{R'_n}, \quad (\text{A.65})$$

but this is always the case for a non-singular matrix A' , since $R'_n = 0$ would imply that the n th column of $1 + \Delta A^{-1}$ has only zero entries. For the case $j \neq n$:

$$\delta_{nj} = 0 = \sum_{k \neq n} R'_k \delta_{k,j} + R'_n (1 + \Delta A^{-1})_{n,j}^{-1} = R'_j + R'_n (1 + \Delta A^{-1})_{n,j}^{-1} \quad (\text{A.66})$$

and hence

$$(1 + \Delta A^{-1})_{n,j}^{-1} = -\frac{R'_j}{R'_n}. \quad (\text{A.67})$$

Explicitly:

$$(1 + \Delta A^{-1})^{-1} = \begin{pmatrix} 1 & & 0 & 0 & \cdots & 0 \\ & \ddots & & \vdots & & \vdots \\ 0 & & 1 & 0 & \cdots & 0 \\ \cdots & -\frac{R'_j}{R'_n} & \cdots & \frac{1}{R'_n} & \cdots & -\frac{R'_j}{R'_n} & \cdots \\ 0 & & \cdots & 0 & 1 & 0 \\ \vdots & & & \vdots & & \ddots \\ 0 & & \cdots & 0 & 0 & 1 \end{pmatrix} \leftarrow n \quad (\text{A.68})$$

The determinant of this matrix is simply $\frac{1}{R'_n}$ as one can see by expanding around row n (after removing row n , column n has only zero entries, so all minors will be zero except the one where row n and column n are removed, in which case the minor is the determinant of the unit matrix, i.e. 1). So the ratio of determinants of A' and A is

$$\frac{\det A'}{\det A} = \frac{\det A^{-1}}{\det A'^{-1}} = \frac{1}{\det(1 + \Delta A^{-1})^{-1}} = R'_n. \quad (\text{A.69})$$

Now A'^{-1} can be obtained,

$$A'^{-1} = A^{-1}(1 + \Delta A^{-1})^{-1} = \left(\begin{array}{c|c} A_{i,j}^{-1} - A_{i,n}^{-1} \frac{R'_j}{R'_n} & \begin{array}{c} \vdots \\ A_{i,n}^{-1} \frac{1}{R'_n} \\ \vdots \end{array} \\ \hline & A_{i,j}^{-1} - A_{i,n}^{-1} \frac{R'_j}{R'_n} \end{array} \right) \quad (\text{A.70})$$

\uparrow
 n

Finally we need to count the number of operations. Each $R'_j \equiv \sum_k A'_{n,k} A_{k,j}^{-1}$ involves N multiplications and $N - 1$ additions, which makes N^2 multiplications and $(N - 1)N$ additions in total. Then we need to divide $A_{i,n}^{-1}$ through R'_n for each i . This requires N multiplications. After this, for all i and $j \neq n$ we need to multiply $\frac{A_{i,n}^{-1}}{R'_n}$ by R'_j . The total number of multiplications is thus $N(N - 1)$. Finally we need $N(N - 1)$ additions to obtain the elements $A_{i,j}^{-1} - A_{i,n}^{-1} \frac{R'_j}{R'_n}$. Altogether we have $2N^2 - 2N$ additions and $N^2 + N + N(N - 1) = 2N^2$ multiplications. This is of order N^2 with a prefactor of 2 for both additions and multiplications, which is the same as we get using the Sherman-Morrison method.

Bibliography

- [1] L. Pitaevskii and S. Stringari, *Bose-Einstein Condensation*. Oxford University Press, 2003.
- [2] C. J. Pethick and H. Smith, *Bose-Einstein Condensation in Dilute Gases*. Cambridge University Press, 2002.
- [3] S. Giorgini, L. P. Pitaevskii, and S. Stringari, “Theory of ultracold atomic Fermi gases,” *Rev. Mod. Phys.* **80** no. 4, (Oct, 2008) 1215–1274, [arXiv:0706.3360v2](#).
- [4] I. Bloch, J. Dalibard, and W. Zwerger, “Many-body physics with ultracold gases,” *Rev. Mod. Phys.* **80** no. 3, (Jul, 2008) 885–964, [arXiv:0704.3011](#).
- [5] O. Goulko and M. Wingate, “Monte Carlo study of a Fermi gas with infinite scattering length,” *PoS LAT2009* (2009) 062, [arXiv:0910.3909](#).
- [6] O. Goulko and M. Wingate, “Thermodynamics of balanced and slightly spin-imbalanced Fermi gases at unitarity,” *Phys. Rev. A* **82** no. 5, (Nov, 2010) 053621, [arXiv:1008.3348](#).
- [7] O. Goulko and M. Wingate, “The imbalanced Fermi gas at unitarity,” *PoS LAT2010* (2010) 187, [arXiv:1011.0312](#).
- [8] O. Goulko, F. Chevy, and C. Lobo, “Collision of two spin polarized fermionic clouds,” to appear in *Phys. Rev. A* (Jun, 2011) , [arXiv:1106.5773](#).
- [9] J. J. Sakurai, *Modern Quantum Mechanics*. The Benjamin/Cummings Publishing Company, Inc., 1985.
- [10] L. D. Landau and E. M. Lifshitz, *Quantum Mechanics: Non-Relativistic Theory*, vol. 3 of *Landau and Lifshitz: Course of Theoretical Physics*. Pergamon Press, 1977.
- [11] W. Ketterle and M. W. Zwierlein, “Making, probing and understanding ultracold Fermi gases,” in *Ultra-Cold Fermi Gases (Proceedings of the International School of Physics “Enrico Fermi”, Course CLXIV)*, M. Inguscio, W. Ketterle, and C. Salomon, eds., pp. 95–288. IOS Press, 2007. [arXiv:0801.2500](#).

- [12] T. Köhler, K. Góral, and P. S. Julienne, “Production of cold molecules via magnetically tunable Feshbach resonances,” *Rev. Mod. Phys.* **78** no. 4, (Dec, 2006) 1311–1361, [cond-mat/0601420](#).
- [13] S. Stringari, “Dynamics and superfluidity of an ultracold Fermi gas,” in *Ultra-Cold Fermi Gases (Proceedings of the International School of Physics “Enrico Fermi”, Course CLXIV)*, M. Inguscio, W. Ketterle, and C. Salomon, eds., pp. 53–94. IOS Press, 2007. [cond-mat/0702526](#).
- [14] D. M. Eagles, “Possible Pairing without Superconductivity at Low Carrier Concentrations in Bulk and Thin-Film Superconducting Semiconductors,” *Phys. Rev.* **186** (Oct, 1969) 456–463.
- [15] P. Nikolić and S. Sachdev, “Renormalization-group fixed points, universal phase diagram, and $1/N$ expansion for quantum liquids with interactions near the unitarity limit,” *Phys. Rev. A* **75** no. 3, (Mar, 2007) 033608, [cond-mat/0609106](#).
- [16] R. Haussmann, W. Rantner, S. Cerrito, and W. Zwerger, “Thermodynamics of the BCS-BEC crossover,” *Phys. Rev. A* **75** no. 2, (Feb, 2007) 023610, [cond-mat/0608282](#).
- [17] Y. Nishida and D. T. Son, “Fermi gas near unitarity around four and two spatial dimensions,” *Phys. Rev. A* **75** no. 6, (Jun, 2007) 063617, [cond-mat/0607835](#).
- [18] Y. Nishida, “Unitary Fermi gas at finite temperature in the ϵ expansion,” *Phys. Rev. A* **75** no. 6, (Jun, 2007) 063618, [cond-mat/0608321](#).
- [19] Y. Nishida and D. T. Son, “Unitary Fermi gas, epsilon expansion, and nonrelativistic conformal field theories,” in *The BCS-BEC crossover and the Unitary Fermi Gas*, W. Zwerger, ed., Lecture Notes in Physics. Springer-Verlag New York, LLC, 2011. [arXiv:1004.3597](#).
- [20] H. Hu, X.-J. Liu, and P. D. Drummond, “Temperature of a trapped unitary Fermi gas at finite entropy,” *Phys. Rev. A* **73** no. 2, (Feb, 2006) 023617, [cond-mat/0509274](#).
- [21] D. Lee and T. Schäfer, “Cold dilute neutron matter on the lattice. II. Results in the unitary limit,” *Phys. Rev. C* **73** no. 1, (Jan, 2006) 015202, [nucl-th/0509018](#).
- [22] V. K. Akkineni, D. M. Ceperley, and N. Trivedi, “Pairing and superfluid properties of dilute fermion gases at unitarity,” *Phys. Rev. B* **76** no. 16, (Oct, 2007) 165116, [cond-mat/0608154](#).

- [23] A. Bulgac, J. E. Drut, and P. Magierski, “Quantum Monte Carlo simulations of the BCS-BEC crossover at finite temperature,” *Phys. Rev. A* **78** no. 2, (Aug, 2008) 023625, [arXiv:0803.3238](#).
- [24] A. Bulgac, J. E. Drut, and P. Magierski, “Spin 1/2 Fermions in the Unitary Regime: A Superfluid of a New Type,” *Phys. Rev. Lett.* **96** no. 9, (Mar, 2006) 090404, [cond-mat/0505374](#).
- [25] A. Bulgac, J. E. Drut, and P. Magierski, “Thermodynamics of a Trapped Unitary Fermi Gas,” *Phys. Rev. Lett.* **99** no. 12, (Sep, 2007) 120401, [cond-mat/0701786](#).
- [26] E. Burovski, N. Prokof’ev, B. Svistunov, and M. Troyer, “The Fermi-Hubbard model at unitarity,” *New J. Phys.* **8** no. 8, (Aug, 2006) 153, [cond-mat/0605350](#).
- [27] L. Radzihovsky and D. E. Sheehy, “Imbalanced Feshbach-resonant Fermi gases,” *Rep. Prog. Phys.* **73** no. 7, (Jul, 2010) 076501, [arXiv:0911.1740](#).
- [28] F. Chevy and C. Mora, “Ultra-cold polarized Fermi gases,” *Rep. Prog. Phys.* **73** no. 11, (Nov, 2010) 112401, [arXiv:1003.0801](#).
- [29] M. W. Zwierlein, A. Schirotzek, C. H. Schunck, and W. Ketterle, “Fermionic superfluidity with imbalanced spin populations,” *Science* **311** no. 5760, (Jan, 2006) 492–496, [cond-mat/0511197](#).
- [30] S. Nascimbène, N. Navon, K. J. Jiang, L. Tarruell, M. Teichmann, J. McKeever, F. Chevy, and C. Salomon, “Collective Oscillations of an Imbalanced Fermi Gas: Axial Compression Modes and Polaron Effective Mass,” *Phys. Rev. Lett.* **103** no. 17, (Oct, 2009) 170402, [arXiv:0907.3032](#).
- [31] G. B. Partridge, W. Li, R. I. Kamar, Y. an Liao, and R. G. Hulet, “Pairing and Phase Separation in a Polarized Fermi Gas,” *Science* **311** no. 5760, (Jan, 2006) 503, [cond-mat/0511752](#).
- [32] M. M. Parish and D. A. Huse, “Evaporative depolarization and spin transport in a unitary trapped Fermi gas,” *Phys. Rev. A* **80** no. 6, (Dec, 2009) 063605, [arXiv:0903.5324](#).
- [33] X. Du, L. Luo, B. Clancy, and J. E. Thomas, “Observation of anomalous spin segregation in a trapped Fermi gas,” *Phys. Rev. Lett.* **101** no. 15, (Oct, 2008) 150401, [arXiv:0805.1036](#).
- [34] X. Du, Y. Zhang, J. Petricka, and J. E. Thomas, “Controlling spin current in a trapped Fermi gas,” *Phys. Rev. Lett.* **103** no. 1, (Jul, 2009) 010401, [arXiv:0901.3702](#).

- [35] F. Piéchon, J. N. Fuchs, and F. Laloë, “Cumulative identical spin rotation effects in collisionless trapped atomic gases,” *Phys. Rev. Lett.* **102** no. 21, (May, 2009) 215301, [arXiv:0901.4008](#).
- [36] R. A. Duine, M. Polini, A. Raoux, H. T. C. Stoof, and G. Vignale, “Spin drag in ultracold Fermi mixtures with repulsive interactions,” *New J. Phys.* **13** no. 4, (Apr, 2011) 045010, [arXiv:1012.3827](#).
- [37] A. Sommer, M. Ku, G. Roati, and M. W. Zwierlein, “Universal Spin Transport in a Strongly Interacting Fermi Gas,” *Nature* **472** (Apr, 2011) 201–204, [arXiv:1101.0780](#).
- [38] G. M. Bruun, “Spin diffusion in Fermi gases,” *New J. Phys.* **13** no. 3, (Mar, 2011) 035005, [arXiv:1012.1607](#).
- [39] S. A. Wolf, D. D. Awschalom, R. A. Buhrman, J. M. Daughton, S. von Molnár, M. L. Roukes, A. Y. Chtchelkanova, and D. M. Treger, “Spintronics: A Spin-Based Electronics Vision for the Future,” *Science* **294** no. 5546, (Nov, 2001) 1488–1495.
- [40] A. Sommer, M. Ku, and M. W. Zwierlein, “Spin transport in polaronic and superfluid Fermi gases,” *New J. Phys.* **13** no. 5, (May, 2011) 055009, [arXiv:1103.2337](#).
- [41] J.-W. Chen and D. B. Kaplan, “Lattice theory for low energy fermions at nonzero chemical potential,” *Phys. Rev. Lett.* **92** no. 25, (Jun, 2004) 257002, [hep-lat/0308016](#).
- [42] D. Lee and R. Thomson, “Temperature-dependent errors in nuclear lattice simulations,” *Phys. Rev. C* **75** no. 6, (Jun, 2007) 064003, [nucl-th/0701048](#).
- [43] E. Braaten, M. Kusunoki, and D. Zhang, “Scattering models for ultracold atoms,” *Annals Phys.* **323** (Jul, 2008) 1770–1815, [arXiv:0709.0499](#).
- [44] M. E. Peskin and D. V. Schroeder, *An Introduction to Quantum Field Theory*. Westview Press, 1995.
- [45] E. M. Lifshitz and L. P. Pitaevskii, *Statistical Physics. Part 2, Theory of the condensed state*, vol. 9 of *Landau and Lifshitz: Course of Theoretical Physics*. Pergamon Press, 1980.
- [46] Y. Castin. Private communication.
- [47] Y. Castin and F. Werner, “The Unitary Gas and its Symmetry Properties,” in *The BCS-BEC crossover and the Unitary Fermi Gas*, W. Zwerger, ed., Lecture Notes in Physics. Springer-Verlag New York, LLC, 2011. [arXiv:1103.2851](#).

- [48] Y. Castin, “Basic theory tools for degenerate Fermi gases,” in *Ultra-Cold Fermi Gases (Proceedings of the International School of Physics “Enrico Fermi”, Course CLXIV)*, M. Inguscio, W. Ketterle, and C. Salomon, eds., pp. 289–349. IOS Press, 2007. `cond-mat/0612613`.
- [49] E. M. Lifshitz and L. P. Pitaevskii, *Physical Kinetics*, vol. 10 of *Landau and Lifshitz: Course of Theoretical Physics*. Pergamon Press, 1981.
- [50] A. N. Rubtsov, V. V. Savkin, and A. I. Lichtenstein, “Continuous-time quantum Monte Carlo method for fermions,” *Phys. Rev. B* **72** no. 3, (Jul, 2005) 035122, `cond-mat/0411344`.
- [51] M. Campostrini, M. Hasenbusch, A. Pelissetto, and E. Vicari, “Theoretical estimates of the critical exponents of the superfluid transition in ^4He by lattice methods,” *Phys. Rev. B* **74** no. 14, (Oct, 2006) 144506.
- [52] A. Pelissetto and E. Vicari, “Critical phenomena and renormalization-group theory,” *Phys. Rept.* **368** no. 6, (Oct, 2002) 549 – 727, `cond-mat/0012164`.
- [53] M. N. Barber, “Finite-size scaling,” in *Phase Transitions and Critical Phenomena*, C. Domb and J. L. Lebowitz, eds., vol. 8, pp. 145–266. Academic Press, 1983.
- [54] J. G. Brankov, *Introduction to Finite-Size Scaling*. Leuven University Press, 1996.
- [55] D. Toussaint, “Simulating QCD at finite density,” *Nucl. Phys. B (Proc. Suppl.)* **17** (Sep, 1990) 248 – 251.
- [56] S. Nascimbène, N. Navon, S. Pilati, F. Chevy, S. Giorgini, A. Georges, and C. Salomon, “Fermi-Liquid Behavior of the Normal Phase of a Strongly Interacting Gas of Cold Atoms,” *Phys. Rev. Lett.* **106** no. 21, (May, 2011) 215303, `arXiv:1012.4664`.
- [57] Q. Chen, J. Stajic, S. Tan, and K. Levin, “BCS-BEC crossover: From high temperature superconductors to ultracold superfluids,” *Phys. Rep.* **412** no. 1, (Jun, 2005) 1 – 88, `cond-mat/0404274`.
- [58] T. DeGrand and C. DeTar., *Lattice Methods for Quantum Chromodynamics*. World Scientific, 2006.
- [59] S. Tan, “Energetics of a strongly correlated Fermi gas,” *Ann. Phys.* **323** no. 12, (Dec, 2008) 2952 – 2970, `cond-mat/0505200`.
- [60] S. Tan, “Large momentum part of a strongly correlated Fermi gas,” *Ann. Phys.* **323** no. 12, (Dec, 2008) 2971 – 2986, `cond-mat/0508320`.

- [61] S. Tan, “Generalized virial theorem and pressure relation for a strongly correlated Fermi gas,” *Ann. Phys.* **323** no. 12, (Dec, 2008) 2987 – 2990, [arXiv:0803.0841](#).
- [62] E. Braaten, “Universal Relations for Fermions with Large Scattering Length,” in *The BCS-BEC crossover and the Unitary Fermi Gas*, W. Zwerger, ed., Lecture Notes in Physics. Springer-Verlag New York, LLC, 2011. [arXiv:1008.2922](#).
- [63] F. Werner and Y. Castin, “Exact relations for quantum-mechanical few-body and many-body problems with short-range interactions in two and three dimensions,” (Jan, 2010) , [arXiv:1001.0774](#).
- [64] E. Burovski, E. Kozik, N. Prokof’ev, B. Svistunov, and M. Troyer, “Critical Temperature Curve in BEC-BCS Crossover,” *Phys. Rev. Lett.* **101** no. 9, (Aug, 2008) 090402, [arXiv:0805.3047](#).
- [65] T. Abe and R. Seki, “From low-density neutron matter to the unitary limit,” *Phys. Rev. C* **79** no. 5, (May, 2009) 054003, [arXiv:0708.2524](#).
- [66] T. Abe and R. Seki, “Lattice calculation of thermal properties of low-density neutron matter with pionless NN effective field theory,” *Phys. Rev. C* **79** no. 5, (May, 2009) 054002, [arXiv:0708.2523](#).
- [67] H. Dong, L.-W. Siu, T. T. S. Kuo, and R. Machleidt, “Unitarity potentials and neutron matter at the unitary limit,” *Phys. Rev. C* **81** no. 3, (Mar, 2010) 034003, [arXiv:0912.0273](#).
- [68] J. Carlson, S.-Y. Chang, V. R. Pandharipande, and K. E. Schmidt, “Superfluid Fermi Gases with Large Scattering Length,” *Phys. Rev. Lett.* **91** no. 5, (Jul, 2003) 050401, [physics/0303094](#).
- [69] G. E. Astrakharchik, J. Boronat, J. Casulleras, and S. Giorgini, “Equation of State of a Fermi Gas in the BEC-BCS Crossover: A Quantum Monte Carlo Study,” *Phys. Rev. Lett.* **93** no. 20, (Nov, 2004) 200404, [cond-mat/0406113](#).
- [70] A. Gezerlis and J. Carlson, “Strongly paired fermions: Cold atoms and neutron matter,” *Phys. Rev. C* **77** no. 3, (Mar, 2008) 032801, [arXiv:0711.3006](#).
- [71] J. T. Stewart, J. P. Gaebler, C. A. Regal, and D. S. Jin, “Potential Energy of a ^{40}K Fermi Gas in the BCS-BEC Crossover,” *Phys. Rev. Lett.* **97** no. 22, (Nov, 2006) 220406, [cond-mat/0607776](#).
- [72] L. Luo and J. E. Thomas, “Thermodynamic Measurements in a Strongly Interacting Fermi Gas,” *J. Low Temp. Phys.* **154** (Jan, 2009) 1–29, [arXiv:0811.1159](#).

- [73] F. Palestini, A. Perali, P. Pieri, and G. C. Strinati, “Temperature and coupling dependence of the universal contact intensity for an ultracold Fermi gas,” *Phys. Rev. A* **82** no. 2, (Aug, 2010) 021605, [arXiv:1005.1158](#).
- [74] T. Enss, R. Haussmann, and W. Zwerger, “Viscosity and scale invariance in the unitary Fermi gas,” *Annals Phys.* **326** no. 3, (Mar, 2011) 770 – 796, [arXiv:1008.0007](#).
- [75] H. Hu, X.-J. Liu, and P. D. Drummond, “Universal contact of strongly interacting fermions at finite temperatures,” *New J. Phys.* **13** no. 3, (Mar, 2011) 035007, [arXiv:1011.3845](#).
- [76] J. E. Drut, T. A. Lähde, and T. Ten, “Momentum Distribution and Contact of the Unitary Fermi Gas,” *Phys. Rev. Lett.* **106** no. 20, (May, 2011) 205302, [arXiv:1012.5474](#).
- [77] S. Nascimbène, N. Navon, K. J. Jiang, F. Chevy, and C. Salomon, “Exploring the thermodynamics of a universal Fermi gas,” *Nature* **463** (Feb, 2010) 1057–1060, [arXiv:0911.0747](#).
- [78] M. Horikoshi, S. Nakajima, M. Ueda, and T. Mukaiyama, “Measurement of Universal Thermodynamic Functions for a Unitary Fermi Gas,” *Science* **327** no. 5964, (Jan, 2010) 442–445.
- [79] M. J. H. Ku, A. T. Sommer, L. W. Cheuk, and M. W. Zwierlein, “Revealing the Superfluid Lambda Transition in the Universal Thermodynamics of a Unitary Fermi Gas,” (Oct, 2011) , [arXiv:1110.3309](#).
- [80] Y. Shin, C. H. Schunck, A. Schirotzek, and W. Ketterle, “Phase diagram of a two-component Fermi gas with resonant interactions,” *Nature* **451** (Feb, 2008) 689–693.
- [81] N. Navon, S. Nascimbène, F. Chevy, and C. Salomon, “The Equation of State of a Low-Temperature Fermi Gas with Tunable Interactions,” *Science* **328** no. 5979, (Apr, 2010) 729–732, [arXiv:1004.1465](#).
- [82] F. Werner. Private communication.
- [83] X.-J. Liu, H. Hu, and P. D. Drummond, “Virial Expansion for a Strongly Correlated Fermi Gas,” *Phys. Rev. Lett.* **102** no. 16, (Apr, 2009) 160401, [arXiv:0903.5366](#).
- [84] K. Van Houcke, F. Werner, E. Kozik, N. Prokofev, B. Svistunov, M. Ku, A. Sommer, L. W. Cheuk, A. Schirotzek, and M. W. Zwierlein, “Feynman diagrams versus Feynman quantum emulator,” (Oct, 2011) , [arXiv:1110.3747](#).

- [85] T.-L. Ho and E. J. Mueller, “High Temperature Expansion Applied to Fermions near Feshbach Resonance,” *Phys. Rev. Lett.* **92** no. 16, (Apr, 2004) 160404, [cond-mat/0306187](#).
- [86] S. Succi, *The Lattice Boltzmann Equation*. Oxford University Press, 2001.
- [87] T. Lepers, D. Davesne, S. Chiacchiera, and M. Urban, “Numerical solution of the Boltzmann equation for the collective modes of trapped Fermi gases,” *Phys. Rev. A* **82** no. 2, (Aug, 2010) 023609, [arXiv:1004.5241](#).
- [88] B. Jackson and E. Zaremba, “Modeling Bose-Einstein condensed gases at finite temperatures with N -body simulations,” *Phys. Rev. A* **66** no. 3, (Sep, 2002) 033606, [cond-mat/0205421](#).
- [89] A. C. J. Wade, D. Baillie, and P. B. Blakie, “Direct simulation Monte Carlo method for cold-atom dynamics: Classical Boltzmann equation in the quantum collision regime,” *Phys. Rev. A* **84** no. 2, (Aug, 2011) 023612, [arXiv:1105.2340](#).
- [90] E. Taylor, S. Zhang, W. Schneider, and M. Randeria, “Colliding clouds of strongly interacting spin-polarized fermions,” (Jun, 2011) , [arXiv:1106.4245](#).
- [91] S. Chiacchiera, T. Macrì, and A. Trombettoni, “Dipole oscillations in fermionic mixtures,” *Phys. Rev. A* **81** no. 3, (Mar, 2010) 033624, [arXiv:0911.4965](#).
- [92] L. Vichi and S. Stringari, “Collective oscillations of an interacting trapped Fermi gas,” *Phys. Rev. A* **60** no. 6, (Dec, 1999) 4734–4737, [cond-mat/9905154](#).
- [93] D. Guéry-Odelin, F. Zambelli, J. Dalibard, and S. Stringari, “Collective oscillations of a classical gas confined in harmonic traps,” *Phys. Rev. A* **60** no. 6, (Dec, 1999) 4851–4856, [cond-mat/9904409](#).
- [94] M. Amoruso, I. Meccoli, A. Minguzzi, and M. P. Tosi, “Collective excitations of a degenerate Fermi vapour in a magnetic trap,” *Eur. Phys. J. D* **7** no. 3, (Apr, 1999) 441–447, [cond-mat/9907370](#).
- [95] I. D’Amico and G. Vignale, “Theory of spin Coulomb drag in spin-polarized transport,” *Phys. Rev. B* **62** no. 8, (Aug, 2000) 4853–4857.
- [96] A. Trenkwalder, C. Kohstall, M. Zaccanti, D. Naik, A. I. Sidorov, F. Schreck, and R. Grimm, “Hydrodynamic Expansion of a Strongly Interacting Fermi-Fermi Mixture,” *Phys. Rev. Lett.* **106** no. 11, (Mar, 2011) 115304, [arXiv:1011.5192](#).
- [97] W. H. Press, S. A. Teukolsky, W. T. Vetterling, and B. P. Flannery, *Numerical Recipes in C++ : The Art of Scientific Computing*. Cambridge University Press, second ed., 2002.